BRNO UNIVERSITY OF TECHNOLOGY

VYSOKÉ UČENÍ TECHNICKÉ V BRNĚ

CENTRAL EUROPEAN INSTITUTE OF TECHNOLOGY BUT

STŘEDOEVROPSKÝ TECHNOLOGICKÝ INSTITUT VUT

ADVANCED HYDROPHOBIC AND HYDROPHILIC SURFACE TREATMENTS FOR NON-NUCLEAR ENERGETICS

POKROČILÉ HYDROFOBNÍ A HYDROFILNÍ POVRCHOVÉ ÚPRAVY PRO NEJADERNOU ENERGETIKU

DOCTORAL THESIS
DIZERTAČNÍ PRÁCE

AUTHOR
AUTOR PRÁCE

Pavel Komarov

SUPERVISOR
ŠKOLITEL

doc. Ing. Ladislav Čelko, Ph.D.

BRNO 2021

Abstract

Particular interest is given to solid surfaces with specific wetting behavior (hydrophilic/superhydrophilic and hydrophobic/superhydrophobic) due to their wide range of potential applications such as drag-reducing, anti-icing/de-icing, corrosion-resistant, anti-biofouling, self-cleaning, etc. surfaces. However, the production ways of such coatings are sophisticated multi-step procedures, which are expensive and do not provide sufficient robustness of the hydrophilic/hydrophobic wetting behavior.

The doctoral thesis is focused on (i) the development of a technological way to fabricate hydrophilic/hydrophobic coatings from wear-resistant materials utilizing thermal spraying technology; (ii) a detailed investigation of deposited coatings, analysis of their mechanical properties and the robustness of their wetting behavior.

The first part of the thesis represents a theoretical background on the wetting behavior, surface free energy, hydrophilic/superhydrophilic and hydrophobic/superhydrophobic coatings and thermal spraying technology. In the second part, Al_2O_3, Cr_2O_3-SiO_2-TiO_2, YSZ and WC-Co-Cr plasma-sprayed coatings were fabricated, and their wetting behavior was analyzed concerning their surface topography. Furtherly, several YSZ coatings with lamellar and columnar microstructures were studied to investigate the role of the microstructure on their wetting behavior. The effect of RF-plasma jet surface treatment is also presented. Finally, three different powder feedstocks of WC-Co-Cr were utilized to fabricate wear-resistant coatings with the so-called multi-scale surface topography. It was found that the combination of a coarse powder with ultra-fine (~500 nm) WC particles provides an optimal surface topography with a very high hydrophobicity that furtherly can be tuned into the superhydrophobic state after the additional Si-oil treatment. In the last part, the robustness of the wetting behavior of WC-Co-Cr samples was estimated by the slurry abrasion response test and the cavitation erosion resistance test.

Keywords

wetting behavior, surface free energy, hydrophobic coatings, superhydrophobic coatings, thermal spray technology, surface topography, wear-resistance

Abstrakt

V současnosti lze zaznamenat zvýšený zájem o studium pevných povrchů se specifickou smáčivostí (hydrofilní/superhydrofilní a hydrofobní/superhydrofobní) s ohledem na širokou škálu jejich potenciálních aplikací, mezi které patří například snížení aerodynamického odporu, ochrana proti námraze/odmrazování, korozní odolnost, ochrana proti biologickému znečištění, schopnost samočištění povrchů, apod. Způsoby přípravy takových povlaků však zahrnují sofistikované vícestupňové postupy, které jsou nákladné a neposkytují dostatečnou odolnost hydrofilního/hydrofobního chování takto modifikovaného povrchu.

Předkládaná disertační práce je zaměřena na (i) vývoj technologického způsobu výroby hydrofilních/hydrofobních povlaků z materiálů odolných proti opotřebení s využitím technologie žárového nástřiku; a (ii) studium připravených povlaků, analýza jejich mechanických vlastností a kvality smáčivosti jejich povrchu.

První část práce obsahuje úvod do teorie smáčivosti, volné povrchové energie, hydrofilních/superhydrofilních a hydrofobních/superhydrofobních povrchových úprav a přehled technologií žárových nástřiků.

V rámci druhé, experimentální, části byly připraveny povlaky na bázi Al_2O_3, Cr_2O_3-SiO_2-TiO_2, YSZ a WC-Co-Cr a analyzováno jejich smáčivé chování s ohledem na topografii jejich povrchu. Dále byly studovány povlaky YSZ s lamelární a kolumnární mikrostrukturou, s ohledem na posouzení vlivu struktury povlaku na smáčivé chování. Prezentován je zde rovněž modifikovaný povlak s využitím vysokofrekvenčního plasmatu. V závěrečné fázi experimentů byly použity tři rozdílné prášky na bázi WC-Co-Cr pro výrobu povlaků odolných proti opotřebení s tzv. více stupňovou povrchovou topografií povrchu této aktivity. V rámci bylo zjištěno, že kombinace hrubého prášku s ultra jemnými (~500 nm) WC částicemi umožňuje vznik optimální povrchové topografie s velmi vysokou hydrofobností, kterou lze dále optimalizovat do superhydrofobního stavu pomocí dodatečné modifikace olejem na bázi Si. V poslední části práce byla u tohoto typu povlaku stanovena odolnost smáčivosti vzorků WC-Co-Cr pomocí testu odezvy na otěr v abrazivní suspenzi a testu odolnosti vůči kavitační erozi.

Klíčová slova

smáčivost, povrchová volná energie, hydrofobní povlaky, superhydrofobní povlaky, technologie žárového nástřiku, povrchová topografie, odolnost proti opotřebení

Bibliographic citation:

KOMAROV, Pavel. *Advanced hydrophobic and hydrophilic surface treatments for non-nuclear energetics*. Brno, 2022. Available also at: https://www.vutbr.cz/studenti/zav-prace/detail/140823. Doctoral Thesis. Vysoké učení technické v Brně, Středoevropský technologický institut VUT, Central European Institute of Technology BUT. Supervisor Ladislav Čelko.

Sworn statement

I hereby declare that I have written the PhD thesis on my own following to recommendations of my supervisor Assoc. Prof. Ladislav Čelko, and it is an original work with cited literature and other professional sources listed in the text and reference list.

Pavel Komarov

Acknowledgments

First of all, I would like to thank my supervisor, Assoc. Prof. Ladislav Čelko, for this opportunity, guidance, encouragement and advice on my journey to the PhD title.

Special thanks go to my colleagues from the Advanced Coatings research group, who shared their experience, knowledge and time with me. Their contribution is highly appreciated.

Also, I would like to sincerely acknowledge the CEITEC BUT for PhD scholarship and the CEITEC Nano (CzechNanoLab Research Infrastructure supported by MEYS CR (LM2018110)), who provided access to their facilities.

Last but not least, my lovely family and my lovely partner, thank them very much for their enormous patience and support. I love them.

Table of contents

1 Introduction

Wetting behavior, or wettability, is an essential property of the surface of solid materials. Based on the wetting behavior of water, all the surfaces can be divided into (i) superhydrophobic/hydrophobic (when water is repelled from the solid surface) and (ii) superhydrophilic/hydrophilic (when water droplets spread on the solid surface) [1]. Superhydrophobic/hydrophobic and superhydrophilic/hydrophilic surfaces are of high interest in the research field of fundamental and applied science due to their wide range of potential applications in almost every field of industry where interaction with water or other liquid exists (chemical industry, machine building, machine engineering, medicine, etc.). Particular attention is focused on surfaces with robust hydrophobic and superhydrophobic behavior. Such surfaces are highly attractive due to the possibility to provide (i) water-oil separation (as a mesh or filters where a superhydrophobic-oleophilic surface interacts with oil, but repels water); (ii) self-cleaning (dust and ultra-fine particles are collected during the sliding of water droplets giving higher performance of solar cells); (iii) anti-icing/de-icing (to prevent ice accumulation or decrease ice adhesion in off-shore components, parts of an aircraft, and wind mills where ice affects their productivity and/or might be a cause of a crash of an aircraft); (iv) self-condensed microdroplets (hydrophobic surfaces are intended to provide drop-wise condensation mechanism of heat transfer that is almost 10 times more effective than film-wise mechanism that typically occurs on currently used hydrophilic metallic surfaces); (v) anti-biofouling (hydrophobic/superhydrophobic surfaces have a smaller contact area with water in comparison to hydrophilic surfaces, giving less space for micro-organisms to attach and grow on the surfaces of the parts of the ships that are in long-term contact with water); (vi) increased corrosion resistance (as superhydrophobic/hydrophobic surfaces have a smaller contact area with liquid); (vii) drag-reduction (low adhesion of water to the hydrophobic/superhydrophobic surfaces decrease an energy loss during movement of the ships and submarines in water), etc. [2, 3].

Nevertheless, the industrial application of superhydrophobic/hydrophobic coatings is limited due to several factors: (i) such surfaces require a combination of the so-called multi-scale surface topography (namely co-existence of nano- and micron-sized topographical features) with low-surface energy materials; (ii) most of the superhydrophobic/hydrophobic surfaces show a lack of mechanical robustness, especially low wear-resistance, that leads to the loss of the hydrophobicity during the lifetime; (iii) the majority of currently used technologies are sophisticated, expensive, time-consuming and require the use of a vacuum/inert gas chamber that constrains the treated surface in size and shape (e.g. electron beam, plasma

treatment, physical vapor deposition, plasma-enhanced vapor deposition, etc.). Thus, it is important to produce wear-resistant coatings with superhydrophobic/hydrophobic behavior utilizing cost-effective and industrially scalable technology [4].

For these reasons, thermal spraying is of great potential for the fabrication of surfaces with specific wetting behavior as a relatively less sophisticated technology. Thermal spraying is already widely used in the production of wear-resistant, thermal barrier, corrosion-resistant and other types of coatings for direct application in many industrial fields. By means of this technology, it is possible to obtain coatings from ceramic, metallic, cermet, polymer powders and their combinations. The group of thermal spraying includes several technologies: flame spraying, wire arc spraying, high-velocity oxy-fuel technology, plasma spraying and others.

The present work is divided into three main parts. The first part of the thesis describes the theoretical background of the wetting behavior, surface free energy and thermal spray technology. The current state of the art on the superhydrophobic/hydrophobic and superhydrophilic/hydrophilic surface treatments is also presented. In the second part, the experimental design and methods are described. The last part, Results and Discussion, starts with researching the wetting behavior of Al_2O_3, Cr_2O_3-SiO_2-TiO_2, ZrO_2-Y_2O_3 (YSZ) and WC-Co-Cr wear-resistant coatings fabricated by the atmospheric plasma spray technique. The wettability of the produced coatings was studied concerning their surface topography in the as-sprayed, ground and polished states. Based on the results, YSZ and WC-Co-Cr materials were chosen for further research. In the next stage, YSZ coatings with a columnar microstructure were fabricated through the suspension plasma spray route using nano- and submicron-sized powders, and these were compared with conventional YSZ coatings possessing lamellar microstructure obtained by atmospheric plasma spraying. Furthermore, the effect of the microstructure, surface topography and radio-frequency plasma jet surface treatment on the wetting behavior of YSZ coatings was investigated. Finally, the wear-resistant WC-Co-Cr coatings were fabricated utilizing high-velocity oxy-fuel spraying, using three different powder feedstocks: coarse powder, coarse powder with ultra-fine WC particles and fine powder with ultra-fine WC particles. The role of the surface chemical composition and surface topography on the wetting behavior of WC-Co-Cr coatings was analyzed and discussed. The technologically simple way to improve the hydrophobicity using Si-oil treatment of the solid surface is also presented. The robustness of the superhydrophobic/hydrophobic behavior of the most hydrophobic WC-Co-Cr coatings was studied using the slurry abrasion response test and the cavitation erosion resistance test. Additionally, several preliminary tests of superhydrophobic coatings for further potential applications were conducted and presented.

2 Review

2.1 Wetting behavior of solid surfaces

The wettability or wetting behavior of solid surfaces is commonly determined by the value of the water contact angle (WCA). Based on the WCA, all materials can be divided into four main groups: (i) superhydrophilic (WCA ≤ 10°), (ii) hydrophilic (10° < WCA < 90°), (iii) hydrophobic (90° ≤ WCA < 150°) and (iv) superhydrophobic (150° ≤ WCA) [1-3]. The most important factors that have an impact on wetting behavior are surface chemistry and surface topography.

Wetting behavior of ideally smooth surfaces

The intersection of the liquid-vapor and solid-liquid interfaces forms the angle also known as "contact angle", i.e., the angle between the tangent to the curved surface of a liquid droplet and a wetted solid surface as illustrated in Figure 1. The interface where the existence of three phases (liquid, solid and gas) appears is called the "three-phase contact line", this line is marked by the color red in Figure 1.

Assessment of the wetting behavior of an ideally smooth solid surface is described by Young's equation (1), where γ_{lv} is the liquid surface tension, γ_{sv} is the solid surface free energy (SFE), γ_{sl} is the solid/liquid interfacial free energy and θ_Y is the contact angle. A graphical illustration of Eq. 1 is presented in Figure 1.

$$\gamma_{sv} - \gamma_{sl} = \gamma_{lv} * cos\theta_Y \quad (1)$$

Thomas Young [5] was the first who proposed the capillary theory. According to Young's theory, the hydrophobic surfaces possess high WCA and low γ_{sv} surface free energy in comparison to the hydrophilic materials.

The surface free energy is a thermodynamic function that characterizes the energy of intermolecular force of particles at the interface with particles of each of the contacting phases. Another definition of the surface free energy is the potential energy that is concentrated at the interface required to form a unit of surface area. The surface free energy is excessive (SFE > 0), and the unit of SFE is J/m^2 [6, 7]. SFE depends on chemistry (e.g., SFE of polytetrafluoroethylene is 21.0 mJ/m^2 and SFE of Cu is 1650 mJ/m^2) and the aggregate state of the material. As follows from the Eq. 1, the ideally smooth solid surfaces with a low value of SFE are hydrophobic. Several examples of materials with low surface free energy and their wetting behavior are summarized in Table 1.

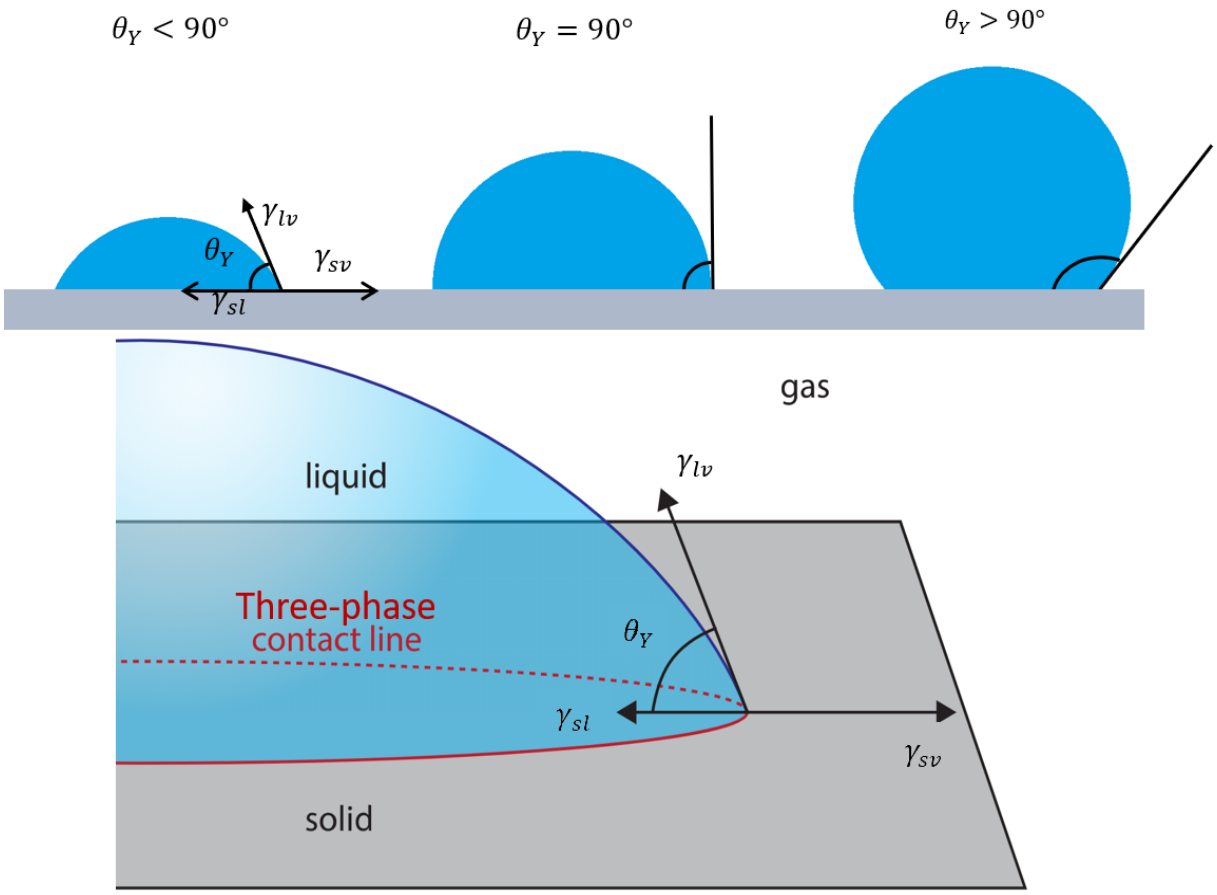

Figure 1 Wetting behavior of ideally smooth solid surface

Table 1 Values of several solid materials' surface energy and their water contact angles

Material		Surface energy [mJ/m^2]	Water contact angle [°]	Ref.
Poly (methylpropenoxy-fluoroalkylsiloxane) with number of CF_2-group (n)	n = 3	14.2	105.0	[8]
	n = 5	16.0	102.4	[8]
	n = 7	12.6	106.7	[8]
	n = 9	12.2	109.3	[8]
Polytetrafluorethylen		21.0	110.0	[8], [9]
Octadecanol		20.0	117.0	[10]
Perfluoroeicosane		6.7	122.0	[11]

It was experimentally observed that the material with the almost ideally smooth surface and the lowest surface energy (regular aligned closest hexagonal packed $–CF_3$ groups of n-Perfluoroeicosane) [11] had a water contact angle value of 119˚. The SFE value of n-perfluoroeicosane was measured as 6.7 mJ/m^2. The work of Nishino et al. [11] pointed out that it is not possible to obtain the superhydrophobic state only by lowering the surface energy of the solid surface.

As the SFE value depends on the material's chemistry, the wetting behavior is also affected by the surface chemistry heterogeneity, crystalline structure and grain boundaries in polycrystalline and composite materials (e.g., cermet materials). On the smooth surface of polycrystalline materials, there are plenty of arbitrarily oriented grains with different crystallographic facets, and each of them might have different "solid-liquid" free surface energy. In composite materials, grains with different chemical compositions (e.g., WC and Co) also have different SFE values. Based on that, it can be concluded that the boundary between two different phases or crystals might act as an energy barrier for the three-phase contact line to move, i.e., liquid droplet to be spread and increase solid surface hydrophobicity [4].

According to the Owens-Wendt method (also known as the "harmonic mean" method), the surface energy of a solid consists of a sum of two components: a polar component (γ^p) and a dispersive (γ^d) component, Eq. 2-5 [7, 12-14].

$$\gamma_{SL} = \gamma_L + \gamma_S - 2\sqrt{\gamma_S^d * \gamma_L^d} - 2\sqrt{\gamma_S^p * \gamma_L^p} \tag{2}$$

$$\gamma_S = \gamma_{SL} + \gamma_L * cos\theta \tag{3}$$

$$\gamma_L(1 + cos\theta) = 2\sqrt{\gamma_S^d * \gamma_L^d} - 2\sqrt{\gamma_S^p * \gamma_L^p} \tag{4}$$

$$\gamma_S = \gamma_S^d + \gamma_S^p \tag{5}$$

where θ is the contact angle of the liquid on the solid surface; γ_{SL} is the interfacial energy of solid-liquid interface; γ_S is the surface free energy of solid; γ_S^d is the dispersive component of solid surface SFE; γ_S^p is the polar component of solid surface SFE; γ_L is the surface energy of liquid (surface tension); γ_L^d is the dispersive component of liquid surface energy; and γ_L^p is the polar component of the liquid's surface energy.

Theoretically, the polar component refers to the dipole-dipole, dipole-induced dipole, hydrogen bonding and acid-base interactions. The dispersive component theoretically refers to the van der Waals interactions. As van der Waals interactions appear between all atoms and molecules, no solid or liquid material's SFE entirely consists of the polar component. However, some substances' SFE consists only of a dispersive component (e.g. alkanes). The Owens-Wendt theory supposes that the polar part of the solid surface will interact with the polar part of the liquid, as well as the dispersive part of the solid will interact with the dispersive part of the liquid, see Figure 2 [14, 15]. In other words, the polar liquid (e.g., water) should spread on the polar surface (e.g., Al_2O_3), giving a low water contact angle with hydrophilic behavior.

The most common way to measure the surface free energy of solid materials is the sessile droplet method with measurement of the contact angles of several liquids, and further calculations according to Young's Eq. (1) and the Owens-Wendt method (Eq. 2-5). In the case of the Owens-Wendt method, two known liquids are used, usually water (as a liquid with a predominant polar component) and diiodomethane (as a liquid with $\gamma^P \sim 0$ polar component). However, other known liquids can also be used, and the rule is to use liquids with a significant difference in the distribution of the polar and the dispersive components. Several examples of such liquids are presented in Table 2 (data is taken from the See System software).

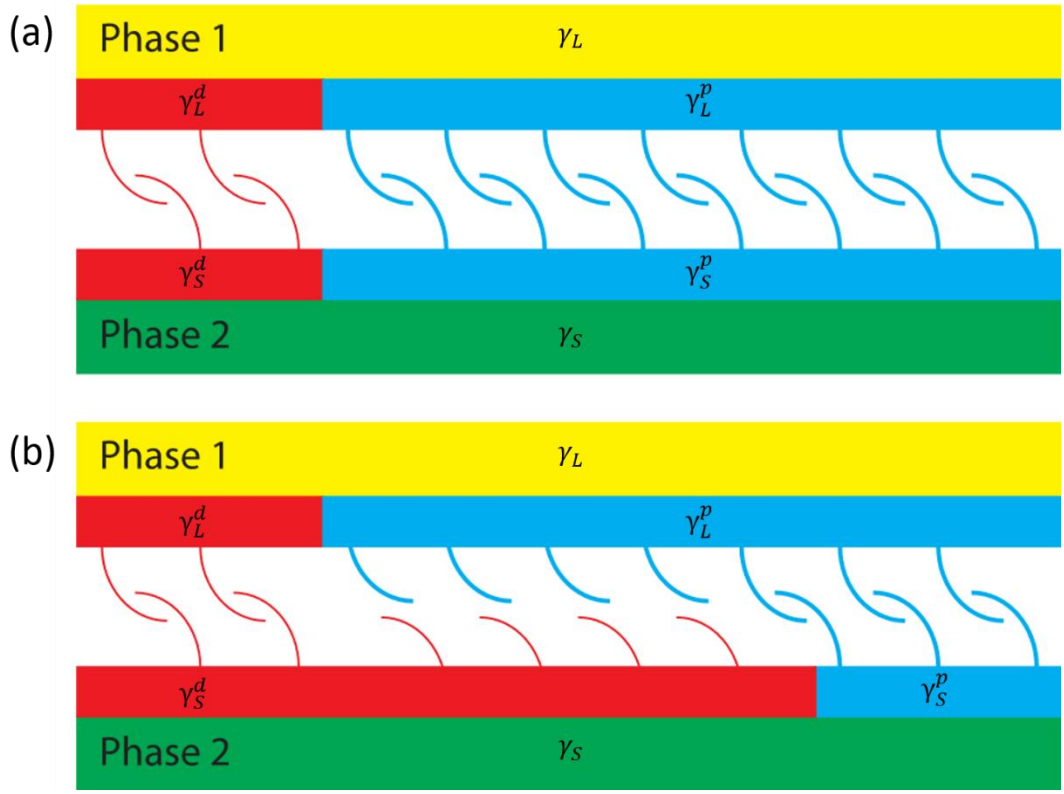

Figure 2 Illustration of the interactions of a liquid with solid surfaces with (a) similar and (b) different distribution of dispersive and polar components, adapted from [14]

Table 2 Surface tension values for different liquids from See System software

Liquid	Surface tension [mJ/m^2]	γ^d [mJ/m^2]	γ^p [mJ/m^2]
Water	72.80	21.80	51.00
Glycerol	64.00	34.00	30.00
Ethylene glycol	48.00	29.00	19.00
Diiodomethane	50.80	50.80	0.00
Formamide	58.00	39.00	19.00
α-bromonaphthalene	44.40	43.50	0.00

Wetting behavior of rough surfaces

Young's equation only describes the water wetting behavior of the ideally smooth surface, which is impossible to find in real objects. Real objects consist of complicated micro-relief with peaks and valleys with different shapes and dimensions. Therefore, in the first half of the 20th century, Wenzel [16, 17] and Cassie-Baxter [18] proposed the equations trying to incorporate solid material rough surface in two different ways of wetting, see Figure 3. According to them, wetting can be homogeneous (Wenzel state of wetting) without entrapped air pockets; and/or heterogeneous (Cassie-Baxter state of wetting) with entrapped air pockets between solid and liquid phases. The wetting mechanism depends on substrate material surface energy, temperature, mass and speed of droplet when it impacts the surface, time of wetting, etc. [4].

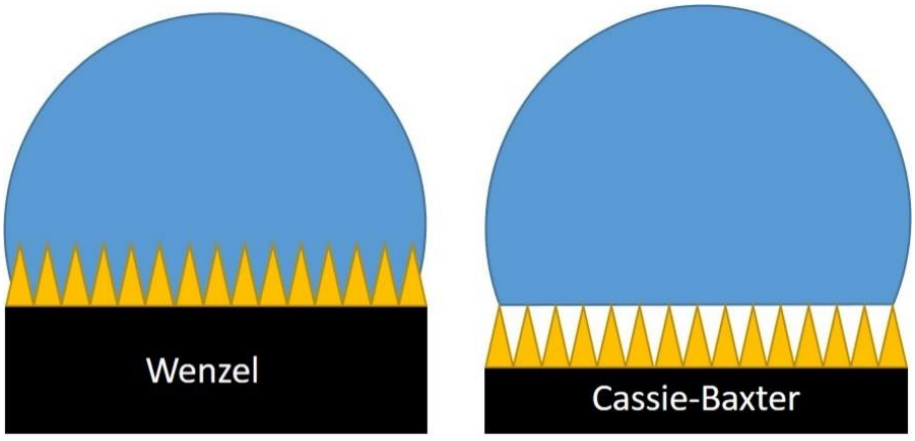

Figure 3 Schematic representation of Wenzel and Cassie-Baxter wetting models

According to Wenzel (Eq. 6), surface roughness amplifies the hydrophilicity of the intrinsically hydrophilic solid surface (when the solid surface is hydrophilic in the ideally smooth state); and amplifies hydrophobicity for intrinsically hydrophobic solid surface:

$$cos\theta_W = Rs * cos\theta_Y \quad (6)$$

where θ_W is the contact angle of a liquid droplet on the rough surface; $cos\theta_Y$ is the contact angle on the similar ideally smooth surface; and Rs is the surface roughness factor that shows the complexity of the surface and is expressed as the ratio "real surface area/projected surface area".

On the other hand, the Cassie-Baxter model (Eq. 7) describes the wetting behavior of the rough surface with entrapped air pockets existing in between the liquid and solid phase, where the liquid contact with a solid surface exists only at a small surface area and can be represented by the equation (7):

$$cos\theta_{CB} = f_s * cos\theta_Y + f_s - 1 \quad (7)$$

where θ_{CB} is the contact angle between a liquid droplet and a rough surface; and f_s is the part of the surface area that is in contact with a liquid droplet.

Besides the general division based on the WCA value, the wetting behavior of the superhydrophobic surfaces can also differ based on their water mobility and the value of the sliding angle (SA). The sliding angle is defined as the minimum tilt angle of the solid surface when the liquid droplet starts to move. If the sliding angle is low (SA < 10°), pointing to a high water mobility with low adhesion to the surface, then the superhydrophobic surface possesses the so-called *Lotus effect*; and if the sliding angle is high (water droplet does not repel from the surface even in upside-down position), then the superhydrophobic surface possesses the so-called *Rose petal effect* [19].

Nowadays, research shows that regardless of the material, to obtain superhydrophobic behavior of the solid surface with the *Lotus effect* [19], the formation of the multi-scale surface roughness is required [20]. The multi-scale rough surface consists of micro-peaks that are covered by nano-sized peaks, see Figure 4. The presence of entrapped air pockets is most likely in between the nano-sized peaks. Entrapped air pockets prevent the contact of the water droplet with the solid surface, thus improve water repellency (enhance hydrophobicity) and water mobility (lower SA) [20].

The combination of Wenzel and Cassie-Baxter models (Eq. 8) was found to be helpful in the description of the wetting behavior of solid surfaces with the multi-scale roughness [21], where the surface roughness factor *Rs* and the surface area of "solid-liquid" contact f_s are considered:

$$cos\theta_{CBW} = Rs * f_s * cos\theta_Y + f_s - 1 \quad (8)$$

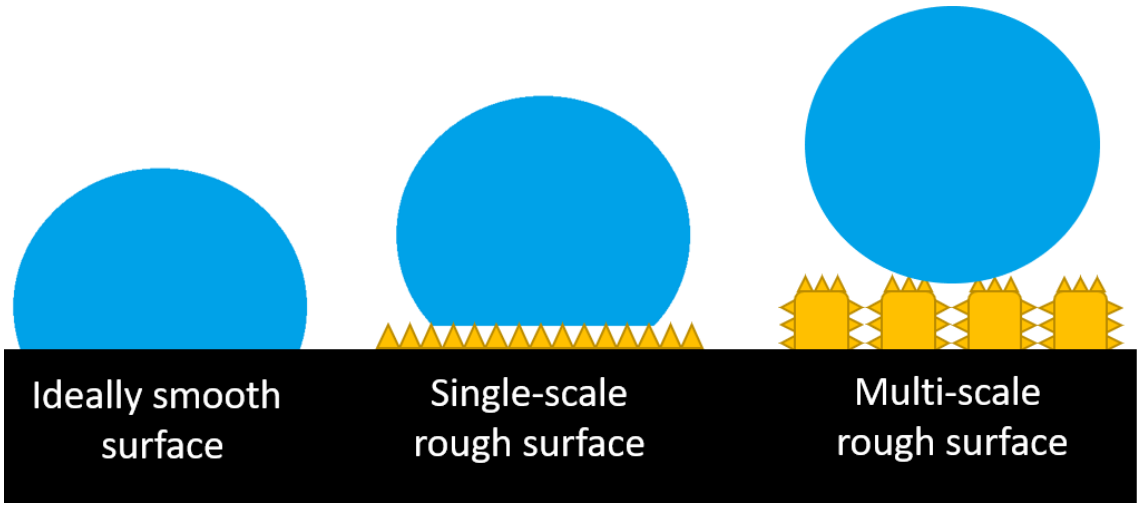

Figure 4 Schematic illustration of the wetting behavior of solid material surface with a different type of surface roughness

2.2 Development of surfaces with specific wetting behavior

Hydrophilic/Superhydrophilic surfaces

Most well-known and widely used construction materials, such as metals and ceramics, are hydrophilic due to their high surface free energy (metals) and polar components (ceramics). In the review [22], it is reported that only several solid material surfaces possess almost superhydrophilic behavior (WCA ~ 10° or below): gold, copper, chromium, TiO_2, quartz, amorphous silica and glass. Such superhydrophilicity appears only if these surfaces are properly cleaned or freshly prepared. For other less hydrophilic or even hydrophobic materials, two common approaches of hydrophilization are used: (i) deposition of more hydrophilic molecular structures than the base material (in the case of inorganic base materials); or (ii) modification of the surface chemistry i.e., increasing of SFE (in the case of polymers with low SFE) [22].

In the first approach, the most studied organic molecular structures are alkanethiols on silver, platinum and palladium; chlorosilanes on aluminum, silicon dioxide, titanium; phosphonic acids on titanium, aluminum [22, 23]. The hydrophilic behavior of these deposited organic mono- and multi-layers appears only when hydrophilic polar groups are at the top of the layer. If there are hydrocarbon- or fluorine-containing groups at the top, then the layer will show more hydrophobic behavior. Even though the water contact angle of a zero degree was not achieved in all the aforementioned hydrophilic layers [22, 23].

The studies focused on surface chemistry modification by plasma, corona discharge, flame, protons, electrons, ions, X-rays, γ-rays and ozone treatments to tune the hydrophobic surface of polymers into hydrophilic without an impact on the bulk properties of the materials were

reported [22, 23]. The most studied are the plasma and corona treatments. These techniques use accelerated electrons, which bombard the polymer structures in order to break the molecular bonds further. After that, produced free radicals generate cross-linking, react with the oxygen from the surrounding air and create oxygen-based groups (e.g., hydrophilic polar hydroxyl, peroxy, carbonyl, carbonate, ether and ester groups). However, modified surface layers were of low robustness and destroyed in the air after a short time [22, 23].

Hydrophobic/Superhydrophobic surfaces

In general, the manufacture of the hydrophobic/superhydrophobic surfaces is inspired by various natural surfaces, and based mainly on the surface treatment to deposit low surface energy materials and/or to form multi-scale topography [23, 24]. Plenty of methods were applied to develop superhydrophobic surfaces including lithography, solution immersion, plasma etching, templating, electrodeposition, sol-gel, etc. [24, 25]. As an example of such work, the authors [26] investigated artificial Lotus multi-scale structured leaves fabricated by replicating natural Lotus leaves (*Nelumbo nucifera*) microstructure using a two-step molding process and by self-assembled tubule formed waxes isolated from Lotus leave. This study shows that multi-scale topography amplified the water repellency of the replicate from hydrophobic behavior with WCA of 119° (in the polished state) up to superhydrophobic behavior with WCA of 171°.

Significant attention was recently focused on the rare-earth elements' oxides (REO's) due to the work reported by Azimi et al. [27], where REO's were presented as ceramics with intrinsically hydrophobic behavior in the polished state. The authors observed such unusual water repellency for ceramic surfaces and suggested its connection with REO's electronic structure on the *4f* orbitals compared to other common ceramics such as alumina, see Figure 5. However, it should be noted that the sintered pellets of REO's were stored in a vacuum prior to water contact angle measurements. Thus, the surface of pellets could also be affected by vacuum preprocessing.

Further research on this topic shows varying results which keep the hydrophobicity of REOs under debate: (i) authors suggest an explanation of hydrophobicity of Yb_2O_3 as an effect of hydrocarbon adsorption from the atmosphere or after vacuum treatment [28, 29]; (ii) oxide-to-metal ratio was suggested to be responsible for low-WCA of ~15° in the case of freshly prepared CeO_2 with O/Ce (at. %) ratio of ~3.0 and after ultra-high vacuum treatment the O/Ce ratio decreased to ~2.2, and the WCA increased up to 104° [30]; (iii) the low value of electronegativity was shown as a predominant factor in the hydrophobicity of Nd-O compound

rather than electronic structure [31]; and (iv) other work shows even complete wetting (superhydrophilicity) with WCA of 0° of Ho_2O_3 and CeO_2 [32].

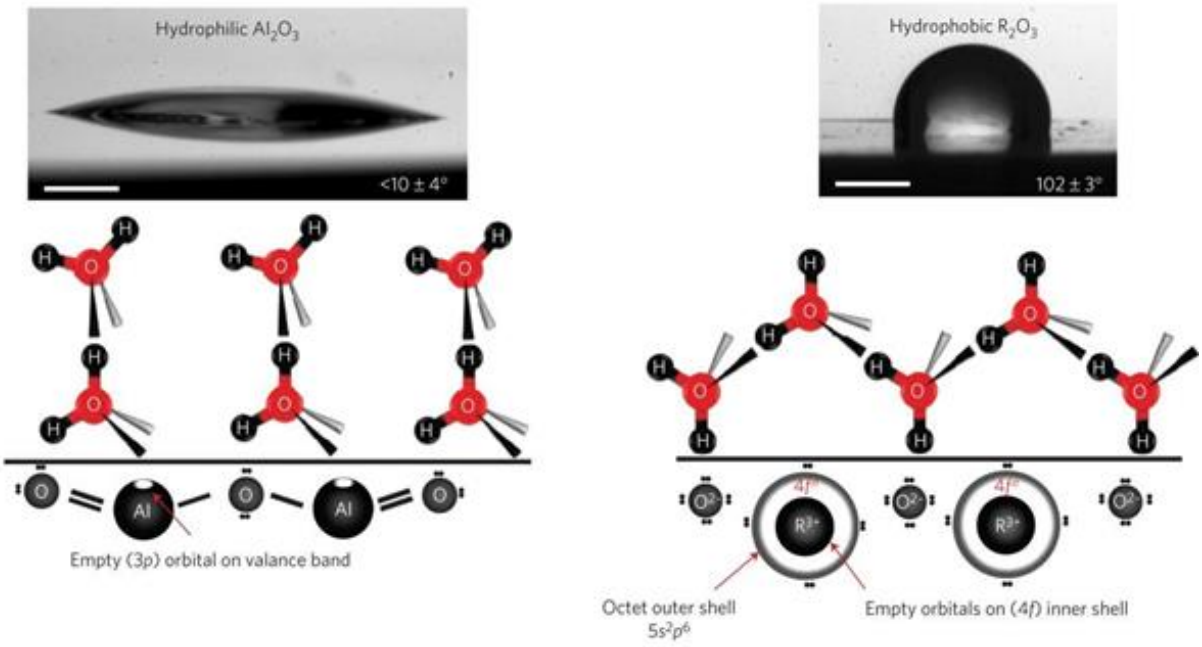

Figure 5 Schematic illustration of the difference in the electronic structure of hydrophilic alumina and hydrophobic rare-earth element oxides [27]

2.3 Application of surfaces with specific wetting behavior

Depending on the wetting behavior, chemical, physical and mechanical properties, the surfaces with specific wetting behavior can be used in various applications:

- *water-oil separation*: meshes or filters where the oleophilic-superhydrophobic surface will attract oil from emulsion but repel the water providing separation [4, 33];
- *anti-biofouling*: for ships or parts of the ships where hydrophobic-superhydrophobic surfaces will repel water and give fewer opportunities for micro-organisms to grow; and the opposite with hydrophilic surfaces that are covered by water in off-shore what creates conditions for different micro-organisms to grow, Figure 6 [10];
- *self-condensed microdroplets*: heat-transfer systems where hydrophobic surfaces are supposed to ensure drop-wise condensation (DWC) mechanism results in ~10 times higher heat transfer performance in comparison to film-wise condensation (FWC). Nowadays, the steel or copper tubes covered by a thin film of oil to promote DWC heat transfer, but after several cycles, these films are simply washed away, and metallic tubes remain uncovered and hydrophilic with FWC heat transfer mechanism, Figure 7 [34, 35];

- *self-cleaning*: for solar cells, where dust or other ultra-fine particles decrease the effectivity of the device, the usage of transparent superhydrophobic layer with superior water mobility enables the water droplet to slide off the surface and to collect the dust and/or ultra-fine particles [4, 36, 37];
- *Anti-icing, de-icing, anti-frosting*: for off-shore components, platforms, outer parts of airplanes, windmills, etc. where a high value of water contact angle and low sliding angle (SA < 10°) could minimize ice adhesion and ice accumulation. In real applications, the surfaces are rarely in 0° horizontal position; thus, water droplets are expected to slide off from the surface, Figure 8 [38-40];
- *Corrosion resistance*: as with the increase of WCA, the area of contact of a solid surface with a corrosive liquid (water) environment is decreasing, and a chance of electrochemical reaction is reduced [40];
- *Drag-reduction*: of submarines, ships, pipes (as muddy-water transportation) where low adhesion of liquid at solid surfaces will reduce an energy loss promoted by friction during the movement of the liquid in pipes or resulting in more effortless movement of the ships or submarines [41];
- *Increased cavitation erosion (CE) resistance*: since the erosion mechanism of cavitation is amplified by corrosion, and the superhydrophobic surface is expected to be more corrosion resistant than hydrophilic; also, CE resistance of a coating is dependent on its density and hardness [42]. Thus, hard and dense hydrophobic/superhydrophobic coatings are of great interest for hydro-turbine applications, ship propellers, hydraulic systems, etc. [40].

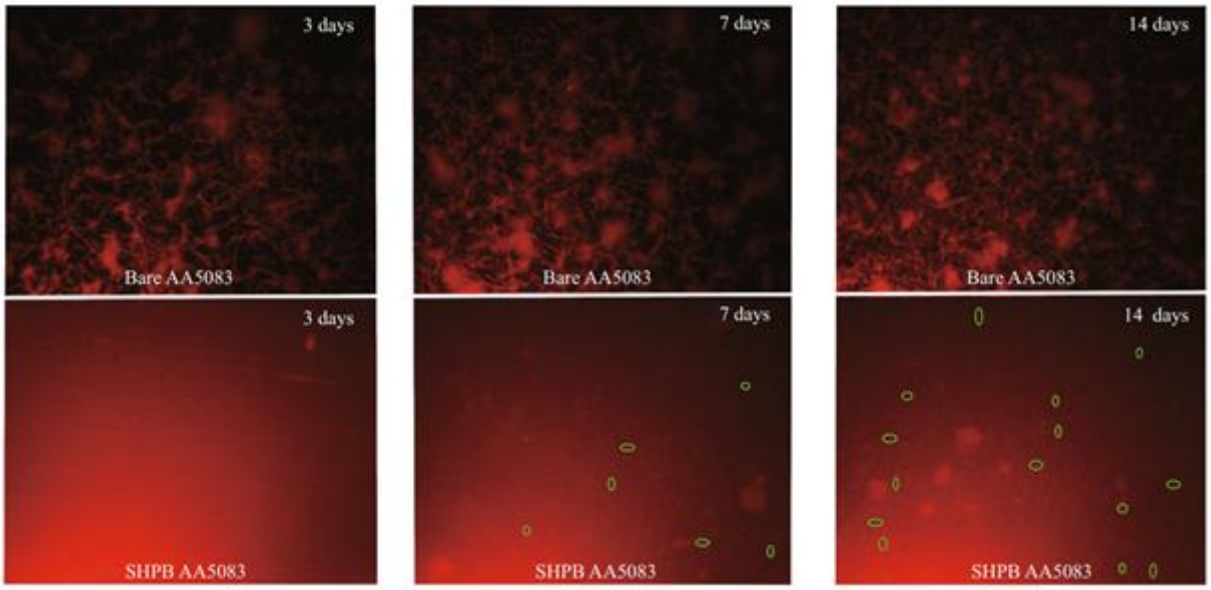

Figure 6 Fluorescent micrographs showing different adhesion of seaweed (*Navicula algae*) onto hydrophilic (top) and superhydrophobic (bottom) surfaces of AA5083 Al alloy [43]

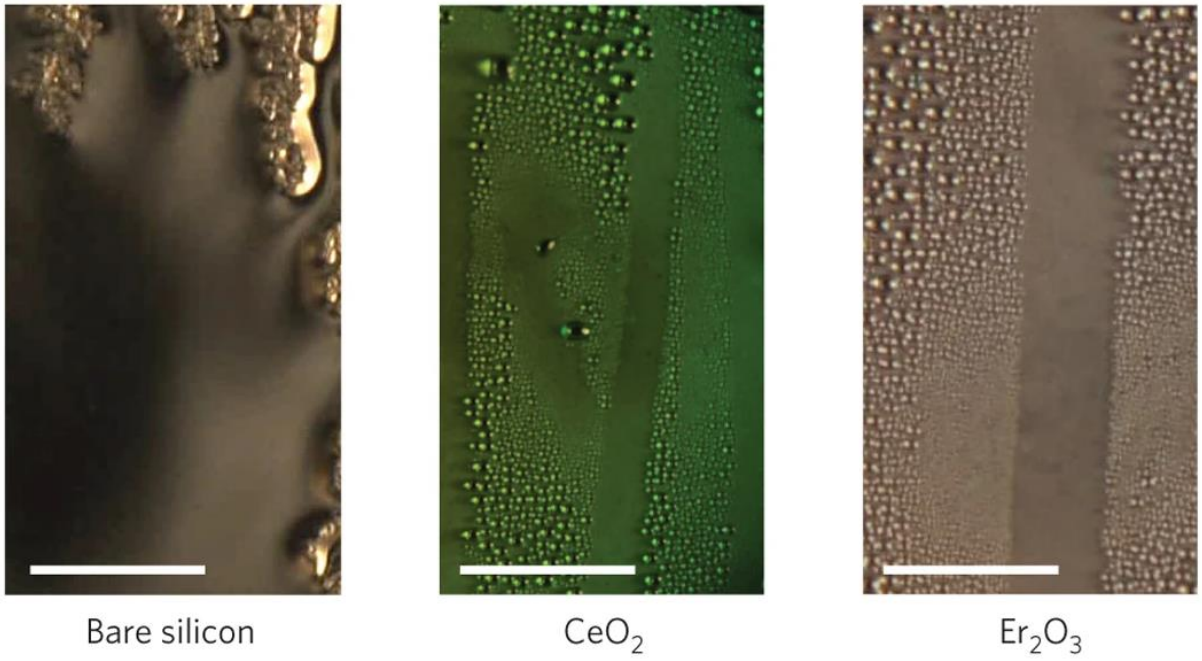

Figure 7 Film-wise condensation (bare silicon) and drop-wise condensation (CeO_2 and Er_2O_3); scale bars are of 5 mm [27]

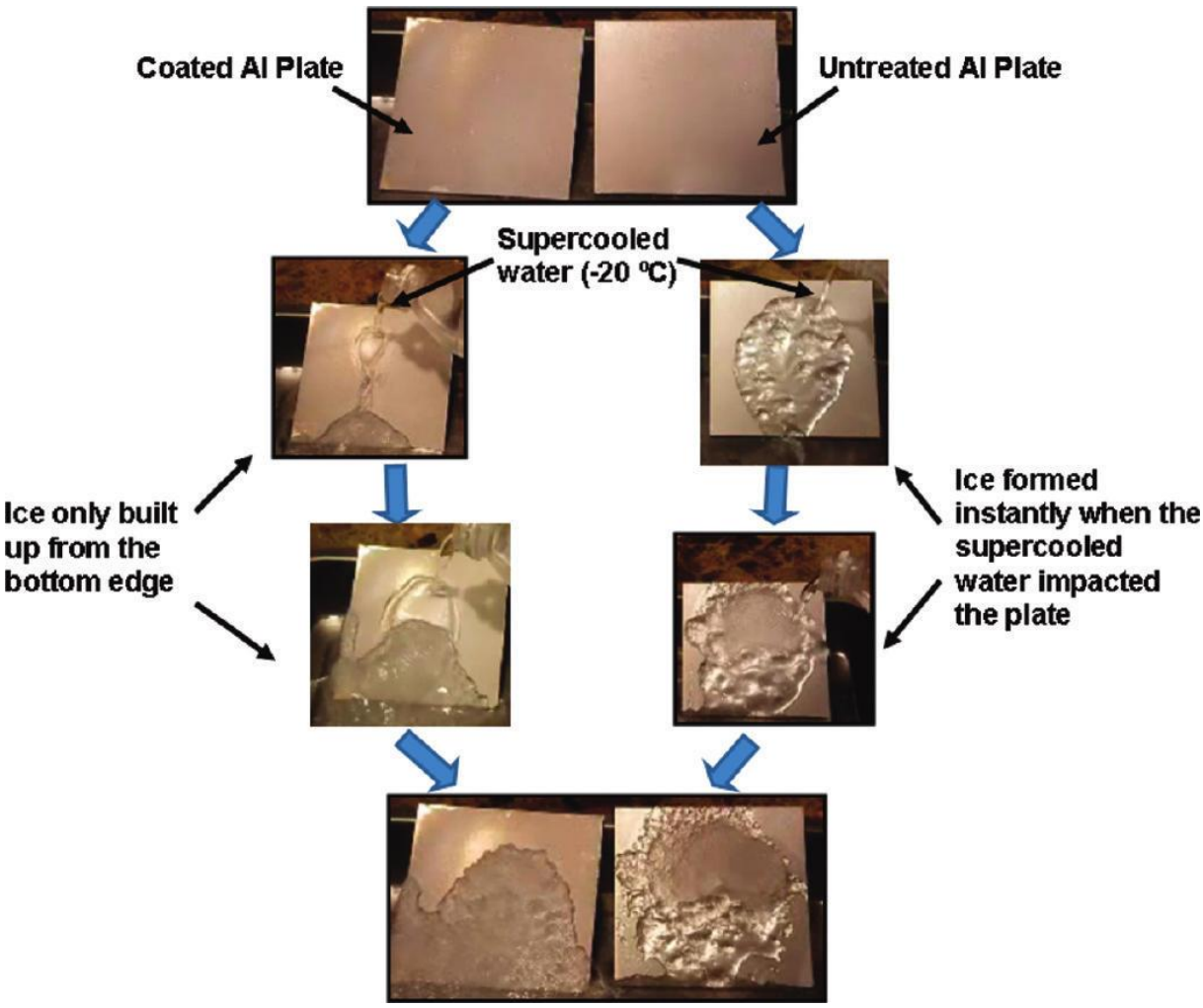

Figure 8 Anti-icing performance of coated superhydrophobic Al plate in comparison to untreated hydrophilic Al plate [44]

However, most of the methods used to manufacture the coatings with specific wetting behavior (superhydrophilic, hydrophilic, hydrophobic, superhydrophobic) have several major disadvantages that limit their industrial-scale application, such as the time-consuming nature of the process or constraints on the size and shape of treated components, due to the required vacuum or inert atmosphere chamber, the insufficient mechanical stability (e.g., low wear resistance of fluoropolymers) [45], degradation in the harsh atmosphere, or even in the sunlight, and high technology costs associated with the purchasing cost of rare-earth element oxides and their precursors [24, 46, 47].

Therefore, developing cost-effective and industrially scalable technology for the fabrication of mechanically durable surfaces with a robust specific wetting behavior remains challenging.

2.4 Thermal spray technology

Thermal spraying is a potential candidate for the manufacturing of coatings with specific wetting behavior. It is a highly industrialized, relatively fast and cost-effective way to deposit coatings on a large scale. This technology is widely used in the fabrication of porous/dense, wear-resistant/abradable, corrosion-resistant, thermal/environmental barrier, and other types of coatings from metallic, ceramic, cermet, and polymer materials. During thermal spraying, a feedstock material (wire, powder or suspension) is fed to a plasma or a flame jet followed by heating and acceleration of particles towards the substrate. Thus, the formation of the coating is a result of the plastic deformation of accelerated melted, partially melted, or un-melted particles that impacted the substrate surface, as illustrated in Figure 9. Using thermal spraying enables the deposition of coatings with a thickness ranging from several micrometers up to a few millimeters.

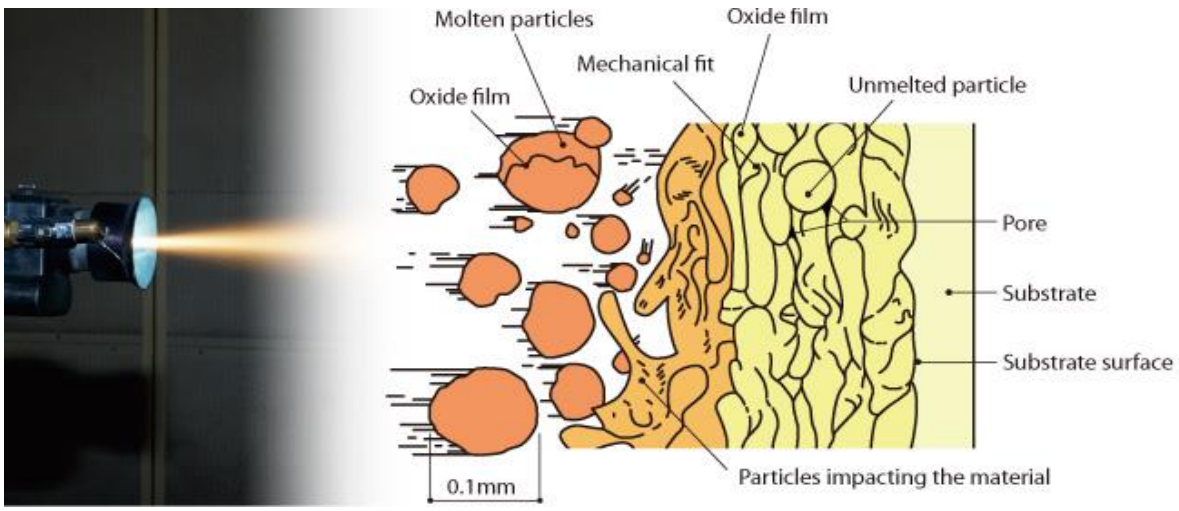

Figure 9 Principle of coating formation during thermal spray [48]

The group of thermal spraying methods consists of several technologies the most important ones are atmospheric plasma spraying (APS), water-stabilized plasma spraying (WSP-H), high-velocity oxy-fuel spraying (HVOF), high-velocity air-fuel spraying (HVAF), flame spraying (FS), twin wire arc spraying (TW), detonation-gun spraying (D-Gun) and cold-gas dynamic spraying (CG or CGS). There also exist certain modifications of these technologies based on the type of the feedstock (e.g., powders suspension and/or precursors solution) and the surrounding atmosphere (vacuum/low pressure): suspension plasma spraying (SPS), solution precursor plasma spraying (SPPS), vacuum plasma spraying (VPS), low-pressure plasma spraying (LPPS), suspension high-velocity oxy-fuel spraying (S-HVOF), etc. Figure 10 shows the main difference among representative technologies based on the in-flight particle velocity and the temperature of the flame [49].

Later on, HVOF, APS, SPS and WSP-H technologies will be introduced in more detail as the technologies used in the present work.

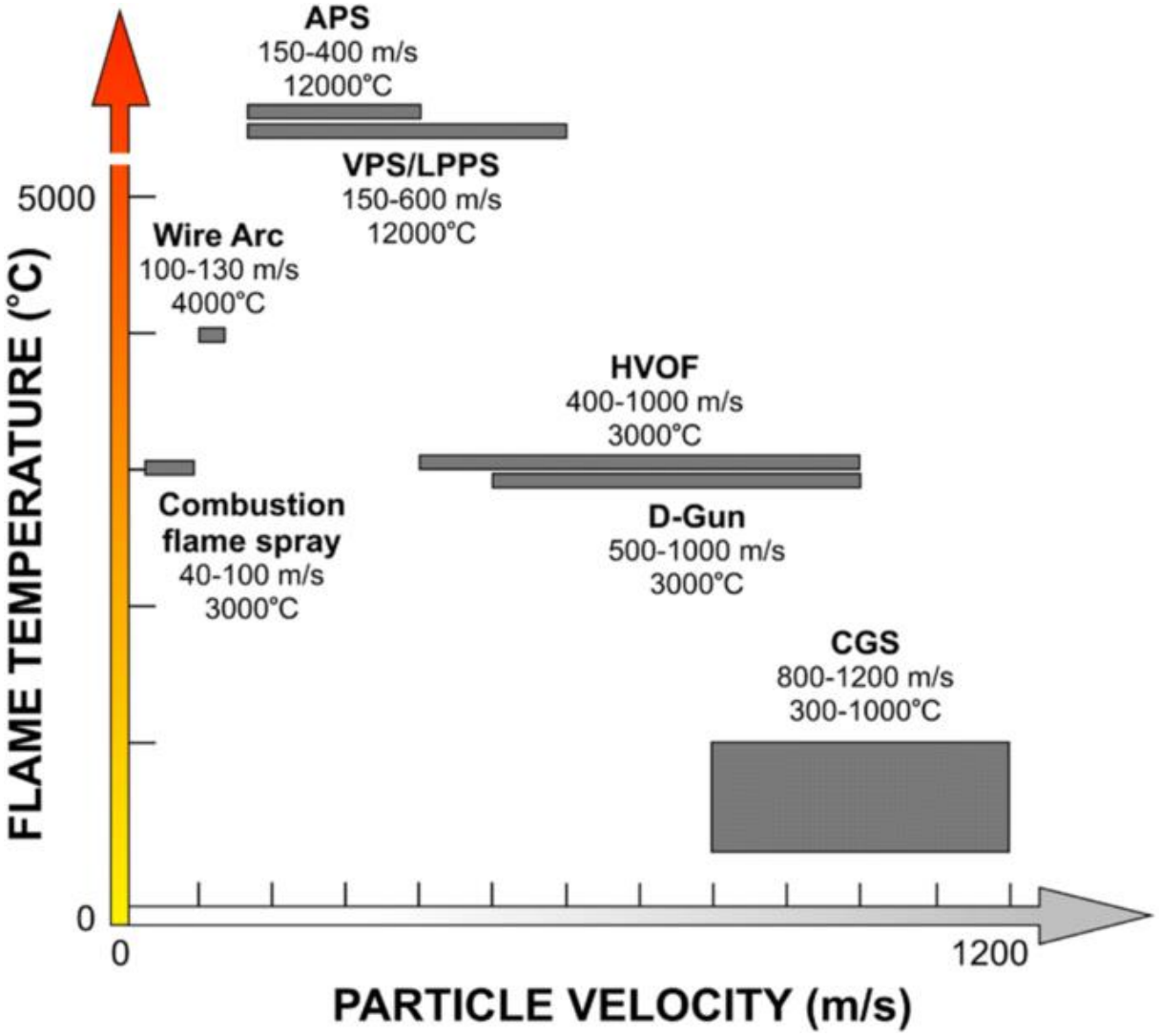

Figure 10 The principal difference in flame temperature and particle velocity among thermal spraying technologies [49]

2.4.1 High-velocity oxy-fuel spraying

The HVOF technology was developed at the beginning of the 1980s. The main principle of HVOF is based on the combustion of gas or liquid fuel mixed together with oxygen in the combustion chamber. The outgoing flow of gases heats and accelerates injected powders which impinge on the substrate surface at supersonic speed, see Figure 11 [48]. As the fuel in the HVOF process, gas (propane, ethane, propylene, acetylene, hydrogen, natural gas) or liquid (kerosene) can be used. The HVOF torch consists of (i) the combustion chamber where gas or liquid fuel and oxygen are introduced; (ii) convergent-divergent nozzle (de Laval nozzle) where exhaust flow of gases is accelerated up to supersonic speed; and (iii) radial or co-axial powder

injection. Due to intense heating during the spraying process, water cooling for the combustion chamber and the nozzle is typically used. Nitrogen is used as a carrier gas for powder transportation from the powder feeder to the HVOF torch. Usually, the powders of cermet composites containing carbides reinforcements and metallic alloys in size from 5 to 45 µm are used in HVOF spraying [50]. The supersonic speed of particles during spraying promotes their flattening at the moment of impact with the substrate and enables the formation of dense coatings (with low porosity of ~1%) and high adhesion to the substrate [42].

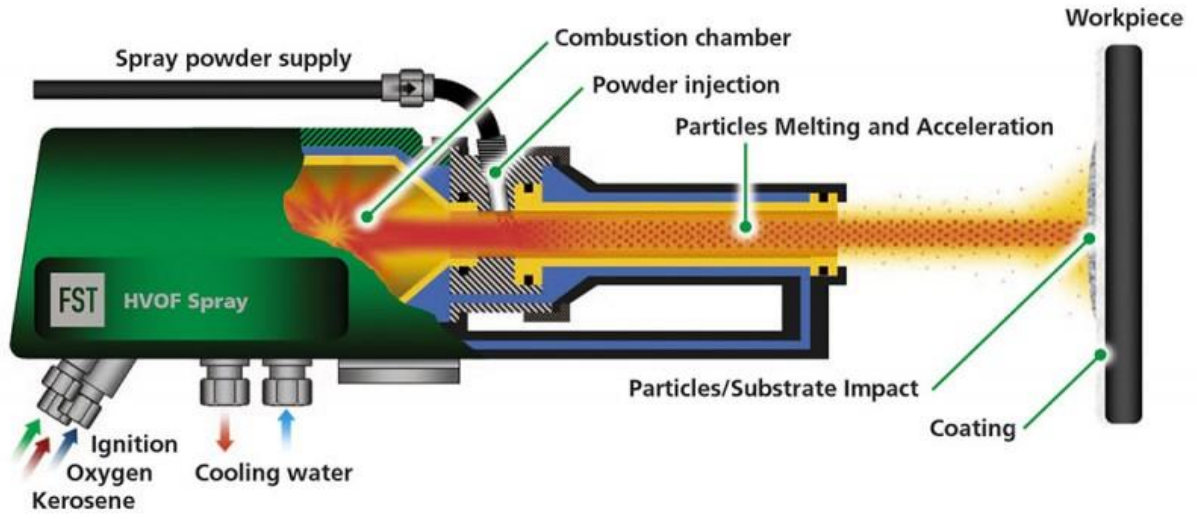

Figure 11 Schematic illustration of a high-velocity oxy-fuel spraying torch [51]

Coatings sprayed by HVOF technology are widely used in the automotive, aerospace and chemical industries. Examples include abrasion-resistant WC-Co/WC-Co-Cr coatings; M-CrAlY bond coats for gas turbine thermal barriers; Ni-based corrosion-resistant coatings for chemical reactions; and NiCr bond coats applied prior to spraying ceramic/cermet top coats by other thermal spraying techniques [50].

2.4.2 Plasma spraying

Atmospheric plasma spraying of powders

The utilization of plasma as a heating source for spraying was patented at the beginning of the 1960s [50]. At that time, the introduction of plasma plume into thermal spraying enabled the enlargement of a variety of spraying materials, such as ceramics.

Conventional plasma torches consist of one (e.g., F4MB) or more (e.g., Axial III, TriplexPro-210) thoriated tungsten cathode(s) and high-purity oxygen-free copper anode, see Figure 12. The plasma plume is created by the ionization and expansion of plasma forming gas via electric arc discharge. As plasma forming gases, technically pure Ar or mixtures of Ar+H_2,

Ar+N_2, Ar+He, Ar+H_2+He, Ar+N_2+He can be used [50]. The powder particles are injected into the plasma plume using Ar carrier gas through powder supply, see Figure 12. The powder injection can be radial (e.g., as in F4MB) or axial (e.g., as in Axial III). After injection into the plasma plume, powder particles are accelerated and rapidly heated up to a molten or partially molten state with the aim of impacting the substrate's surface and forming the coating.

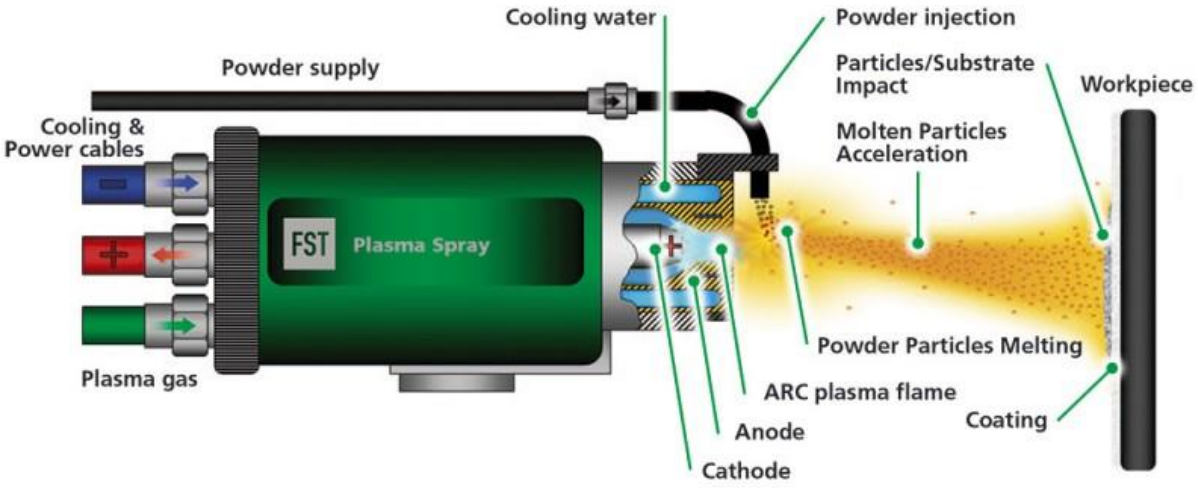

Figure 12 Schematic illustration of a single-cathode plasma spraying torch [52]

One of the alternatives to a conventional gas-stabilized plasma torch is the hybrid water-stabilized plasma torch (WSP-H), see Figure 13. The main difference of the WSP-H is in plasma forming gases. In the WSP-H torch, water steam and argon gas are used to create the plasma. The chamber of the WSP-H torch is divided into several sections where water is injected tangentially, and thus a vortex flow is created. This vortex flow of water surrounds and stabilizes the plasma plume. The plasma plume burns between the tungsten cathode and the water-cooled rotating anode.

Using plasma spraying (both conventional APS and WSP-H) enables the fabrication of coatings from different powder materials including ceramic, metallic, cermet, polymers, or a combination of them. Currently used plasma torches are capable of reaching very high temperatures of the plasma plume up to ~12 000° C for APS and up to 16 000° C for WSP-H torch [53]. The velocity of powder particles at the moment of impacting the substrate surface can reach ~400 m/s. The typical size of powder particles for atmospheric plasma spraying ranges from 20 up to 125 µm. Powder particles smaller than 20 µm produce agglomerates in the powder injection tube before reaching the plasma plume, resulting in difficulties in continuous feeding during the spraying process. The coatings microstructure of conventional APS is lamellar with splats boundaries, voids and porosity [50].

Using APS technology, it is possible to deposit the coatings with diverse properties such as abrasion resistant, cavitation erosion-resistant, electrically conductive or non-conductive, high-temperature corrosion-resistant coatings, with low-friction coefficient, oxidation resistant coatings, thermal barriers and many others [50].

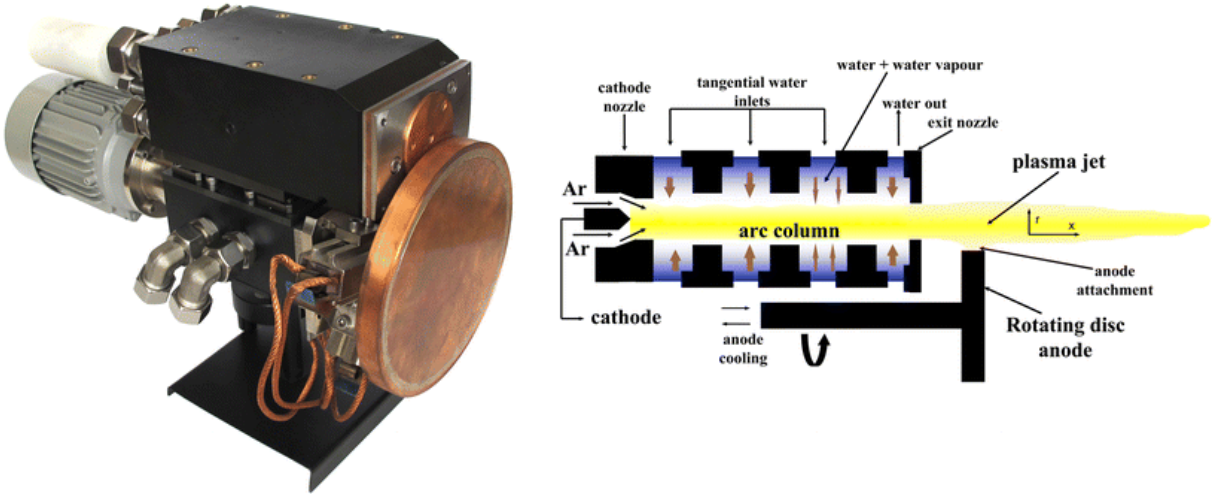

Figure 13 WSP-H 500 water-stabilized plasma torch [54]

Suspension plasma spraying

The principle of suspension plasma spraying (SPS) is the same as for atmospheric plasma spraying, with the only difference being in the state of the feedstock, see Figure 14. As spraying of powder particles with a size below 10 µm is problematic in the conventional atmospheric plasma spray technique, fabrication of coatings from nano- and submicron-sized powders can be done via suspension plasma spraying [55–58]. The content of powder particles in the suspension might vary from 2.5% up to 40% (wt.). Usually, preparation of in-lab made suspension consists of several steps: (i) dispersion of nano-, sub-micron or micron-sized powder in a solvent (typically in ethanol or in water, or in their mixture); (ii) addition of dispersant to prevent agglomeration and postpone sedimentation; and (iii) magnetic stirring or mechanical ball milling to ensure continuous mixing. There are also commercially available ready-to-spray suspensions [49, 57]. During the plasma spraying process, the suspension can be injected into the plasma plume radially (in the case of F4MB and WSP-H plasma torches) or axially (in the case of Axial III plasma torch) [57-59]. The utilization of suspensions with ultra-fine solid particles allows the production of coatings with finer and denser lamellar microstructure compared to conventional atmospheric plasma spraying. In addition to lamellar microstructure, see Figure 15a, it is possible to fabricate coatings with a columnar microstructure, see Figure 15b [61].

The application of liquid feedstock with ultra-fine powder particles in plasma spraying was found to be useful in producing solid oxide fuel cells, thermal barrier coatings, wear-resistant coatings, bio-active coatings and photo-catalytic coatings [57, 60–62].

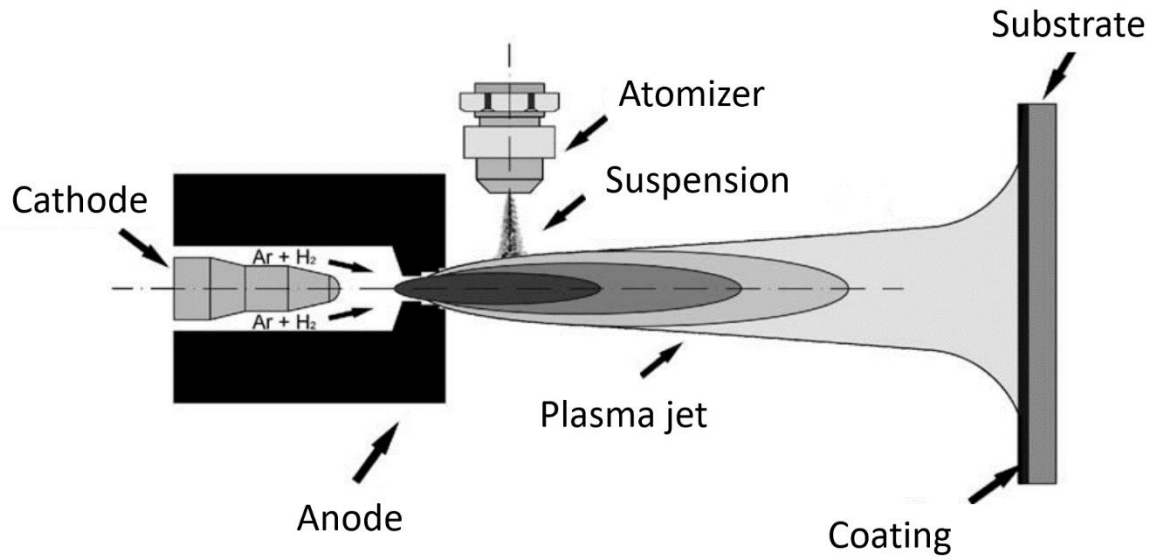

Figure 14 Schematic illustration of suspension plasma spraying with radial injection, adapted from [63]

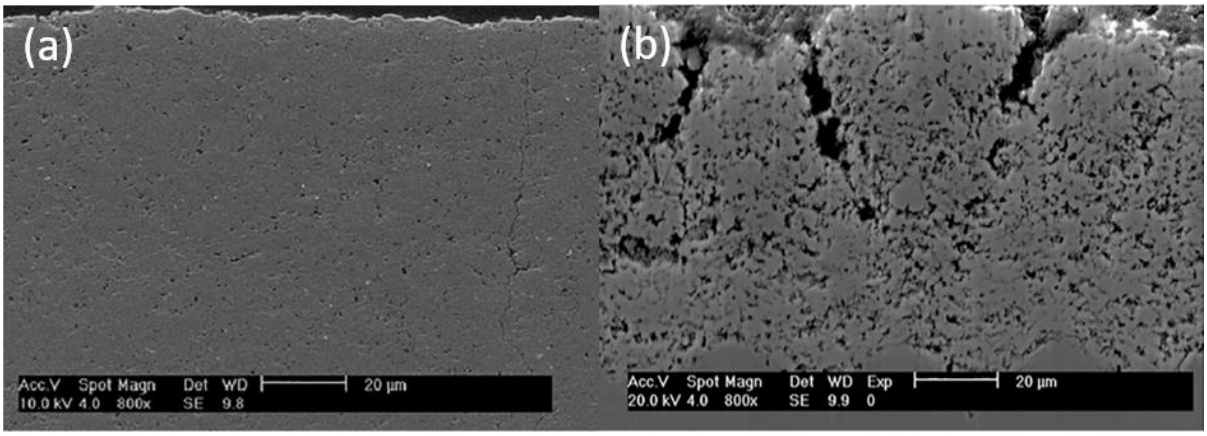

Figure 15 Representative examples of suspension plasma sprayed dense lamellar (a) and columnar (b) microstructure [61]

2.5 Thermally sprayed coatings with hydrophilic/hydrophobic wetting behavior

Several attempts to fabricate thermally sprayed coatings with superhydrophilic/hydrophilic properties were made. Suspension- and powder-flame spraying were used separately to form the final bi-modal thin film of TiO_2 with superhydrophilic behavior [64]. The APS was utilized to deposit hydrophilic Ti-coatings onto PEEK substrate for medical applications [65]. Ghosh et al. [66] fabricated slippery WC-Co coatings employing the HVOF technique. These

coatings were hydrophobic (with WCA of 103° and SA of 41°) in the as-sprayed state, that was turned into the hydrophilic slippery surface (with WCA of 60° and SA of 20°) after nano finishing by shape adaptive grinding machine [66].

In the case of hydrophobic and superhydrophobic coatings, two approaches with low-surface energy organic materials mainly were used: (i) modification of the initial feedstock [67, 68]; and (ii) subsequent post-treatment of the coating [69, 70]. All coatings exhibited very high WCA above 150° and small SA below 10°. Several studies reported on hydrophobic/superhydrophobic behavior without the application of low-surface energy organic materials as well. For instance, Qiao et al. [71] provided additional laser-texturing surface treatment onto HVOF sprayed WC-Co-Cr coatings that increased WCA up to 136.5°. Vijay et al. [72] reported on HVAF sprayed WC-Co-Cr coatings with multi-scale surface topography with the WCA of 135.1°. The formation of the multi-scale surface topography is explained by the presence of fine carbides on the surface. Xi et al. [73] deposited WC-Co coatings using HVOF that showed hydrophobic behavior in the as-sprayed state with WCA of 123° ± 2.3°. In order to improve coatings' hydrophobicity, surface modification by additional deposition of hydrophobic nano-SiO_2 powder was done and the WCA of the coatings was increased up to 154.3° ± 3.0°.

Another direction in the fabrication of hydrophobic/superhydrophobic coatings is the spraying of rare-earth elements' oxides. Highly hydrophobic behavior (WCA ~ 139°) was reported on CeO_2 plasma sprayed coatings in the as-sprayed state [46]. Bai et al. [74] reported on the hydrophobic behavior of CeO_2 suspension-HVOF sprayed coatings with WCA in the range of 134° to 146°. Xu et al. [24, 47] fabricated Yb_2O_3 utilizing solution precursor atmospheric plasma spraying (SPAPS) and solution precursor vacuum plasma spraying (SPVPS) that showed superhydrophilic behavior in the as-sprayed state. The superhydrophobic state was obtained after 12 hours of vacuum treatment. However, the robustness of the superhydrophobic/hydrophobic behavior leaves much to be desired as it was completely lost after 10 min at 300° C, and coatings became superhydrophilic [24]. After the sand erosion test of Yb_2O_3 SPAPS and SPVPS coatings, the decrease of the WCA from 163° to 96° (for SPAPS) and from 155° to 140° (for SPVPS) was observed after only 5 cycles of testing.

3 Aims of the thesis

The main aim of the thesis is to develop a technology to fabricate wear-resistant hydrophobic/hydrophilic coatings employing the thermal spraying process; and to provide the detailed analysis of the produced coatings, assessment of their mechanical properties and robustness of the wetting behavior.

To fulfill the main aim of the thesis, the following steps were designed and performed:

- Spraying of wear-resistant coatings from commercially available powders, namely Al_2O_3, Cr_2O_3-SiO_2-TiO_2, ZrO_2-Y_2O_3 (YSZ) and WC-Co-Cr using APS technique;
- Study of the plasma sprayed coatings in the as-sprayed state and after #220 abrasive paper, 9 µm, 3 µm and 1 µm diamond suspensions (grinding and polishing) in order to determine a correlation between surface topography parameters and water wetting behavior;
- Spraying of YSZ coatings using ultra-fine powder particles in suspension feedstock to study the effect of different types of microstructure (lamellar vs. columnar) onto wetting behavior in the as-sprayed state;
- Improvement of the wetting behavior up to superhydrophobic state of suspension plasma sprayed YSZ coatings via additional surface modification;
- Investigation of the fabricated modified and unmodified YSZ coatings via SEM, EDX, topography analysis, and determination of their water contact angles;
- Fabrication of the wear-resistant WC-Co-Cr coatings from three different powders (coarse, coarse with ultra-fine WC, and fine with ultra-fine WC) employing HVOF spraying in order to obtain multi-scale surface roughness;
- Development of a technologically simple way to amplify hydrophobicity of the coatings surface;
- Detailed characterization of the WC-Co-Cr coatings through SEM, EDX, XRD, XPS and assessment of topographical features, water contact angles and surface free energies in four states, namely (i) as-sprayed, (ii) as-sprayed modified, (iii) polished and (iv) polished modified;
- Carrying out the slurry abrasion response test and cavitation erosion test on the WC-Co-Cr coatings in the as-sprayed and as-sprayed modified states to estimate the robustness of the wetting behavior.

4 Experimental design and methods

In order to fulfill the aims and obtain the results, structural observation, surface chemistry and phase analysis, surface topography investigation, water contact angle measurements, free surface energy evaluation, wear-resistance and cavitation erosion tests were conducted. The flowchart of the experimental design is presented in Figure 16.

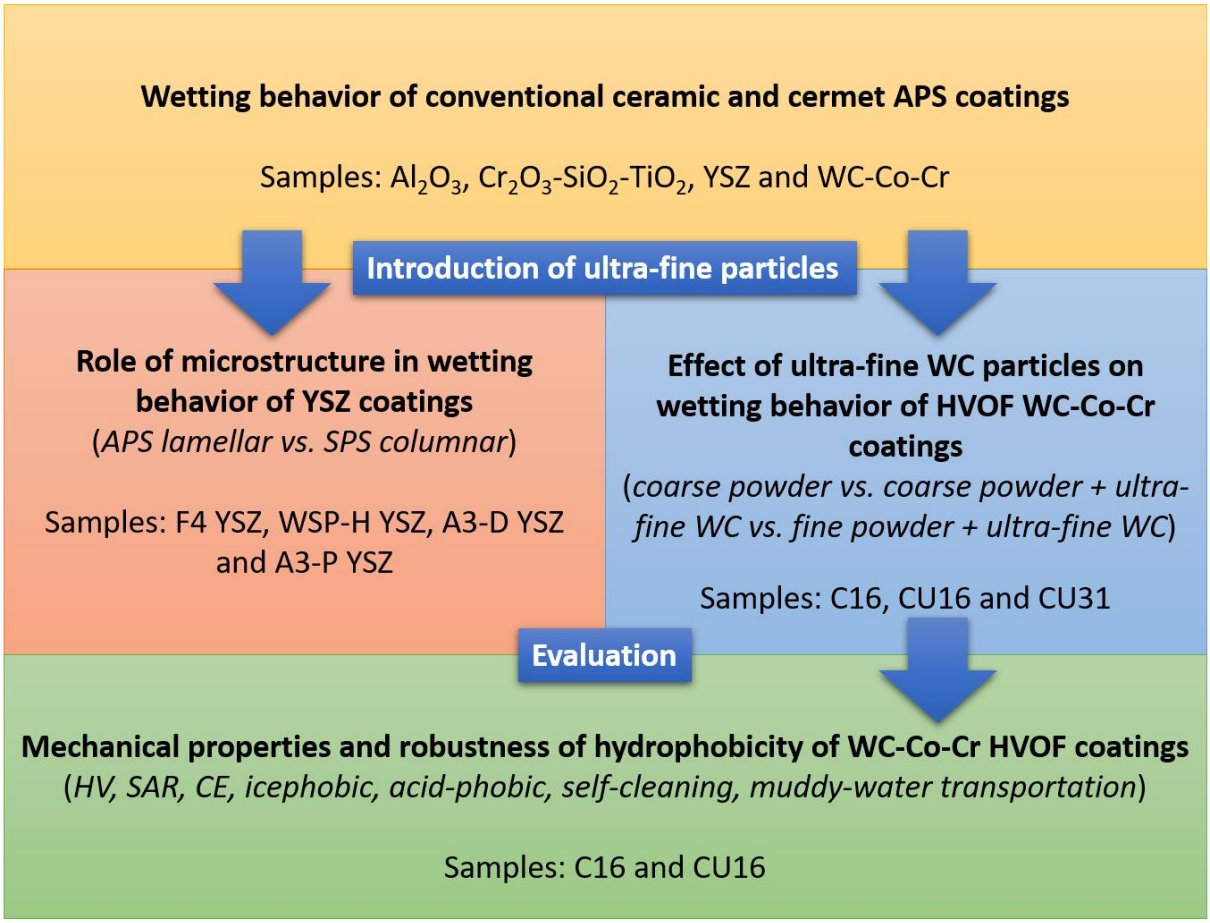

Figure 16 The flowchart of the experimental design used in the present work

At first, it was decided to make screening and spray commercially available wear-resistant ceramic (Al_2O_3, Cr_2O_3-SiO_2-TiO_2, ZrO_2-Y_2O_3 (YSZ)) and cermet (WC-Co-Cr) powders by using the APS technique. This step was done with the aim of obtaining the first experience on how the water will behave on a surface of conventional coatings widely used in the industry. The spraying process of all aforementioned powders was performed in cooperation with S.A.M. – metalizační společnost s.r.o. (Brno, Czech Republic).

Based on the obtained results, YSZ and WC-Co-Cr materials were selected for further research: (i) to estimate the influence of different parameters of plasma spraying of YSZ powder and suspension with ultra-fine particles on coating microstructure and wetting behavior; (ii) to investigate the wettability of WC-Co-Cr coatings fabricated by HVOF spraying utilizing three

different feedstocks (coarse powder, coarse powder with ultra-fine WC and fine powder with ultra-fine WC); and (iii) to provide additional surface treatment. In this research stage, spraying of YSZ suspension was done at the Institute of Plasma Physics of the Czech Academy of Science (Prague, Czech Republic) and at the Institute of Energy and Climate Research, Forschungszentrum Jülich GmbH (Jülich, Germany).

The final part of the experimental work focused on evaluating the mechanical performance of the produced WC-Co-Cr coatings and assessing the robustness of their wetting behavior, including short-term testing on icephobic, acid-phobic, muddy-water transportation and self-cleaning performance.

4.1 Thermal spraying process

An APS set-up (APS MF-P-1000 (GTV, Germany), equipped with the F4MB-XL plasma torch (Oerlikon Metco, Switzerland), was used to produce coatings from commercially available powders on metallic substrates. As a substrate, the coupons of C45 construction steel (diameter 25.4 mm, height 5 mm) were used. Before spraying, the substrates were grit blasted by corundum particles with the aim of activating the surface and assuring the proper surface roughness for better mechanical interlocking of the coating. In order to improve the adhesion of the ceramic coatings to the substrate, the bond coats from the NiCr (Amperit 251, Höganäs AB, Germany) powder feedstock were sprayed first. After spraying of the bond coats, the top coats from Al_2O_3 (40.05.1G, GTV, Germany), $92Cr_2O_3$-$5SiO_2$-$3TiO_2$ (40.36.7G, GTV, Germany), $92ZrO_2$-$8Y_2O_3$ (YSZ) (40.23.1G, GTV, Germany) and 86WC-10Co-4Cr (80.76.1G, GTV, Germany) were sprayed. The initial powders and spraying parameters used are listed in Table 3.

Hybrid water-stabilized plasma torch WSP-H 500 (ProjectSoft HK a.s., Czech Republic) was used to spray YSZ ethanol-based suspension with 25 wt.% of suspended solid particles [54].

Table 3 Atmospheric plasma spraying parameters

Feedstock	Ar [slpm]	H_2 [slpm]	Current [A]	Spray distance [mm]
NiCr	45	11	600	140
Al_2O_3	41	14	530	120
$92Cr_2O_3$-$5SiO_2$-$3TiO_2$	40	13	650	110
$92ZrO_2$-$8Y_2O_3$	40	12	630	80
86WC-10Co-4Cr	55	4	700	140

To estimate the suspension spraying conditions of YSZ coatings on wetting behavior, two sets of samples with different spraying trajectories were fabricated using the Axial III high-power plasma torch (Northwest Mettech Corporation, Canada), see Table 4. The difference between two sets of samples was in the robot's movement trajectory. The trajectory for the A3-D YSZ sample was shorter, as well as the cooling time of the sample during spraying, in comparison to the sample A3-P YSZ. Laboratory made ethanol-based suspension with 5 wt. % of YSZ solid content, see Figure 17 (mixed TZ-5Y and TZ-3Y powders, Tosoh Corporation, Japan), was used to deposit coatings onto the metallic substrate. Before YSZ top coat deposition, grit blasting and bond coat spraying were performed.

Table 4 YSZ suspension plasma spraying parameters for Axial III plasma torch

Sample	Ar [slpm]	H_2 [slpm]	N_2 [slpm]	Current [A]	Spray distance [mm]	Robot trajectory [mm]
A3-D	184	36.5	24.5	230	70	200 * 2 *16
A3-P						320 * 2 * 16

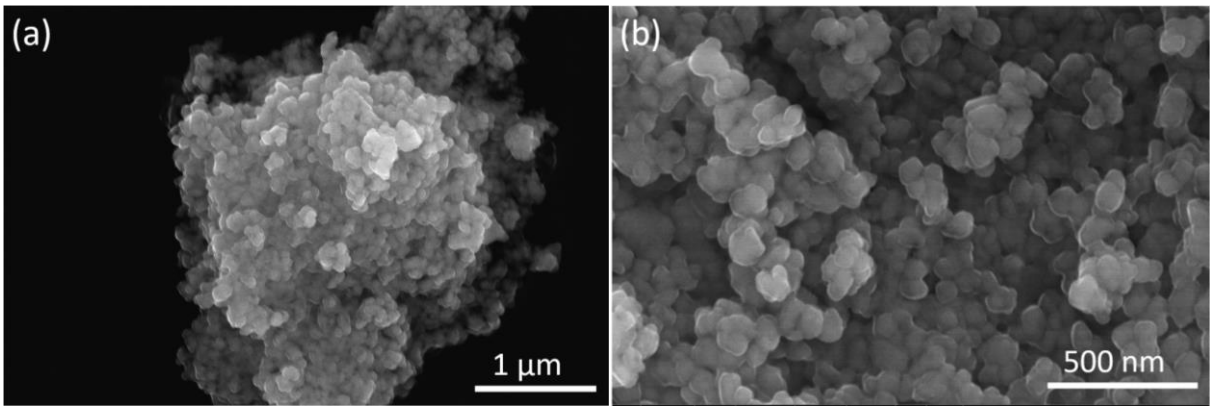

Figure 17 SEM micrographs of (a) YSZ powder used in suspension and (b) its detail

The high-velocity oxy-fuel spraying technique (GLC 5 HVOF torch, GTV, Germany) was used for further investigation of WC-Co-Cr coatings and their wettability. Three series of cermet coatings were fabricated from commercially available agglomerated and sintered powders GP10C-16, GP10CU-16 and GP10CU-31 (XTC, China) with different distribution of particle size (i) coarse, (ii) coarse with ultra-fine WC and (iii) fine with ultra-fine WC, respectively. The morphology of powder particles is shown in Figure 18. The coatings henceforth are designated as C16, CU16 and CU31 based on the powder feedstock. As

substrates, AISI 304 stainless steel coupons (30 mm * 10 mm) with NiCr (Amperit 251, Höganäs AB, Germany) bond coat (~150 µm thickness) were used. Here, stainless steel was used as a substrate because of the planned testing of coatings by the slurry abrasion response test and the cavitation erosion resistance tests performed in artificial seawater. Prior to spraying, grit blasting of metallic substrates with alumina particles and cleaning in an ultrasonic bath were provided to improve surface roughness for better adhesion strength of the coating and to remove organic contaminations, respectively. Before each spraying run, the substrate temperature was kept in the range of 30-40 °C. To record in-flight behavior (temperature and velocity) of powder, an AccuraSpray G3C system (Tecnar Automation, Canada) was used and measurements were done at the distance of 200 mm. Spraying parameters, feedstock powder description and in-flight powder characteristics are summarized in Table 5.

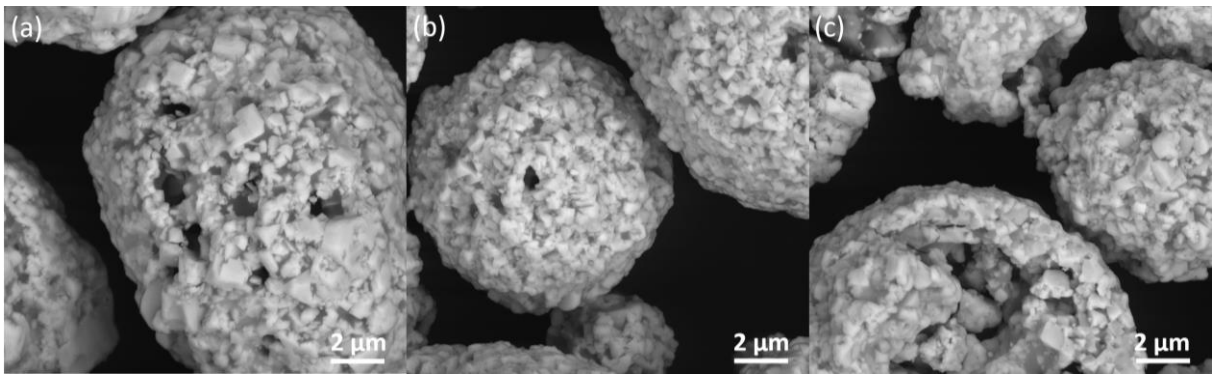

Figure 18 Morphology of (a) GP10C-16, (b) GP10CU-16 and (c) GP10CU-31 powders, where WC particles (white color) embedded into Co-Cr matrix (light gray color)

Table 5 Spraying parameters and feedstock powder description

Coating designation	C16	CU16	CU31
Feedstock powder	GP10C-16	GP10CU-16	GP10CU-31
Powder chemical composition [wt. %]	86WC-10Co-4Cr		
Agglomerate size [µm]	-25+5		-10+2
WC carbides size [µm]	> 0.5	< 0.5	
Ethylene [slpm]	96		
Oxygen [slpm]	252		
Spray distance [mm]	200		
Robot movement speed [mm/s]	600		
In-flight particle velocity [m/s]	~610	~615	~680
In-flight particle temperature [°C]	~2200	~2130	~2020

4.2 Samples' surface modification

Surface modification of YSZ samples was done by a radio-frequency (RF) plasma jet developed at Masaryk University (Brno, Czech Republic). It was reported elsewhere [75] that RF-plasma surface treatment improves hydrophobic performance on the glass surface. A schematic illustration of the RF-plasma device used for this purpose is presented in Figure 19. Apparatus constiting of a 1-1000 W RF power supply operating at 13.56 MHz, with an LC matching unit for power loss elimination and silicon capillary jet. As a carrier gas, argon with the addition of hexamethyldisiloxane (HMDSO, 98.5%, Sigma Aldrich) was used. The HMDSO was introduced to the RF-plasma jet in vapor form using bubbler and secondary carrier argon flow. Deposition of the hydrophobic layer was carried out at the constant conditions, i.e., input power 150 W, deposition time 40 s, the distance between the sample surface and jet orifice of 3 cm, main argon flow 5 l/min and additional argon flow carrying HMDSO vapors 2 l/min.

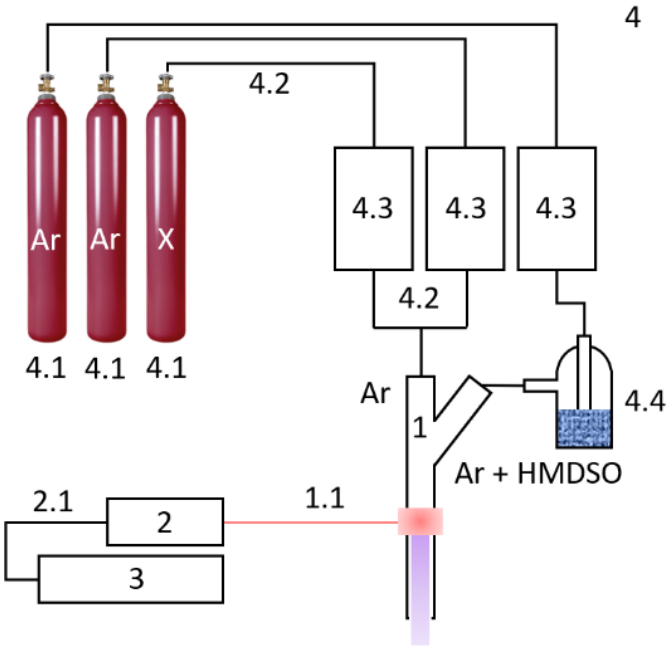

Figure 19 RF plasma jet system - 1 – capillary plasma jet; 1.1 – RF electrode; 2 – LC matching unit; 2.1 – coaxial cable; 3 – RF supply (13.56 MHz); 4 – gas distribution; 4.1 – gas storage; 4.2 – tube/hose connections; 4.3 – flowmeter; 4.4 – bubbler.

Regarding the surface chemistry modification of HVOF cermet coatings (C16, CU16 and CU31), a technologically simple way to improve hydrophobicity of the coatings using a hydrophobic agent was developed and applied. Silicon oil (Novato, Czech Republic) on a polydimethylsiloxane (PDMS) basis was chosen for this study due to its availability and low purchasing cost. The mixture of oil and isopropyl alcohol (50/50 vol. %) was sprayed onto the coatings' surface from a distance of 300 mm under the angle of 90°, see Figure 20.

Subsequently, these modified samples were put under the vacuum of 1×10^{-1} Pa pressure to let the thin oil coating mixture penetrate the thermal sprayed coating to fill the open interconnected pores. Following that, the samples were cured in a furnace at a temperature of 350 °C for 30 min. After curing, a very thin transparent layer was present on the coating's surface. The silicone oil treatment was used with the aim of (i) providing superhydrophobic behavior and to (ii) eliminating the influence of initial as-sprayed coating surface chemistry, in order to study the role of surface topography in the wetting behavior.

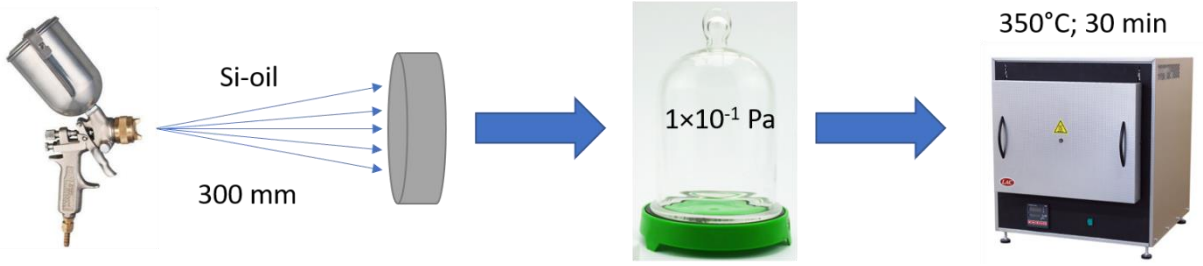

Figure 20 Illustration of silicone oil surface treatment

4.3 Samples' surface preparation

The Al_2O_3, Cr_2O_3-SiO_2-TiO_2, YSZ and WC-Co-Cr plasma sprayed coatings were studied in the as-sprayed, ground (after #220 abrasive paper and 9 µm diamond suspension) and polished (after 3 µm and 1 µm diamond suspensions) states, in order to understand the influence of surface topography of commercially utilized coatings on their wetting behavior. The YSZ coatings (namely A3-D and A3-P) sprayed from suspension were analyzed in as-sprayed and as-sprayed modified states (after RF-plasma treatment). Cermet coatings of WC-Co-Cr (C16, CU16 and CU31) were evaluated in the as-sprayed, polished, as-sprayed modified and polished modified (after Si-oil treatment) states. These are further termed as AS (as-sprayed), P (polished), AS-M (as-sprayed modified) and P-M (polished modified).

Polishing was performed using diamond suspensions, starting from 9 µm down to 1 µm diamond abrasive particles in size, until the surface root mean square height *Sq* was ≤ 0.20 µm and the surface roughness factor *Rs* was < 1.01. These polished samples were prepared in order to eliminate the influence of surface topography and thus to determine the effect of phase composition and surface chemistry on wetting behavior and free surface energy values.

4.4 Coatings characterization

4.4.1 Microstructure, elemental and phase analysis

Investigation of samples cross-sections of atmospheric plasma sprayed coatings was carried out by using an optical microscope Olympus DSX 510 (Olympus, Japan). Details of the microstructures were observed by scanning electron microscopes LYRA3 (Tescan, Czech Republic) and Verios 460L (Thermo Fisher Scientific, USA). Energy-dispersive X-ray spectroscopy was performed using an X-ray spectrometer XFlash 5010 detector (Bruker, USA) equipped on LYRA3 SEM. The XRD SmartLab 3kW diffractometer (Rigaku, Japan) in the Bragg-Brentano geometry with Cu-Kα radiation (λ = 0.154 nm) with a current of 30 mA and voltage of 40 kV was used to investigate the phase composition of thermally sprayed coatings. The diffractograms were taken from 20° to 90° with 0.02° step size and 1 s of the scan time. X'Pert Highscore v.3a software with implemented Rietveld refinement method was used for qualitative and quantitative phase analysis of diffraction patterns. Following crystallographic models from the International Crystallographic Database were applied to determine detected phases, i.e. Al_2O_3 (ICSD 98-002-8260; 98-000-9770), Cr_2O_3 (ICSD 98-002-5781), SiO_2 (ICSD 98-003-4927), Cr (ICSD 98-062-5712), CoO (ICSD 01-070-2855), W_2C (ICSD 98-003-0008; 98-007-7568), W (ICSD 01-089-3012), WC (ICSD 98-001-5406; 01-072-0097), CrN (ICSD 98-005-3146), WO_2 (ICSD 98-000-8217) and YSZ (ICSD 98-007-5309; 98-007-5310; 92-006-2994).

The crystallinity was calculated in the Highscore v.3a software using the "constant background intensity" method. The crystallinity *C* [%] was determined using the Eq. 9:

$$C = \frac{100 * \sum I}{\sum I_{total} - \sum I_{const.bgr.}} \quad (9)$$

where ΣI is the area of crystalline peaks, ΣI_{total} is the total diffraction pattern area and $\Sigma I_{const.bgr}$ is the area of constant background, which is subtracted from the total intensity [76].

4.4.2 Surface chemistry analysis

XPS analysis was performed at a Kratos Analytical Axis Supra spectrometer (KRATOS-XPS, Kratos Analytical Ltd., UK), with a monochromatic Al source at 80 eV pass energy for wide spectra and at 20 eV for high-resolution spectra of C 1s, O 1s, W 4f, Co 2p and Cr 2p peaks. The scanned area of the coating surface was 300×700 μm^2. For post-processing and deconvolution of the aforementioned peaks, the CasaXPS 2.3.22PR 1.0 software with synthetic peak models and constraints supported by the existing literature was used [77–81]. As

wettability of the solid surface is dependent on the chemistry of the very thin surface layer, X-ray photoelectron spectroscopy (XPS) was carried out onto as-sprayed, polished and polished modified surfaces of C16, CU16 and CU31 coatings to investigate the surface chemical composition. Additionally, XPS analysis was carried out onto WSP-H, A3-D and A3-P YSZ samples with a columnar microstructure. All the samples were cleaned in the ultrasonic bath with isopropyl alcohol and further dried by hot air before measurements.

4.4.3 Surface topography characterization

The detailed surface features of thermally sprayed coatings were recorded by the scanning electron microscope LYRA3. The quantitative data of coatings surface topography was measured by an optical profilometer MicroProf-100 (Fries Research and Technology Gmbh, Germany) and an optical laser confocal microscope LEXT OLS 4100 (Olympus, Japan). The data obtained from MicroProf 100 and LEXT OLS 4100 was post-processed in Gwyddion 2.53 open-source software. Post-processing consisted of (i) *mean plane subtraction* to provide plane leveling of the data/figure, and (ii) *Kuwahara filtering*, which is an edge-preserving smoothing technique, used in order to eliminate the noise and the artifacts from data/figure. Only these two aforementioned steps were selected because they did not significantly change the measured data. Five regions of 5 mm^2 and/or ~600 μm^2 areas were analyzed for each sample surface topography investigation. The larger area (5 mm^2) was used only for comparative surface topography analysis of the coatings sprayed from solid feedstock, where powder particles were in the size of tens of microns. A smaller surface area of ~600 μm^2 was selected in order to detect fine and ultra-fine topographical features (below 3 µm). The analysis of ~600 μm^2 area was then performed for polished surfaces (to detect small-sized valleys/pores and peaks), for suspension plasma sprayed coatings (as suspended powder particles were below 3 µm in size) and for HVOF WC-Co-Cr coatings produced from bi-modal feedstock (as it contained ultra-fine WC particles).

The coatings surface topography was characterized by the surface arithmetic mean height (*Sa*), the root mean square height (*Sq*), the skewness (*Ssk*), the kurtosis (*Sku*) and the surface roughness factor (*Rs*) in order to investigate the role of topography on wetting behavior. The surface arithmetic mean height *Sa* and the root mean square height *Sq*, which are the areal analogs of widely used profile arithmetical mean height (*Ra*) and profile root mean square height (*Rq*), provide information on the vertical extent of a surface. The skewness describes whether the surface has predominantly high peaks ($Ssk > 0$) or deep valleys/pores ($Ssk < 0$); the kurtosis reveals if the peaks and valleys are sharpened ($Sku > 3$) or flattened ($Sku < 3$), see Figure 21.

The developed interfacial area ratio *Sdr*, which is defined in the ISO 25178-2 standard [82], can be used to explain the complexity of the coatings surface topography. This *Sdr* parameter was found to be useful in describing the wetting behavior of cermet-based surfaces [72]. However, in this study, the surface roughness factor *Rs* is used instead of *Sdr* because *Rs* appears in the Wenzel (Eq. 6) [16, 17] and in the combined Wenzel-Cassie-Baxter (Eq. 8) [21] models of wetting. The surface roughness factor *Rs* shows the ratio of "true" surface area per its projection and *Rs* directly correlates with *Sdr* as $Rs = Sdr + 1$ [83].

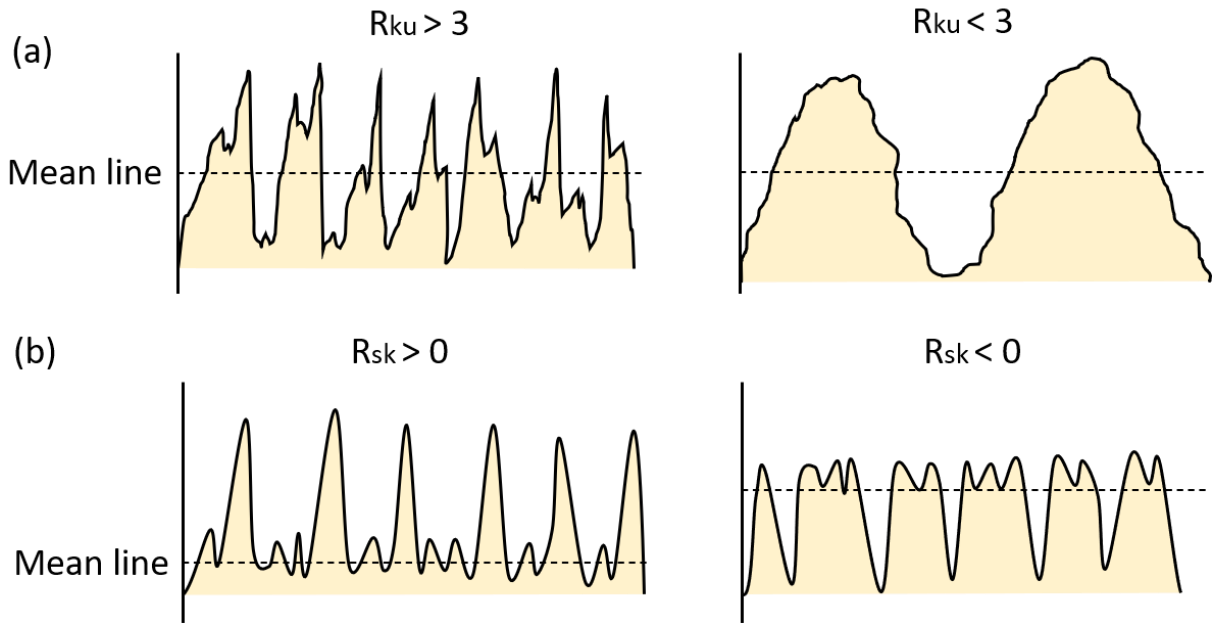

Figure 21 Illustration of (a) kurtosis *Rku* and (b) skewness *Rsk* on different profiles; *Rku* and *Rsk* are profile analogs of *Sku* and *Ssk*

4.5 Wetting behavior and surface free energy measurements

The surface energy values and the data on the water wetting behavior of experimental samples were obtained from the sessile droplet method using See System E (Advex Instruments, Czech Republic) with eponymous image analysis software. Before measurements, each samples' surface was cleaned in an ultrasonic bath with isopropyl alcohol and dried by hot air to remove dust and organic impurities from the coating's surface. During the sessile droplet method for WCA and SFE measurements, 10 droplets of 3 µl of a liquid were deposited onto the surface of a coating, and the angle of the "vapor-liquid-solid" interphase line was measured. These tests were conducted at room temperature. The small volume of liquid was used to reduce the impact of gravitational force on the shape of the droplets.

The sessile droplet method on a smooth solid surface is based on Young's equation (Eq.1), where the solid surface free energy, the solid/liquid interfacial free energy, the liquid surface

tension and the contact angle parameters are included. Calculation of the SFE was carried out using the Owens-Wendt model. For these measurements, sets of water and diiodomethane droplets were deposited onto the solid surfaces with further evaluation of their contact angles. All calculations were provided by the See System E software.

4.6 Mechanical properties and wear/erosion resistance of hydrophobic/superhydrophobic coatings

Prior to wear-resistant tests, all the superhydrophobic coatings were subjected to the water-flush test for ~5 min using tap water [24]. Only the WC-Co-Cr modified coatings did not show any degradation of the wetting behavior after this short test, therefore, these samples were chosen for further analysis.

The mechanical properties of HVOF sprayed WC-Co-Cr coatings were evaluated using the Vickers microhardness test. Due to the absence of standardized methods for assessment of the mechanical robustness of the hydrophobic/superhydrophobic behavior, the slurry abrasion response (SAR) and the cavitation erosion (CE) resistance tests were used.

The SAR test is commonly applied to rank the materials that are used for pumps and in the fluid transport systems. The CE resistance test is directed to estimate the resistance of the materials against cavitation damage. Such damage occurs in hydraulic turbines, bearings, ship propellers, valves, spillways, etc. The two C16 and CU16 representatives with the highest hydrophobic performance were selected for SAR and CE resistance tests.

Additionally, the Vickers microhardness measurements were carried at the samples cross-sections by an average of at least 12 indents with HV 0.3 load using DeraScan G75 tester (Struers, Germany).

The slurry abrasion response test (ASTM G75 Standard Test Method for Determination of Slurry Abrasivity (Miller Number) and Slurry Abrasion Response of Materials (SAR Number)) [84] is a wear-resistant test where the samples are exposed in a slurry media and wear against the rubber with a pre-setup force of 22.24 N with 48 cycles per minute, see Figure 22a. The duration of the test was 6 hours, split into three 2-hours sessions. As a slurry, the mixture of artificial seawater (ASW) and 50 wt. % of Al_2O_3 (30 – 50 μm in size) was used. The as-sprayed modified and unmodified samples were tested as follows: (i) unmodified samples were tested for 6 hours (17 280 cycles) with topography and WCA measurements after 4 and 6 hours of testing; (ii) modified samples were tested for 1 minute (48 cycles) until the coatings' superhydrophobic behavior was lost. The unmodified samples were examined after 4

and 6 hours because it was a period when the wetting behavior of the coatings was changed from hydrophobic to hydrophilic.

The cavitation erosion resistance test (ASTM G32 – 16 Standard Test Method for Cavitation Erosion Using Vibratory Apparatus) [85] was performed using an alternative method where the coating surface was facing the horn of the vibration apparatus (Sonopuls Ultrasonic Homogenizer HD 3400, Bandelin, Germany) with a frequency of 20 kHz and an amplitude of 50 µm, see Figure 22b. The distance between the horn and the coating surface was 0.5 mm. The as-sprayed hydrophobic samples were tested until the hydrophobic behavior was lost; that was 165 min for the C16 sample and 120 min for the CU16 sample. The superhydrophobic coatings were tested for 20 minutes and terminated once the superhydrophobic effect was lost. The cumulative mass loss, coatings' surface top-view and wetting behavior changes were observed and evaluated after the test.

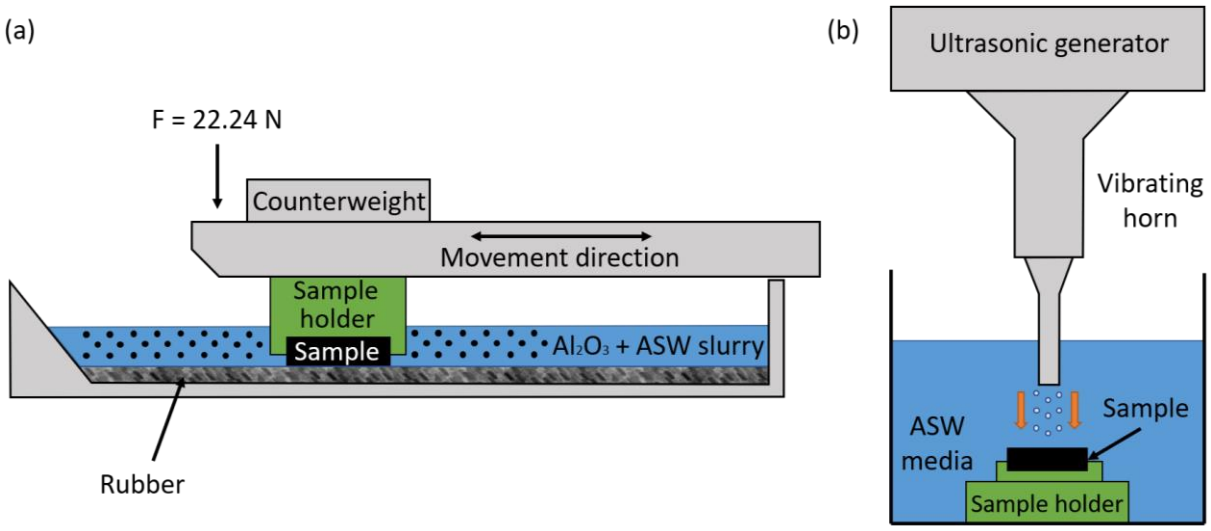

Figure 22 Slurry abrasion response (a) and cavitation erosion (b) tests

Several short-term tests for icephobic, acid-phobic, self-cleaning and muddy-water transportation performance of superhydrophobic C16 and CU16 coatings were also performed. The preliminary estimation of the icephobic behavior was conducted on superhydrophobic (C16/CU16 AS-M) and hydrophobic (C16/CU16 AS, C16/CU16 P-M) coatings in comparison to bare aluminum and stainless-steel substrates. During the test, several 3 µl droplets of deionized water were dripped onto the solid surface of a coating/substrate, and immersed into the laboratory freezer with -10° C temperature in order to froze the water droplets. After complete freezing, the contact angle between the ice-droplet and the solid surface was evaluated.

For analysis of "acid-phobic" performance, a droplet of the mixture of sulfuric acid in water (4.7 M, 9.3 M and 14 M) and pure sulfuric acid was dripped onto the surface of C16/CU16 AS and C16/CU16 AS-M coatings. The contact angle between the liquid droplet and solid surface was estimated.

For the self-cleaning test, the sample was covered by fine alumina powder particles (below 1 μm in size) and tilted at the angle of ~10°. Then, the water droplets were sent to the surface with the aim of sliding off and collecting the alumina powder particles.

The muddy-water transportation test was carried out via sending the continuous flow of a water-based slurry consisting of ultra-fine WC powder particles (50 wt. %) on the coating's surface that was tilted at the angle of ~10°.

5 Results and discussion

5.1 Wetting behavior of YSZ, Al_2O_3, Cr_2O_3-SiO_2-TiO_2 and WC-Co-Cr plasma sprayed coatings

5.1.1 Microstructure and phase composition

Analysis of cross-sections of atmospheric plasma sprayed coatings showed that the coatings consisted of compact splat-like or lamellar microstructure with a low number of unmelted particles, see Figure 23. Based on the results of the digital image analysis, the thickness of the coatings was in a range from ~290 μm to ~780 μm and the porosity ranged from ~3 % to ~7 %, see Table 6. The presence of vertical and randomly oriented cracks was observed in the YSZ and Cr_2O_3-SiO_2-TiO_2 coatings, respectively, Figure 23a and Figure 23c. The XRD measurements and Rietveld refinement, see Table 6, confirmed the decomposition of initial powder feedstock of Cr_2O_3-SiO_2-TiO_2 and WC-Co-Cr coatings with the formation of Cr and W_2C phases, respectively. The presence of WO_2, CrN and CoO phases, Table 6, suggests that molten or partially molten powder particles of WC-Co-Cr decomposed and interacted with the atmosphere during plasma spraying. In the case of coatings sprayed from the initial Al_2O_3 feedstock, the XRD analysis revealed the formation of η-Al_2O_3 (~94%) with a small amount of α-Al_2O_3 (~6%). The coatings of yttria-stabilized zirconia (YSZ) consisted only of a metastable tetragonal ZrO_2-Y_2O_3 (t`-YSZ) phase, which is typical for plasma sprayed YSZ deposits. Based on XRD analysis, all of the coatings were supposed to show attraction to water, since they mostly consisted of intrinsically hydrophilic ceramic components.

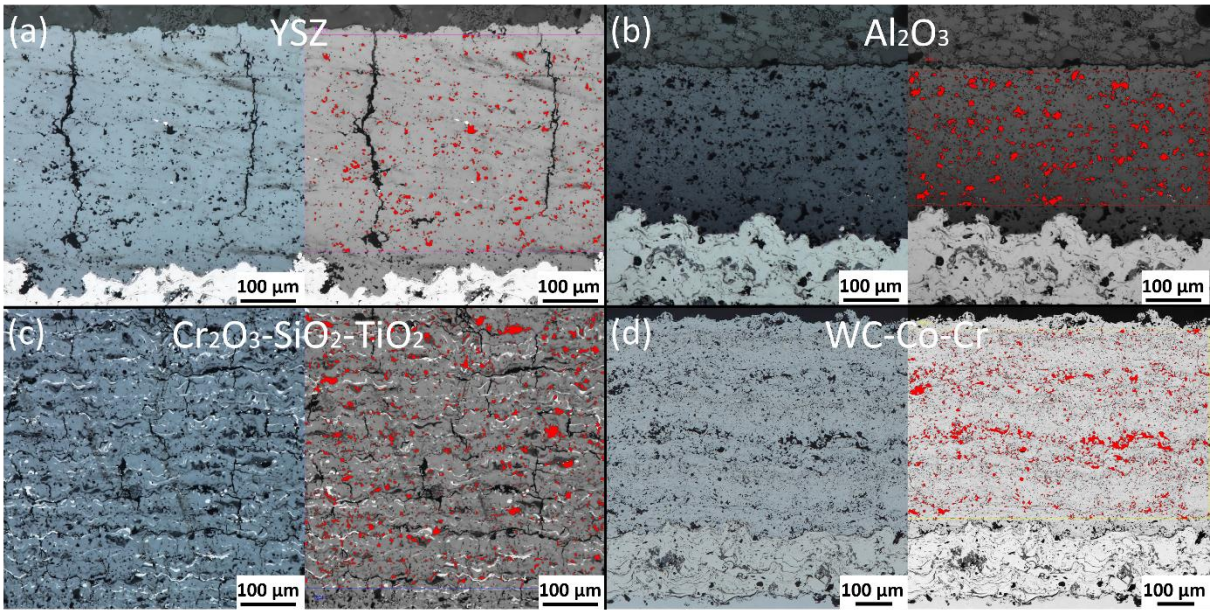

Figure 23 Cross-sections of (a) YSZ, (b) Al_2O_3, (c) Cr_2O_3-SiO_2-TiO_2 and (d) WC-Co-Cr coatings; pores are marked by red color

Table 6 Rietveld refinement and porosity measurements of YSZ, Al_2O_3, Cr_2O_3-SiO_2-TiO_2 and WC-Co-Cr plasma sprayed coatings

Coating	Phases [wt. %]	Porosity [%]
YSZ	t`-YSZ	3.1
Al_2O_3	η-Al_2O_3 – 94% α-Al_2O_3 – 6%	6.9
Cr_2O_3-SiO_2-TiO_2	Cr_2O_3 – 91 % Cr – 7 % SiO_2 – 2 %	6.8
WC-Co-Cr	W_2C – 43 % WC – 18 % WO_2 – 2 % CoO – 22 % CrN – 15 %	5.6

5.1.2 Surface topography

Analysis of surface topography was performed on ceramic and cermet coatings in the as-sprayed state, after grinding with #220 abrasive paper and after polishing with diamond suspensions containing 9, 3 and 1 µm abrasive particles. The results are shown in Table 7.

The values of the surface arithmetic mean height *Sa*, the root mean square *Sq*, the skewness *Ssk* and the surface roughness factor *Rs* decreased gradually from the as-sprayed state down to the polished state. On the contrary, the values of the kurtosis *Sku* increased. The decrease of the surface arithmetic mean height *Sa*, the root mean square *Sq* and the surface roughness factor *Rs* was connected to the removal of peaks and the progressive flattening of the surface during the grinding/polishing process. The decrease in the skewness *Ssk* values shows that the surface predominantly consisted of deep valleys/pores as the grinding/polishing process mostly affecting the peaks rather than the valleys. The gradual increase in the kurtosis *Sku* can be explained by the use of finer abrasive particles with each subsequent step of surface treatment (from grinding with #220 abrasive paper down to polishing with 1 µm diamond suspension).

Table 7 Roughness parameters of as-sprayed, ground and polished surfaces of YSZ, Al_2O_3, Cr_2O_3-SiO_2-TiO_2 and WC-Co-Cr coatings

Coating	Surface condition	Sa [µm]	Sq [µm]	Ssk [-]	Sku [-]	Rs [-]
YSZ	As-sprayed	9.1	11.6	0.12	3.11	1.25
	#220	1.0	1.9	-1.04	3.30	1.01
	9 µm	0.3	1.0	-1.32	10.01	1.01
	3 µm	0.2	0.8	-1.43	10.21	<1.01
	1 µm	0.2	0.7	-1.34	12.32	<1.01
Al_2O_3	As-sprayed	8.8	10.9	0.22	2.90	1.10
	#220	0.9	1.2	-0.90	3.53	1.01
	9 µm	0.6	0.8	-1.22	4.54	1.01
	3 µm	0.3	0.4	-1.84	8.10	<1.01
	1 µm	0.2	0.3	-2.01	9.92	<1.01
Cr_2O_3-SiO_2-TiO_2	As-sprayed	9.1	11.4	0.20	2.80	1.20
	#220	0.7	0.8	-0.64	3.63	1.01
	9 µm	0.3	0.4	-0.72	7.81	1.01
	3 µm	0.1	0.2	-0.91	9.92	<1.01
	1 µm	0.1	0.1	-1.03	10.54	<1.01
WC-Co-Cr	As-sprayed	9.3	11.6	0.34	2.90	1.21
	#220	1.0	1.3	-1.22	4.44	1.01
	9 µm	0.2	0.3	-1.40	4.83	1.01
	3 µm	0.1	0.2	-1.73	12.54	<1.01
	1 µm	0.1	0.1	-1.80	15.50	<1.01

5.1.3 Wetting behavior

All YSZ, Al_2O_3, Cr_2O_3-SiO_2-TiO_2 and WC-Co-Cr plasma sprayed coatings revealed hydrophilic behavior in the as-sprayed, ground and polished surface states with a water contact angle (WCA) below 90°, see Table 8. The wetting behavior of ceramic coatings in the as-sprayed and polished states was found to be similar. The most significant difference in WCA between different surface states, as well as the highest WCA value, was observed for the cermet WC-Co-Cr coating, namely from ~89° in the as-sprayed state down to ~55° after grinding and up to ~73° in the polished state.

Table 8 WCA measurements of as-sprayed, ground and polished surfaces of YSZ, Al_2O_3, Cr_2O_3-SiO_2-TiO_2 and WC-Co-Cr coatings

Coating	Surface condition	WCA [°]	WCA after 300 sec [°]
YSZ	As-sprayed	71 ± 2	64 ± 3
	#220	69 ± 1	61 ± 3
	9 µm	66 ± 3	60 ± 2
	3 µm	68 ± 3	62 ± 3
	1 µm	70 ± 1	59 ± 1
Al_2O_3	As-sprayed	79 ± 3	66 ± 2
	#220	72 ± 3	63 ± 3
	9 µm	63 ± 3	57 ± 2
	3 µm	61 ± 1	55 ± 3
	1 µm	81 ± 1	57 ± 1
Cr_2O_3-SiO_2-TiO_2	As-sprayed	83 ± 2	60 ± 3
	#220	69 ± 3	55 ± 2
	9 µm	72 ± 2	57 ± 2
	3 µm	88 ± 4	50 ± 3
	1 µm	87 ± 4	53 ± 1
WC-Co-Cr	As-sprayed	89 ± 1	79 ± 4
	#220	55 ± 2	50 ± 2
	9 µm	59 ± 2	51 ± 2
	3 µm	62 ± 1	49 ± 3
	1 µm	73 ± 3	53 ± 1

It was observed that the WCA values continued decreasing over time. Therefore, all measurements of the WCA were prolonged for 300 seconds until the WCA value became stable and remained unchanged. All the coatings showed similar WCA values ranging from ~50° up to ~79° after 300 s of measurements in the as-sprayed, ground and polished states. The effect of water absorption on plasma sprayed oxide ceramic coatings in the polished state was observed by Harju et al. [86], where the WCA value of the polished (Ra = 0.26 µm) Al_2O_3 coating decreased from ~73° down to ~50° during the first 360 seconds of water droplet exposure. A similar result on the decrease in the WCA value was observed in the current work. The WCA value of the polished (Sa ~ 0.2 µm) Al_2O_3 coating changed from ~81° down to ~57°

after the first 300 seconds of water droplet exposure. Such a significant decrease of the WCA values was also observed in all the studied coatings and was presumed to be connected with the coatings open porosity which is typical for plasma sprayed coatings [50]. The smallest change in the WCA value with the time was noticed on the YSZ ceramic coating. Though, the porosity of the YSZ coating was the lowest among all the studied coatings, see Table 6, the decrease of the WCA value over the time was connected to the presence of vertical cracks, see Figure 23a. The crucial effect of cracks on wetting behavior was reported by Han et al. [87], where the cracks-free styrene-based memory shape polymer (S-SMP) showed almost hydrophobic behavior with the WCA of ~85°. Whereas, the introduction of cracks into S-SMP led to the hydrophilic state with dramatical decrease of the WCA down to ~25°. On the basis of the fact that cracks changed wetting behavior from almost hydrophobic to hydrophilic state, it can be suggested that vertical cracks in the YSZ coating provided faster infiltration of water droplets into the coating rather than to the pores. Therefore, the WCA value of the YSZ coating did not change significantly after 300 seconds.

The effect of coatings porosity/cracks on wetting behavior among all the coatings was dominant compared to the surface topography state. Therefore, no clear evidence of the surface topography influence on wetting behavior was observed at the end.

According to the Wenzel model of wetting, the surface roughness factor *Rs* amplifies wetting behavior, i.e. a hydrophilic surface becomes more hydrophilic, and a hydrophobic surface becomes more hydrophobic. The studied coatings were mostly ceramics that are polar components and supposed to be hydrophilic due to the strong polar-polar interactions [22]. However, the highest value of WCA (more hydrophobic), as well as the highest surface roughness factor *Rs*, was observed for the as-sprayed surfaces. It shows that wetting did not follow the Wenzel model, but followed the Cassie-Baxter model (Eq. 7) at the moment of first contact of the water droplet with the solid surface. The Cassie-Baxter model of wetting considers the existence of air pockets between the solid and liquid phase, Eq. 7 and Figure 3. These air pockets prevent contact of the liquid phase with the solid phase, thus providing a higher water contact angle value. Subsequently, the water droplet filled the coating pores over time, resulting in a lower water contact angle value. Once the water droplet filled the pores, the wetting state changed from the Cassie-Baxter to the Wenzel wetting state, Eq. 6 and Figure 3.

Consequently, it can be suggested that the WCA value of intrinsically hydrophilic materials might be increased (toward hydrophobicity) if the Cassie-Baxter wetting state is reached and the penetration of water into the pores/valleys/cracks is prevented. Achievement of the long-

term stable Cassie-Baxter wetting state is possible when the surface roughness has the multi-scale character, with nano- and/or submicron-sized peaks/valleys [21].

Based on the results obtained from this study, further research is focused on the formation of YSZ and WC-Co-Cr coatings with a multi-scale topography, with the aim of trying to amplify coatings hydrophobicity. In order to ensure the formation of the multi-scale surface roughness, it was decided to introduce ultra-fine powder particles into the initial feedstock. To realize that, (i) YSZ coatings were produced by the means of suspension plasma spraying (SPS), utilizing ultra-fine powder particles; and (ii) bi-modal (combination of the coarse and ultra-fine powder particles) feedstock was used in the case of WC-Co-Cr material to fabricate the coatings by the use of high-velocity oxy-fuel (HVOF) spraying. The HVOF technology enables the formation of coatings with a lower porosity in comparison to atmospheric plasma spraying, but the heat input in HVOF is not enough to fabricate the coatings from YSZ powder feedstock, therefore the HVOF was only used for the spraying of WC-Co-Cr.

5.2 Investigation of wettability of YSZ plasma sprayed coatings with different microstructure

Yttria-stabilized zirconia (YSZ) material was used in the form of solid and liquid feedstocks to manufacture coatings with different microstructures, namely lamellar and columnar, and to investigate the effect of surface topography and microstructure on wetting behavior. The conventional route of spraying of YSZ powder was used to fabricate the coating with a lamellar microstructure (sample F4 YSZ), using atmospheric plasma spraying utilizing the F4 plasma torch. An in-house-made ethanol-based suspension with YSZ ultra-fine powder particles was used to develop YSZ coatings with the columnar microstructure (samples WSP-H YSZ, A3-D YSZ and A3-P YSZ), employing the water-stabilized WSP-H and Axial III plasma torches.

5.2.1 Microstructure and surface chemistry

Cross-sectional images of plasma sprayed YSZ coatings with lamellar and columnar microstructure are presented in Figure 25. It is clearly seen that the F4 YSZ and WSP-H YSZ coatings were significantly different. The F4 YSZ sample consisted of a conventional lamellar microstructure with a low number of unmelted particles and a relatively low porosity (~3%), see Figure 24 and Figure 25a-b. Such a lamellar microstructure is typical for the powder feedstock plasma spraying process [50]. The overlapping lamellae (splats) were ~40 μm in size and larger, corresponding to the size of the feedstock powder particles (~20-70 μm). The overlapping of the splats is apparent in Figure 25b.

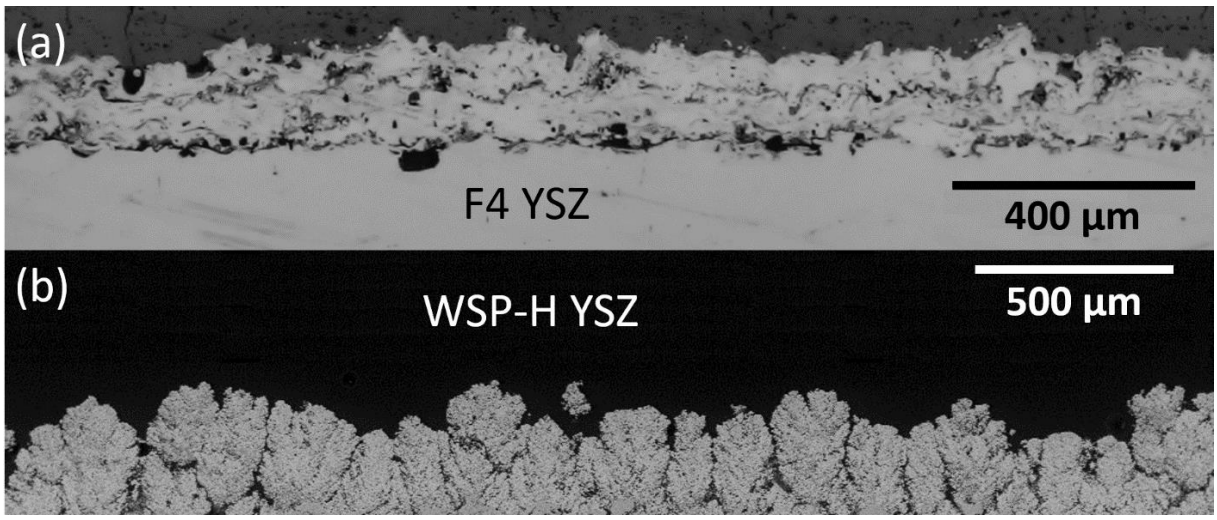

Figure 24 Cross-section micrographs of YSZ (a) lamellar and (b) columnar microstructures

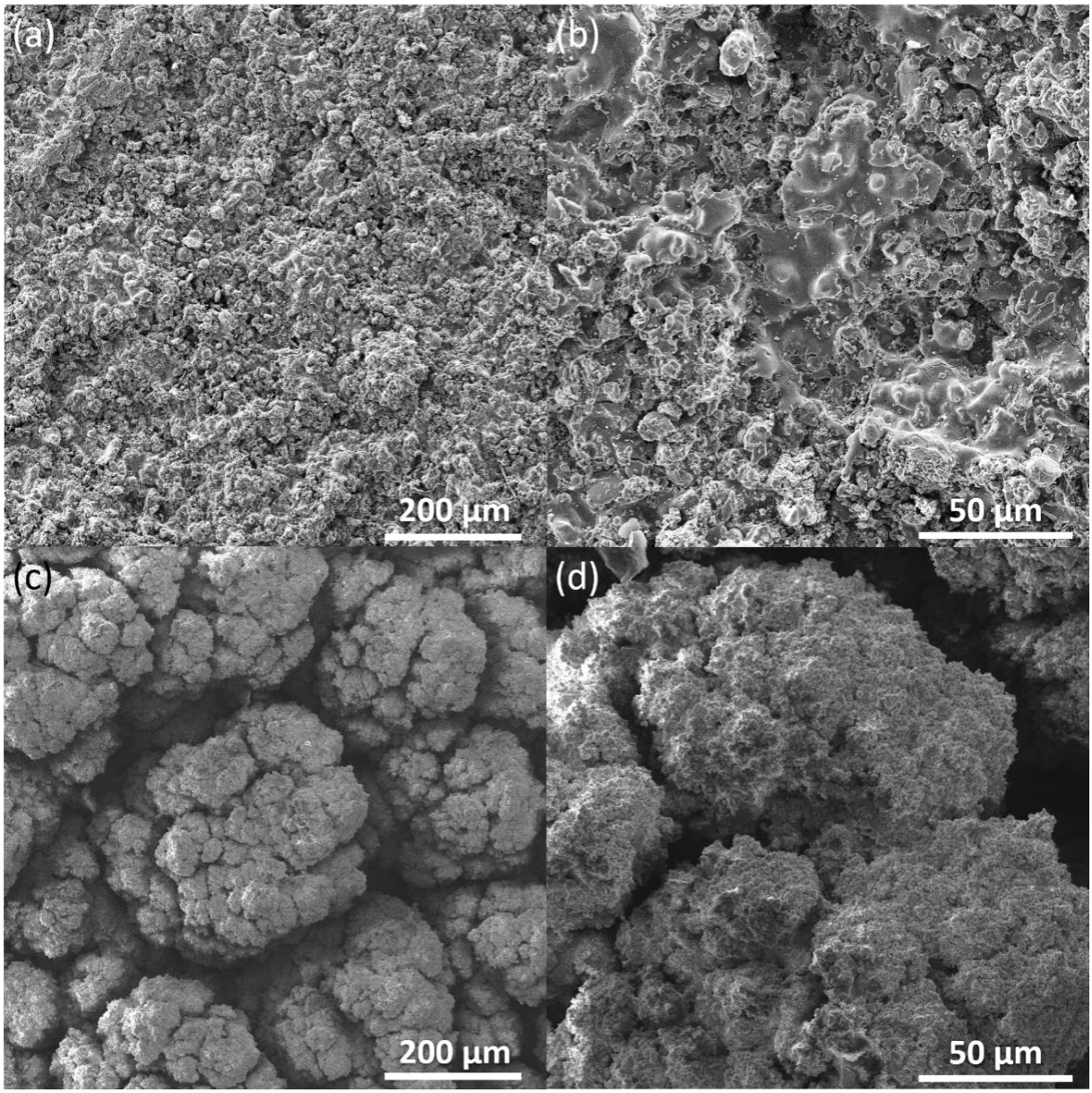

Figure 25 Top-view of YSZ (a, b) lamellar and (c, d) columnar plasma sprayed coatings

On the other hand, the WSP-H YSZ sample consisted of a columnar or cauliflower-like microstructure, with clearly distinguishable columns separated by inter-columnar voids, see Figure 24 and Figure 25c-d.

During the plasma spraying of suspensions, the suspension with nano- and submicron-sized (~50-500 nm) powder particles entered the plasma jet and formed agglomerates. Furtherly, if the agglomerates were coarse and heavy enough, they followed the flow of plasma gases, impacting the substrate. If the agglomerates were too small and light, they flew on the periphery of the plasma stream. This resulted in the formation of massive columns by coarser splats while finer splats were attached at the top of the columns [88, 89]. Figure 25c-d shows that massive columns (~50-200 μm in size) are covered by submicron-sized particles creating a multi-scale surface topography.

Two sets of coatings, namely A3-D and A3-P, were sprayed employing an Axial III plasma torch using the same spraying parameters, but different trajectories of the spraying program, see Figure 26. The trajectory for the A3-D YSZ sample was shorter, as well as the cooling time of the sample during spraying, in comparison to the sample A3-P YSZ.

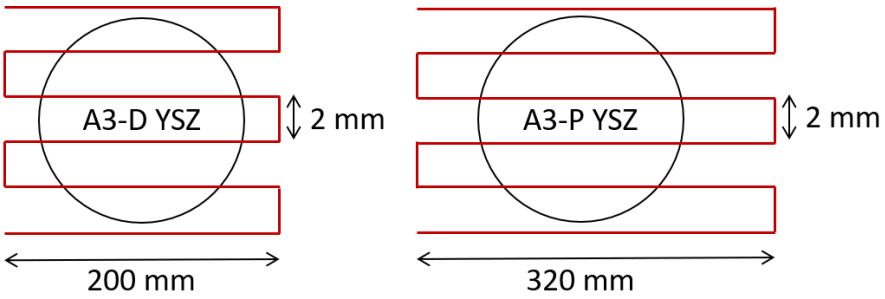

Figure 26 Schematic illustration of the manipulator movement trajectory during spraying of A3-D and A3-P YSZ coupon samples

The difference in spray trajectory was found to have only a slight effect on the appearance of the columnar microstructure of the YSZ coatings, as shown in Figure 27. Cross-sectional observation of Axial III suspension plasma sprayed YSZ coatings revealed that the A3-P YSZ sample consisted of a columnar microstructure with clearly separated columns. In contrast, the A3-D YSZ sample was of a denser columnar microstructure, with a lower number of gaps/pores between columns. However, the presence of inter-columnar voids at the surface of A3-D/A3-P YSZ samples was not observed when compared to the sample WSP-H YSZ.

The denser microstructure of the A3-D YSZ sample was formed due to the shorter trajectory of the manipulators movement during spraying followed by the shorter cooling time

and, therefore, different sintering conditions. However, the top view of the A3-D YSZ and A3-P YSZ samples, presented in Figure 31, did not show a significant difference. In a similar way to the WSP-H YSZ coating, the surface topography of the A3-D and A3-P YSZ samples consisted of a multi-scale topography with massive coarse columns (~30-200 μm in size) covered by submicron-sized particles, see Figure 28.

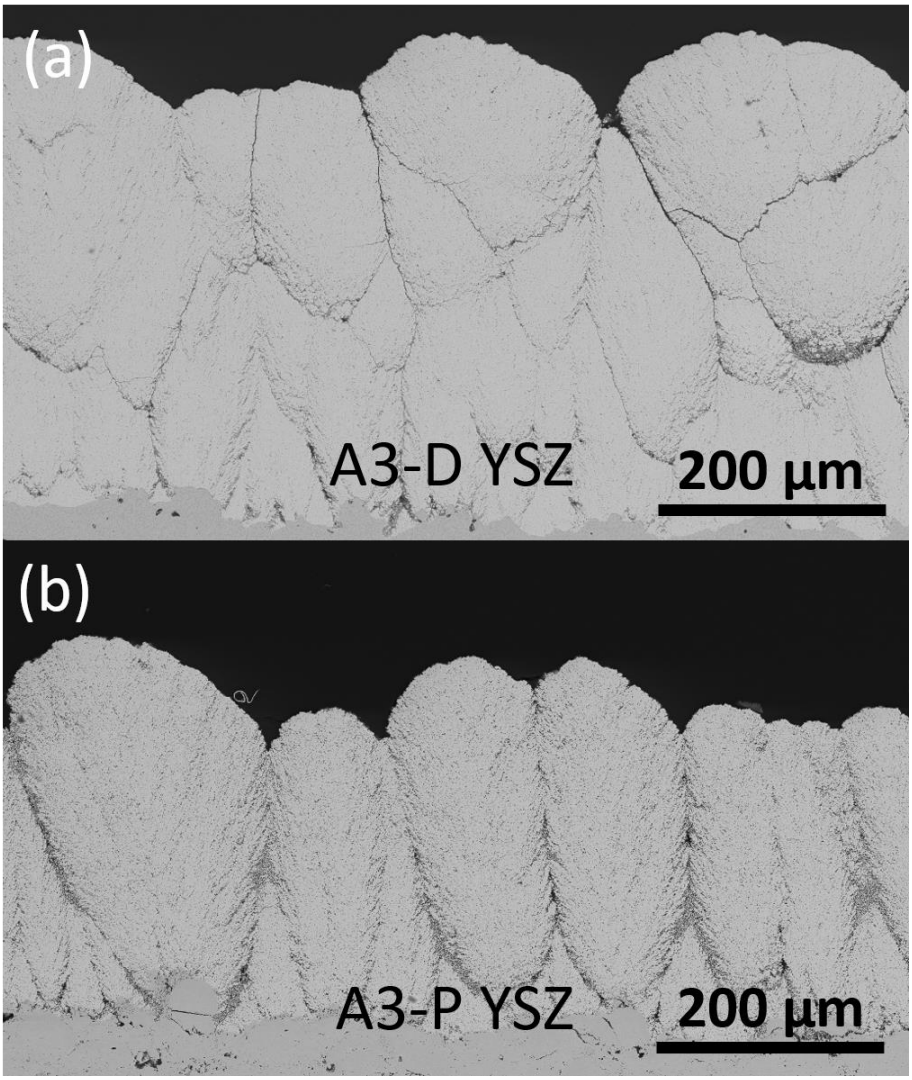

Figure 27 Cross-section micrographs of (a) A3-D and (b) A3-P YSZ coatings fabricated by Axial III plasma torch

The analysis of XRD patterns revealed that all the coatings consisted of the metastable tetragonal phase (t` - YSZ), shown in Figure 29. During the plasma spraying process, suspension or powder particles were heated up to extremely high temperatures with a subsequent intensive solidification when impacting the solid substrate. The single metastable tetragonal YSZ phase formation could be expected under such non-equilibrium conditions [90].

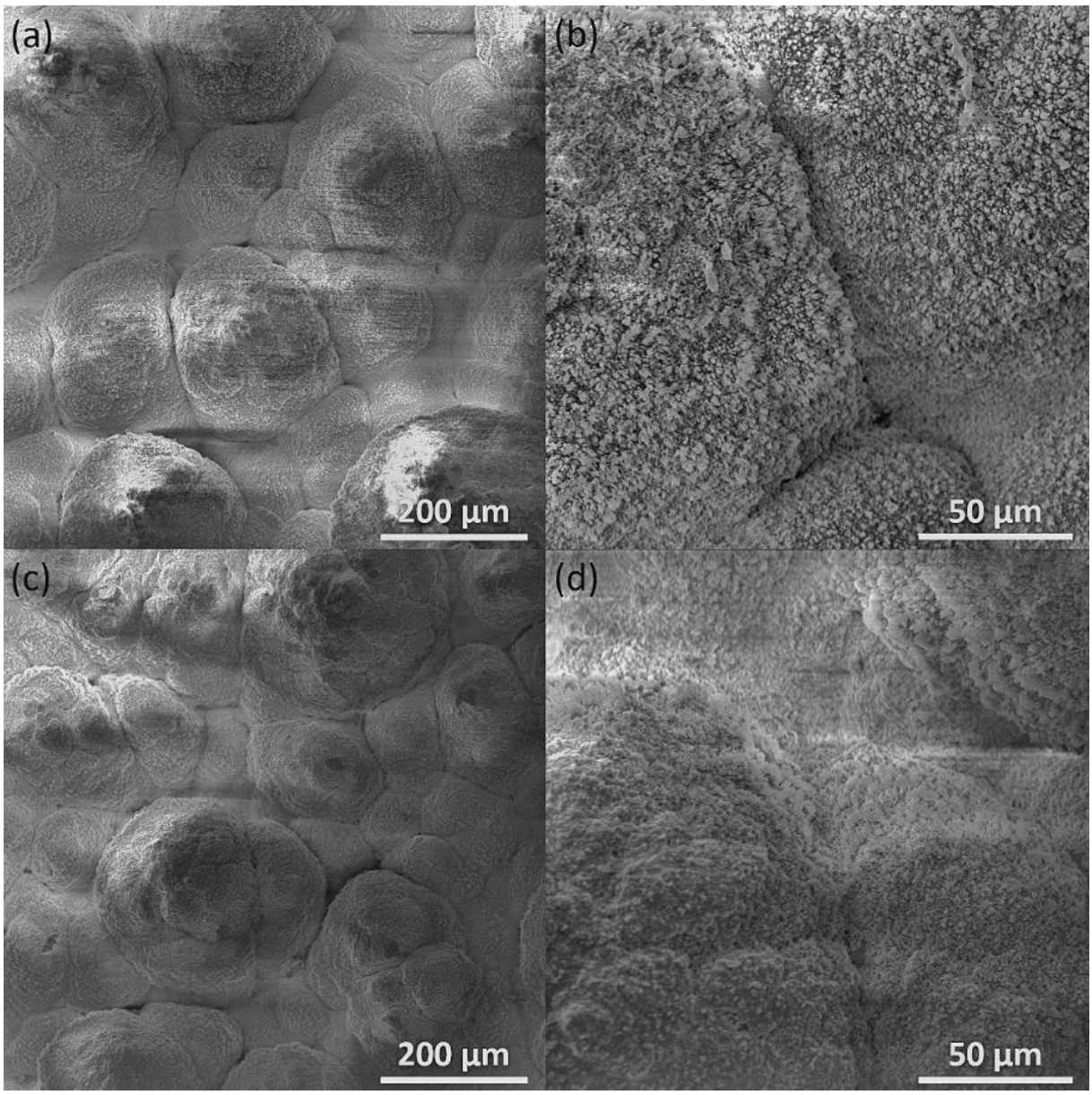

Figure 28 Top-view of (a, b) A3-D and (c, d) A3-P YSZ coatings fabricated by Axial III plasma torch

Energy-dispersive X-ray spectroscopy (EDX) analysis was performed in order to compare the elemental distribution of F4 YSZ, WSP-H, A3-D and A3-P YSZ coatings. The results are summarized in Table 9. The EDX analysis showed the presence of zirconium, oxygen and yttrium elements, following the chemical composition of YSZ (ZrO_2-Y_2O_3) initial powder/suspension feedstock. The distribution of elements was found to be very similar for all the YSZ coatings: 59-61 wt.% of zirconium, 14-15 wt.% of yttrium and 24-26 wt.% of oxygen, which was also found in a good agreement with the relevant literature [89].

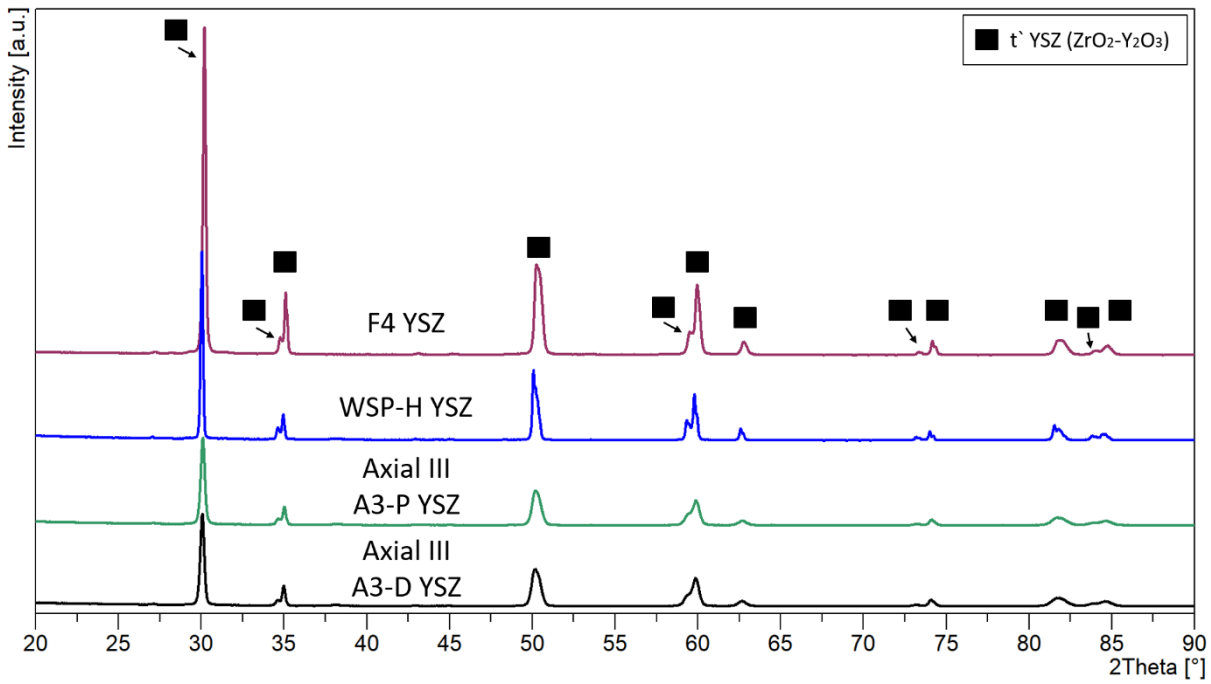

Figure 29 X-ray diffraction analysis of lamellar (F4 YSZ) and columnar (WSP-H YSZ, A3-P YSZ, A3-D YSZ) coatings

Table 9 EDX analysis of YSZ coatings

Coating	Element [wt.%]		
	Zr	Y	O
F4 YSZ	59.9	14.1	26.0
WSP-H YSZ	60.1	14.1	25.8
A3-D YSZ	59.2	15.3	25.5
A3-P YSZ	59.9	15.2	24.9

The results of quantitative X-ray photoelectron spectroscopy (XPS) analysis are summarized in Table 10. Even though different APS and WSP-H technologies were used to produce the YSZ coatings, the results of the XPS analysis showed no significant difference among the samples. The XPS analysis revealed the highest content of Zr 3d (69-70 at.%), then O 1s (~17 at.%) and Y 3d (4-5 at.%), which is the base of YSZ (ZrO_2-Y_2O_3). The C 1s element was detected due to the organic contaminations adsorbed from the atmosphere and/or the vacuum chamber of XPS apparatus [91].

Table 10 XPS quantitative analysis of YSZ coatings

Coating	Element [at.%]			
	Zr 3d	Y 3d	O 1s	C 1s
F4 YSZ	69.1	4.9	17.8	8.2
WSP-H YSZ	70.1	4.7	17.3	7.9
A3-D YSZ	69.6	4.7	17.4	8.3
A3-P YSZ	69.8	5.0	17.1	8.1

5.2.2 Surface topography

The surface topography was analyzed on the as-sprayed lamellar (F4 YSZ) and columnar (WSP-H YSZ, A3-D YSZ and A3-P YSZ) coatings. In this section, the surface topography taken from the area of 648×648 μm^2 is presented, thus the presented data for the F4 YSZ sample (Table 11 and Table 7) was found to be slightly different.

The results are summarized in Table 11 and presented in Figure 30 as 3D illustrations of the coatings' surface. The values of the surface arithmetic mean height (*Sa*), the root mean square height (*Sq*) and the surface roughness factor (*Rs*) were significantly higher for the YSZ samples with a columnar microstructure. The YSZ samples with a columnar microstructure showed a higher number of pores/valleys than peaks (*Ssk* < 0). On the contrary, the surface of the lamellar YSZ sample revealed a higher number of peaks (*Ssk* > 0). The slight difference in kurtosis (*Sku*) showed that the peaks on the surface of the columnar WSP-H YSZ sample were sharper (*Sku* > 3) than the peaks on the surface of the F4 YSZ, A3-D and A3-P samples (*Sku* ~ 3).

Table 11 Roughness parameters of surfaces of YSZ coatings

Coating	Sa [µm]	Sq [µm]	Ssk [-]	Sku [-]	Rs [-]
F4 YSZ	7.3	9.1	0.14	2.81	1.29
WSP-H YSZ	41.8	52.4	-0.93	3.45	3.56
A3-D YSZ	28.3	34.0	-0.05	2.31	2.56
A3-P YSZ	30.1	35.9	-0.21	2.35	2.65

Finally, the surface roughness factor *Rs* was almost three times higher for the WSP-H YSZ sample (columnar microstructure) compared to the F4 YSZ sample (lamellar microstructure) and of ~30% higher than that of the A3-D/A3-P YSZ samples (columnar microstructure). This

difference in *Rs* values between the F4 YSZ and WSP-H/A3-D/A3-P YSZ samples is connected to the use of ultra-fine powder in the suspension feedstock. The ultra-fine particles from the initial feedstock enabled the formation of submicron-sized peaks on the surface, enlarging the total surface area of the coating. When comparing Figure 25b (F4 YSZ), Figure 25d (WSP-H YSZ) and Figure 28b, d (A3-D/A3-P YSZ), it is apparent that the surface of the lamellar YSZ sample was composed of flattened splats of several tens of microns in size, while the surface of the columnar YSZ samples was composed mostly of massive columns (~30-200 µm in size), covered by the submicron-sized particles. However, both the A3-D and A3-P YSZ samples were much smoother in comparison to the WSP-H YSZ sample. The higher value of the surface roughness factor *Rs* of the WSP-H YSZ sample is connected to the presence of a higher number of ultra-fine features located at the top of the massive columns. As can be seen from the 3D illustrations in Figure 30, the surface of large columns is rougher in the case of the WSP-H YSZ sample. The same tendency can be observed when comparing top-views of the WSP-H YSZ with A3-D/A3-P YSZ samples, Figure 25c and Figure 28a, c, respectively. This resulted in a higher value of kurtosis *Sku* and a lower value of skewness *Ssk* and meant that the surface of the WSP-H YSZ sample consisted of a higher number of narrow valleys/pores presented on the surface in comparison to the A3-D and A3-P YSZ surfaces.

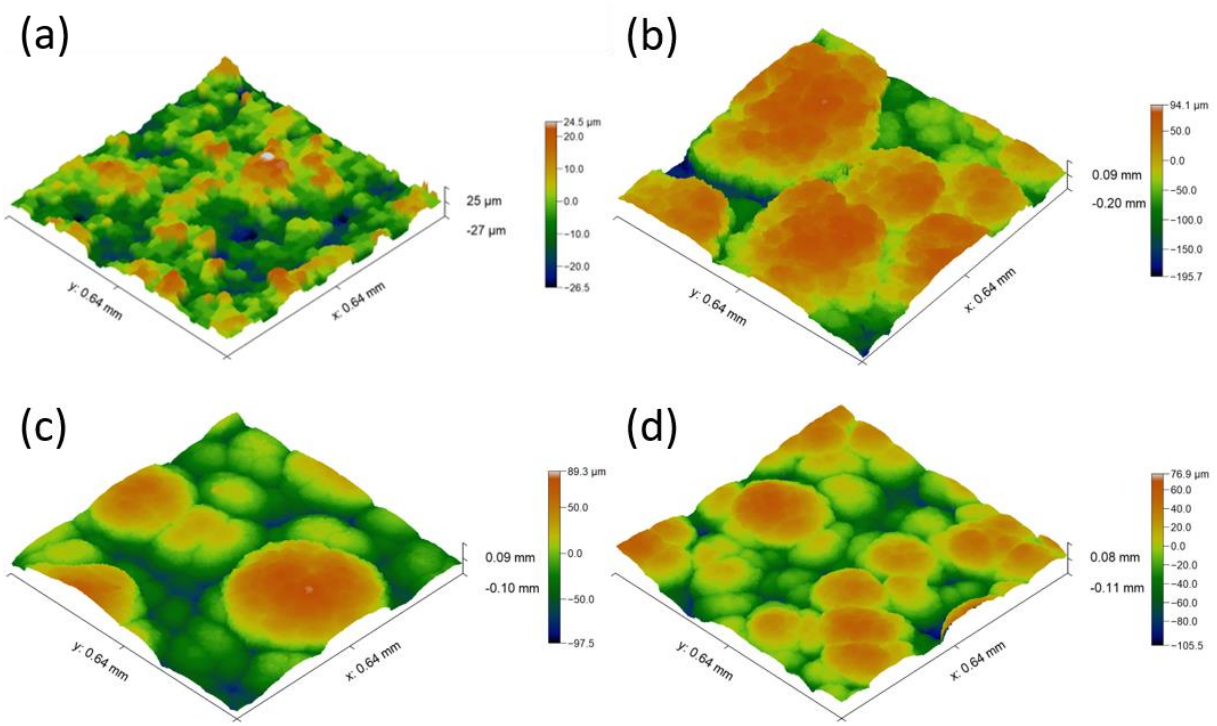

Figure 30 3D topography illustration of (a) F4, (b) WSP-H, (c) A3-D and (d) A3-P YSZ coatings

5.2.3 Wetting behavior

The results of the water contact angle (WCA) measurements pointed to a significant difference in wetting behavior among all studied coatings. The lamellar F4 YSZ sample was found to be hydrophilic with a WCA of 64 ± 3° and the columnar WSP-H YSZ sample was superhydrophobic with a WCA of 156 ± 3°, Figure 31. The YSZ coatings with columnar microstructure fabricated employing an Axial III plasma torch showed hydrophobic behavior in the A3-D YSZ sample (with WCA of 129 ± 3°) and almost superhydrophilic behavior in the A3-P YSZ sample (with WCA of 14 ± 7°), Figure 34.

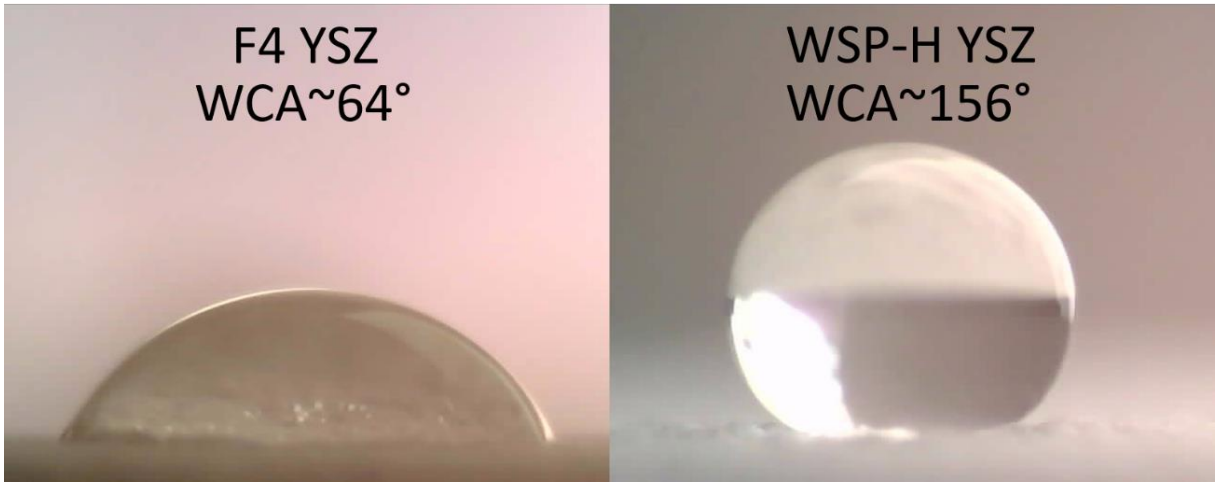

Figure 31 Water droplet behavior on the as-sprayed lamellar F4 YSZ and columnar WSP-H YSZ coatings

The wetting behavior of solid surfaces depends mostly on two main factors, namely the surface chemistry and surface topography. In recent studies, C-H hydrocarbon surface contamination was shown to be responsible for the different wetting behavior of REO's ceramic coatings with a columnar microstructure [91], where, without any change in microstructure/surface topography, an increase of adventitious carbon from 8.6% up to 32.4% was claimed to be responsible for "superhydrophilic-to-superhydrophobic" transition. Qiao et al. [71] reported on the hydrophobic effect of carbon accumulated on the surface of WC-Co-Cr HVOF sprayed coatings after laser texturing. In their work, the content of carbon increased from ~11 wt.% up to ~63 wt.% according to EDX analysis. However, in the present study, the content of carbon (C 1s) detected by the XPS analysis was found to be almost the same, ranging from 7.9 to 8.3 at.%, and no carbon was detected by the EDX analysis for any YSZ coating, see Table 9 and Table 10. As the XRD analysis of the YSZ coatings showed the same phase composition with only a single tetragonal-YSZ phase, the elemental distribution (the EDX and

the XPS analyzes) was found to be very similar, therefore, such a high difference in wetting behavior was mostly related to the difference in microstructure and topography.

The surface of the lamellar F4 YSZ sample was composed of the splats of several tens of microns in size and pores/cracks in between of them, Figure 25a-b. This combination provided hydrophilic wetting behavior following the Wenzel wetting model (Eq. 6), with pores filled by water, resulting in the low WCA value (hydrophilicity). The opposite wetting behavior was found on the columnar WSP-H YSZ sample, where wetting followed the Cassie-Baxter model (Eq. 7) or a combination of the Wenzel and Cassie-Baxter models (Eq. 8). The Cassie-Baxter wetting model considers the presence of entrapped air-pockets between liquid and solid surfaces. Therefore, the superhydrophobicity of the columnar WSP-H YSZ sample was based on the multi-scale surface topography. The surface morphology of the columnar WSP-H YSZ sample consisted of coarse columns with the layer of submicron-sized peaks distributed at the top of the large columns, Figure 25c-d. The small air pockets could also be entrapped between the ultra-fine peaks and prevent the direct contact of water droplets with the solid surface. Thus, the water repellency was improved, resulting in superhydrophobic behavior. Even though ceramic coating's surface was supposed to be hydrophilic due to the strong polar-polar interactions with water [22], this result proved that using ultra-fine particles in the feedstock for thermal spraying might lead to the formation of the multi-scale topography with high water repellency.

The wetting behavior of the surfaces with the multi-scale topography can be described by a combination of the Wenzel and Cassie-Baxter models (Eq. 8). According to the combined model, the surface roughness factor *Rs* can amplify hydrophobicity, and thus it explained the difference in the wetting behavior of the WSP-H YSZ sample (*Rs* = 3.56) in comparison to A3-D/A3-P YSZ samples (*Rs* = 2.56/2.65). However, this did not explain the significant difference between A3-D and A3-P YSZ samples, which had a similar surface roughness. Such difference in the wetting behavior can be caused by the fact that the A3-P YSZ sample had many more pores between the columns in comparison to the A3-D YSZ sample, see Figure 27. The pores in the microstructure of the A3-P YSZ sample absorbed water droplets in a similar way as in the case of the F4 YSZ sample. In the case of the F4 YSZ and A3-P YSZ samples, the wetting behavior followed the Wenzel model, which assumes that intrinsically hydrophilic surfaces become more hydrophilic with increasing surface roughness factor *Rs*. Therefore, it explains the reason for the lower WCA value of the A3-P YSZ sample compared to the WCA value of the F4 YSZ sample (WCA = 14 ± 7° and *Rs* = 2.65 vs. WCA = 64 ± 3° and *Rs* = 1.29, respectively).

Figure 32 represents the height-maps of the A3-D, A3-P and WSP-H YSZ samples with the averaged arithmetical mean height *Ra* roughness parameter measured on 5 random places on the top of the columns. From Figure 24 and Figure 27, it is apparent that the microstructures of the WSP-H YSZ and A3-P YSZ coatings are relatively similar, but the WCA values are significantly different (156 ± 3° vs. 14 ± 7°). The difference in the wetting behavior was connected to the fact that the surface of the large columns of the WSP-H sample (*Ra* = 1.6 µm) was much rougher compared to the A3-P/A3-D YSZ samples (*Ra* = 0.6 µm). Some authors [92] observed a similar tendency on YSZ plasma sprayed coatings where coatings with higher roughness showed higher WCA values. The rough surface of the columns increased the total surface area of the WSP-H YSZ sample (WSP-H *Rs* = 3.56 vs. A3-P/A3-D *Rs* = 2.65/2.56), that ensured the Cassie-Baxter wetting state with entrapped air-pockets between solid and liquid phases, resulting in superhydrophobic behavior.

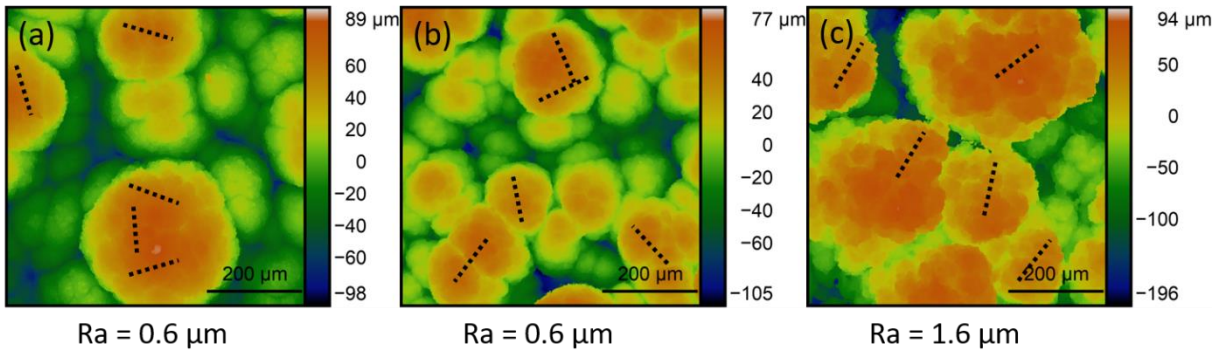

Figure 32 Height-maps of (a) A3-D, (b) A3-P and (c) WSP-H YSZ samples; the dashed lines (~100 µm) mark the profiles used for *Ra* measurements

Based on the discussion above, it can be concluded that (i) the lamellar microstructure of the YSZ (F4 YSZ sample) coatings provided hydrophilic behavior with the Wenzel wetting state due to the infiltration of water into pores and cracks in the coating; (ii) the presence of pores between flat columns supported almost superhydrophilic behavior with the Wenzel wetting state in the A3-P YSZ sample; (iii) similar flat columns, but with a denser columnar microstructure in the A3-D YSZ sample prevented the penetration of water into the coating, resulting in hydrophobic behavior with a Cassie-Baxter wetting state; and (iv) the rough surface of the columns as well as the high surface area of the WSP-H YSZ sample provided superhydrophobic behavior with a Cassie-Baxter wetting state.

As wetting behavior in the case of YSZ columnar microstructure samples appeared to be very sensitive to small changes in microstructure and surface topography, it was decided to apply the additional surface treatment in order to improve their hydrophobicity. The radio-

frequency (RF) plasma jet with hexamethyldisiloxane (HMDSO) admixture was used for this purpose. After such hydrophobization, the wetting behavior of the A3-D and A3-P YSZ samples turned from hydrophobic/hydrophilic up to the superhydrophobic state, i.e., from 129 ± 3° up to 150 ± 2° (for A3-D YSZ) and from 14 ± 7° up to 151 ± 1° (for A3-P YSZ). This transition is presented in Figure 33.

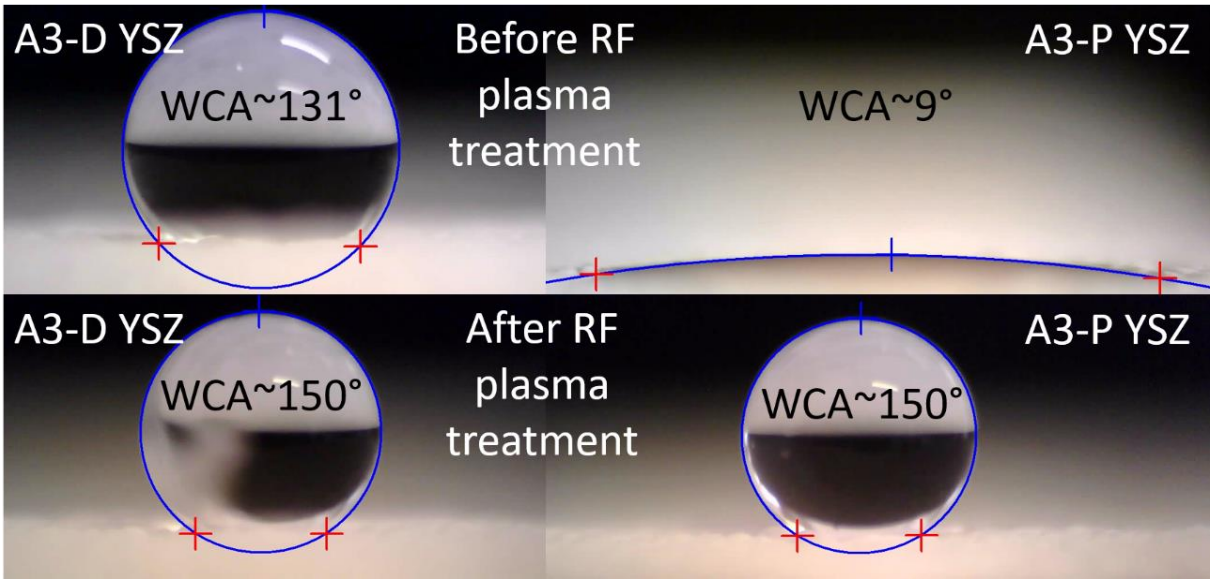

Figure 33 Water droplet behavior on A3-D and A3-P YSZ samples (top) before and (bottom) after RF plasma surface treatment

The EDX surface analysis of the modified A3-D and A3-P YSZ samples revealed a high concentration of carbon (~23 wt.%) and silicon (~16 wt.%). These two elements were addressed to the modification layer that was produced from the HMDSO admixture. The phenomenon of wettability transition is connected to the simultaneous modification of the surface chemistry ensured by the deposition of the nanostructured layer of hydrophobic organosilicons with multi-scale topography [75], Figure 34. The deposited layer was composed of irregular-shaped nano-sized particles (~100 nm in size) and their agglomerates (~1-2 μm in size) possessing dendritic morphology.

The RF plasma jet treatment did not significantly influence the roughness parameters of the A3-D and A3-P YSZ samples, see Table 11 and 12. A noticeable change was found in the values of the skewness *Ssk* parameter, from -0.05 down to -0.51 for the A3-D sample and from -0.21 down to -0.68 for the A3-P sample. The negative skewness means that the surface predominantly consists of valleys/pores than peaks, which is supposed to be due to the formation of a layer with porous dendritic structure composed of nano-sized particles and their micron-sized agglomerates. In the case of the A3-P YSZ sample, the RF plasma jet treatment

provided a fast transition of the wetting regime, i.e., from the homogeneous Wenzel regime to the heterogeneous Cassie-Baxter regime of wetting with a high water repellency (high hydrophobicity). The valleys/pores in the dendritic structure created a space for air-pockets to be entrapped, thereby resulting in enhanced superhydrophobic behavior.

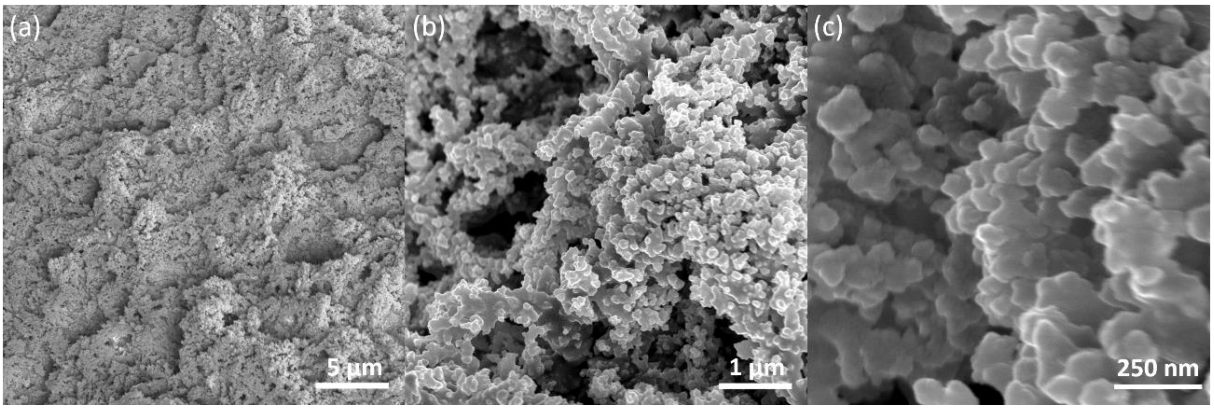

Figure 34 Top-view of RF-plasma modification layer at increasing magnification

Table 12 Roughness parameters of A3-D and A3-P YSZ coatings after RF plasma jet treatment

Coating	Sa [µm]	Sq [µm]	Ssk [-]	Sku [-]	Rs [-]
A3-D YSZ	28.5	34.1	-0.51	2.40	2.61
A3-P YSZ	30.3	36.0	-0.68	2.42	2.72

To estimate the robustness of the superhydrophobic behavior, the WSP-H YSZ, A3-D modified and A3-P modified samples were subjected to the water-flush test for ~5 min using tap water [24]. The superhydrophobic behavior of each YSZ sample was partially or completely degraded after this brief test, resulting in a loss of water mobility. For example, Figure 35 represents the A3-D YSZ modified sample after the water-flush test where water droplets attached to the damaged part.

Figure 35 Degradation of water-mobility performance of the A3-D YSZ modified sample after water-flush test

One of the potential applications of the YSZ coating with superhydrophobic behavior is in the anti-icing surfaces for airplanes and wind turbines where a high water contact angle and a relatively low density of YSZ (~ 2 g/cm^3) material would be beneficial. However, even though the superhydrophobic state was obtained, such a thin layer with dendritic structure composed from nano-particles was not expected to be wear-resistant or useful in sacrificial applications. Thus, further research focused on the production of wear-resistant coatings with multi-scale topography produced by the means of high-velocity oxy-fuel spraying.

5.3 Wetting behavior of WC-Co-Cr cermet coatings produced by high-velocity oxy-fuel spraying

The previous research discovered that the porosity of WC-Co-Cr thermal sprayed coatings had a significant impact on wetting behavior. Therefore, in order to lower porosity, and because of other advantages such as the higher hardness of coatings, higher efficiency and mobility, high-velocity oxy-fuel spraying (HVOF) technology was chosen. The WC-Co-Cr coatings were obtained from three different powders: (i) coarse powder (C16 sample), (ii) coarse powder with ultra-fine WC particles (CU16 sample) and (iii) fine powder with ultra-fine WC particles (CU31 sample). The main idea was to fabricate hard and wear-resistant coatings with a multi-scale surface topography, which could result in hydrophobic or superhydrophobic behavior. Additionally, Si-oil modification was applied (i) to isolate the surface roughness effect on wetting behavior and (ii) to amplify the hydrophobicity of the coatings. In this chapter, the role of surface chemistry and surface topography on wetting behavior and surface free energy of WC-Co-Cr coatings is analyzed and discussed in detail. This part of the thesis was published in the Journal of Thermal Spray Technology [93] and reproduced with permission from Springer Nature.

5.3.1 Microstructure and surface chemistry

The energy-dispersive X-ray spectroscopy analysis was performed on as-sprayed and as-sprayed modified WC-Co-Cr coatings. The result of EDX analysis of the as-sprayed samples is presented in Table 13. It revealed the presence of W, C, O, Co and Cr elements that were from the base material, while the analysis of the modified samples showed the presence of an additional Si element (~10 wt. %) that was supposed to be from Si-oil modification. As shown in Table 13, the distribution of elements was similar for all studied coatings and corresponded with existing literature [94].

Table 13 EDX analysis of C16, CU16 and CU31 coatings in the as-sprayed state

Coating	Element [wt. %]				
	W	C	O	Co	Cr
C16	79.6	11.6	3.1	5.5	0.2
CU16	80.1	10.8	3.4	4.8	0.9
CU31	78.3	12.3	4.6	4.5	0.3

A comparative XRD analysis of unmodified as-sprayed C16, CU16 and CU31 coatings is presented in Figure 36. Clear peaks of WC, W_2C and W phases were detected, while no peaks of Cr and Co binders were observed. The XRD patterns were similar for the C16 and CU16 coatings with nearly equal intensities of WC, W_2C and W phases, but distinctly different from the CU31 coating, as clearly seen from Rietveld refinement, Table 14. The highest decarburization of WC particles during spraying was observed in the CU31 coating, as shown by the highest amount of W_2C and W. Concurrently, the C16 coating showed the lowest decarburization with 51% of retained WC phase. Apparently, the decarburization process was related to the size of powder particles, as the finest powder feedstock was used in the fabrication of CU31 coating. It was reported elsewhere [95–97] that fine powder particles lead to higher decarburization. The in-flight temperature of the GP10CU-31 powder particles at a stand-off distance of 200 mm was the lowest among three powder feedstocks, Table 5 in section 4 Experimental design and methods. Taking this into account, it is believed that fine powder particles flew outside the flame core before reaching a 200 mm stand-off distance. Thus, these fine powder particles were cooled down more than the coarse ones at the moment of impact to the metallic substrate. Computational analysis carried out by Li et al. [98] supported these conclusions, as it was shown that the highest temperature at the moment of impact was obtained for powder particles 20 μm in size. The smaller (as well as larger) powder particles were predicted to reach lower temperatures, which was explained by the high susceptibility of small particles to fluctuations of the gas flow during HVOF spraying.

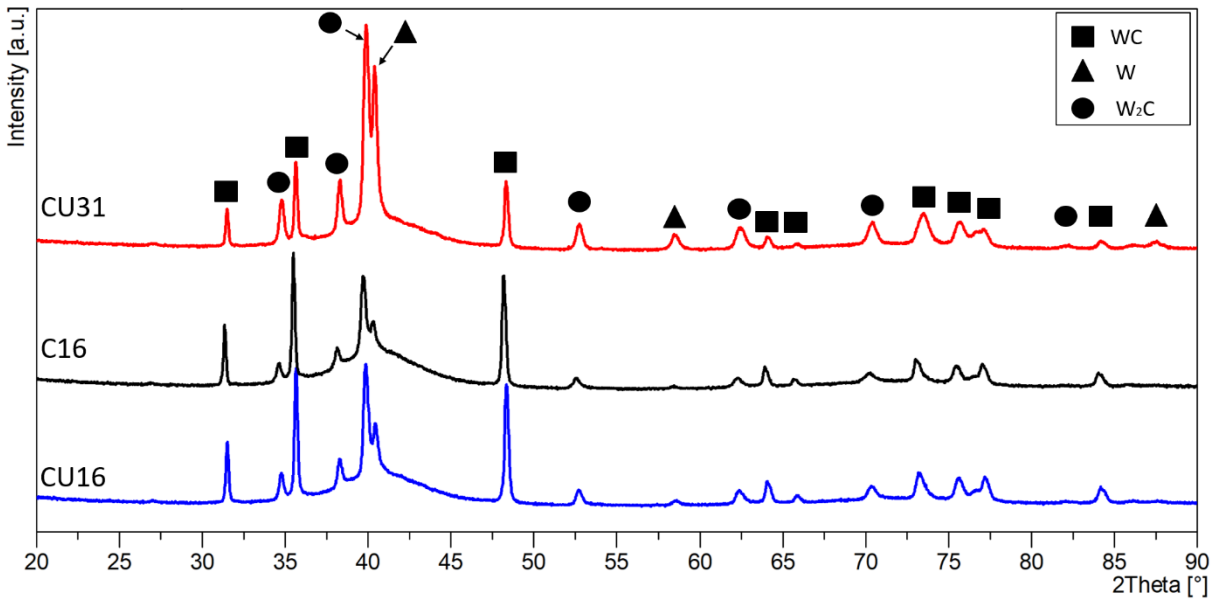

Figure 36 X-ray diffraction analysis of C16, CU16 and CU31 coatings in the as-sprayed state

In all the studied coatings, the presence of an XRD amorphous halo (from 34° to 45° 2θ values) indicated the content of nanocrystalline or amorphous phases. The amorphous halo was related to the Cr and Co metallic binders, agreeing with the existing literature [96, 97, 99–102]. The content of crystallinity was higher in coatings produced from finer powders, i.e., C16 coating (produced from coarse powder) showed 36%, whereas CU31 (produced from fine powder with ultra-fine WC particles) showed 50% of crystallinity, Table 14. These results could be explained by the measured in-flight temperature at the distance of 200 mm, which equals to the spraying distance, Table 5 in Section 4, that was measured to be ~2200° C for C16 coating and ~2020° C for CU31 coating. Thus, molten or partially molten powder particles were subjected to extensive cooling and solidification when impacting the substrate material with further formation of amorphous or nano-crystalline phase [96, 97, 99–102].

The XRD patterns of the modified as-sprayed C16, CU16 and CU31 coatings are not presented here as they did not reveal any presence of the Si-oil modification layer. This might be related to its very low thickness.

As wetting behavior is affected by the chemistry of the very surface layer, quantitative XPS analysis was performed on as-sprayed and polished unmodified surfaces, as well as on the modified polished surface of the C16, CU16 and CU31 coatings. The results of the quantitative XPS analysis of the as-sprayed and polished unmodified surfaces are presented in Table 15. Based on the detected peaks of W 4f, C 1s and O 1s, XPS analysis revealed that the surface chemistry of the cermet coatings was represented mainly through compositions of W, O and C. Clear peaks of Co 2p and Cr 2p were not detected and, thus, were not presented here.

Table 14 Crystalline phases and crystallinity content in C16, CU16 and CU31 as-sprayed coatings

Coating	Phase content [wt.%]			Crystallinity content [%]
	WC	W_2C	W	
C16	51	37	12	36
CU16	49	39	12	41
CU31	20	54	26	50

From Table 15, it is evident that the data of as-sprayed and polished unmodified coatings were different. Such a difference might be connected (i) to the influence of multi-scale roughness on the so-called "shadow effect" [103–105]; and (ii) to the formation of oxide/hydroxide and other layers during grinding/polishing, as within these processes freshly reactive surfaces were subjected to wear and direct contact with polishing slurries and/or cooling water. However, it is clearly seen that elemental distribution among the as-sprayed C16, CU16 and CU31 samples showed only a slight difference in the range of ± 2 at.%.

Table 15 XPS quantitative elemental analysis of as-sprayed and polished unmodified C16, CU16 and CU31 coatings

Coating	Element [at. %]		
	W 4f	C 1s	O 1s
C16 AS	26.4	49.7	23.9
CU16 AS	25.1	50.1	24.8
CU31 AS	23.1	50.9	26.0
C16 P	7.7	63.6	28.7
CU16 P	13.6	53	33.4
CU31 P	15.3	48.5	36.5

In the case of the polished unmodified samples, the distribution of elements differed significantly, Table 15. Thus, the deconvolution of all W 4f, C 1s and O 1s peaks was performed, as presented in Figure 37. The amount of W element in the studied coatings was significantly lower in comparison to the WC-Co-Cr HVOF coatings reported by Wesmann et al. [77, 78]. However, their coatings were subjected to the Ar-sputtering before XPS analysis, which decreased the number of oxides on the surface, as reported by Wesmann et al. [77, 78].

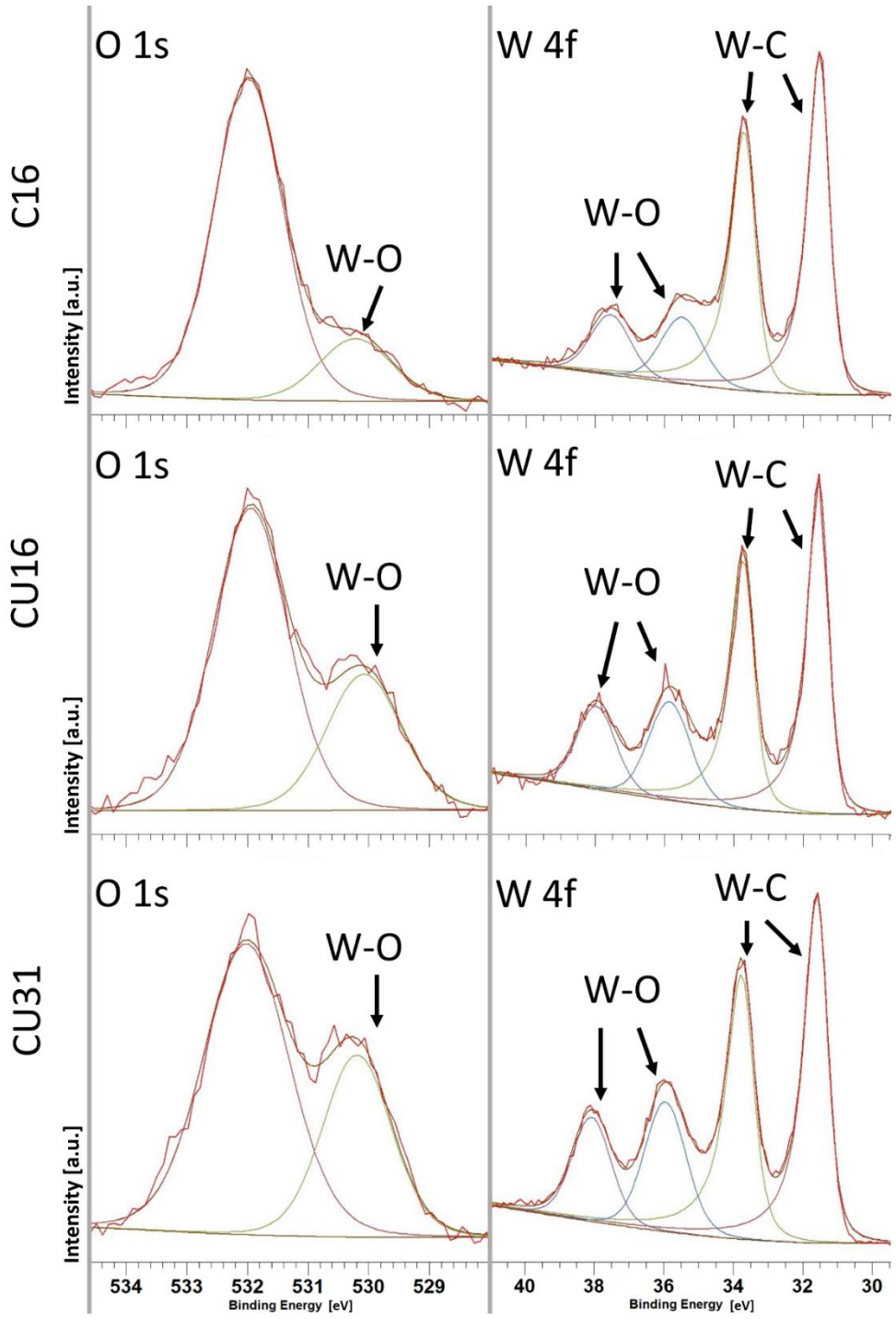

Figure 37 Deconvolution of O 1s and W 4f peaks from high-resolution XPS spectra of C16, CU16 and CU31 polished unmodified samples

The deconvolution of the W 4f and O 1s peaks showed a different content of W-O composition, see Figure 37. The central peak at ~532 eV of O 1s spectra was attributed to the C-O organic contamination from the surrounding atmosphere, whereas a smaller peak at ~530 eV of O 1s spectra was related to the Me-O compound showing W-O in the case of the studied coatings. The deconvolution of W 4f high-resolution spectra revealed two clearly distinguishable groups of peaks, namely (i) at ~31.5 and ~33.5 eV; and (ii) at ~36 and ~38 eV.

The first group was associated with the W-C compound, while the second was related to the W-O composition. In both, the O 1s and W 4f high-resolution spectra, the intensity of the peaks related to the W-O compound increased from the C16 sample to CU31 sample. When compared with XRD Rietveld refinement, Table 14, it is seen that the CU31 sample with the highest amount of W_2C and W phases showed the highest W-O content in XPS analysis as well. A similar outcome was reported by Zhang et al. [79] and it could be explained by the instability of W_2C and W in the air atmosphere, or after the grinding/polishing procedure with further formation of the tungsten oxide layer.

The deconvolution of C 1s high-resolution spectra, presented in Figure 38, revealed a very similar result with the central peak at ~283 eV addressed to the W-C composition. Only the CU31 sample had the second smaller peak at ~285 eV that was supposed to be related to the hydrocarbon C-H compound.

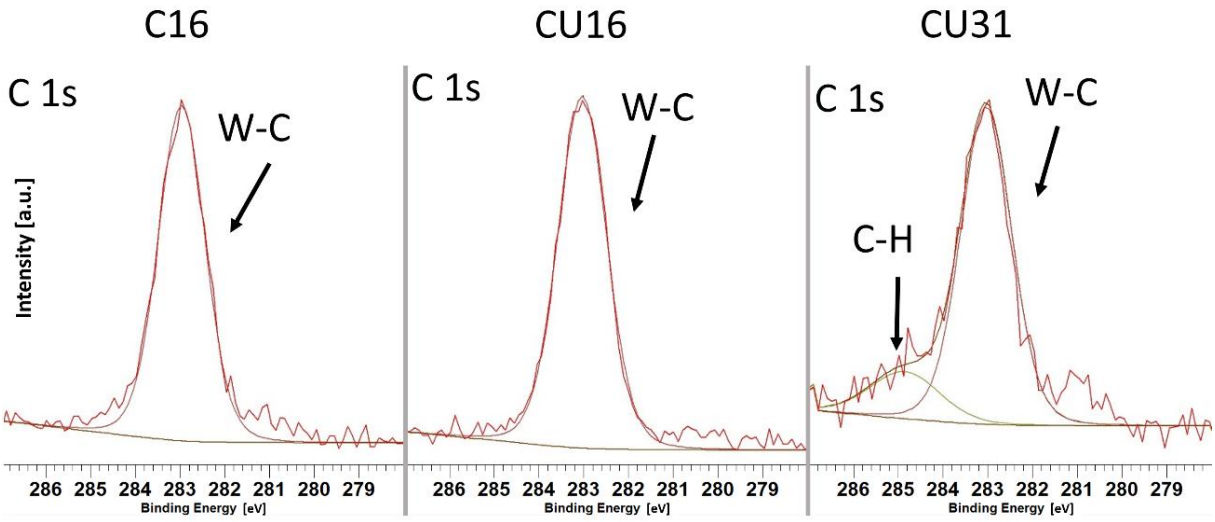

Figure 38 Deconvolution of C 1s peak from high-resolution XPS spectra of C16, CU16 and CU31 polished unmodified samples

Finally, XPS analysis of the polished modified C16, CU16 and CU31 samples showed the presence of Si 2p, C 1s and O 1s elements with nearly the same distribution, Table 18. All these three elements were from the polydimethylsiloxane that was the base of Si-oil. The presence of W 4f, Co 2p or Cr 2p was not detected, indicating that the thickness of the modification layer was enough to completely cover the base WC-Co-Cr coating.

Figure 39 represents cross-sections of the C16, CU16 and CU31 AS samples. All the coatings were of a lamellar or splat-like microstructure that is very common for HVOF deposits [96, 97, 99–101].

Table 16 XPS quantitative elemental analysis of polished modified C16, CU16 and CU31 coatings

Coating	Element [at. %]		
	Si 2p	C 1s	O 1s
C16 P-M	31.1	48.6	20.3
CU16 P-M	29.7	49.6	20.7
CU31 P-M	30.8	49.7	19.5

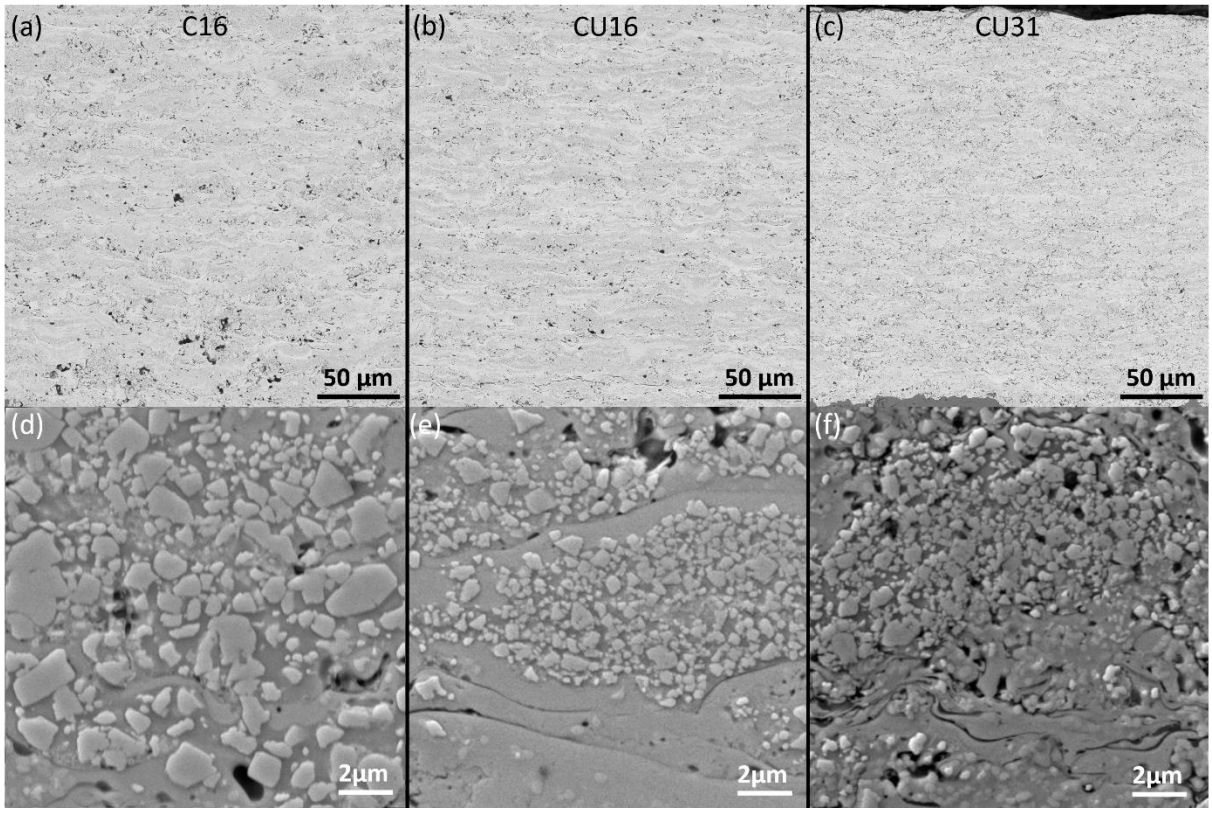

Figure 39 Cross-section micrographs and their details of (a, d) C16, (b, e) CU16 and (c, f) CU31 WC-Co-Cr samples

As one of the aims was to produce dense WC-Co-Cr coatings, the porosity of HVOF deposits was much lower when compared with plasma sprayed WC-Co-Cr coatings, Figure 23 and Figure 39, i.e., C16 and CU16 had ~1.5% and CU31 had ~1% of porosity. Based on the literature [97, 101, 102], it was expected that the coating fabricated from the finest powder feedstock would have the lowest porosity. The differences in carbides size and their morphology among the studied coatings can be observed in Figure 39d-f. Irregularly shaped carbides with a size above 1 µm were mostly contained in the C16 coating produced from the coarsest powder feedstock. In contradistinction to the C16 coating, spherical shaped WC

particles with a size below 1 µm were predominantly presented in the microstructure of the CU16 and CU31 coatings that were sprayed utilizing ultra-fine carbides. The spherical morphology of particles indicated a complete or partial melting of the carbide powder particles during the HVOF spraying process.

5.3.2 Surface topography

The topographic analysis was performed on as-sprayed, as-sprayed modified and polished unmodified coatings. In the case of the polished unmodified surfaces, topography measurements were done to ensure that the root mean square height *Sq* was below 0.20 µm and the surface roughness factor *Rs* was below 1.01; 2D height maps are presented in Figure 40. In the case of the as-sprayed modified surfaces, topography measurements did not reveal any noticeable difference when compared to the as-sprayed unmodified surfaces. Thus, only the results on the as-sprayed unmodified surfaces are presented and discussed in the further text.

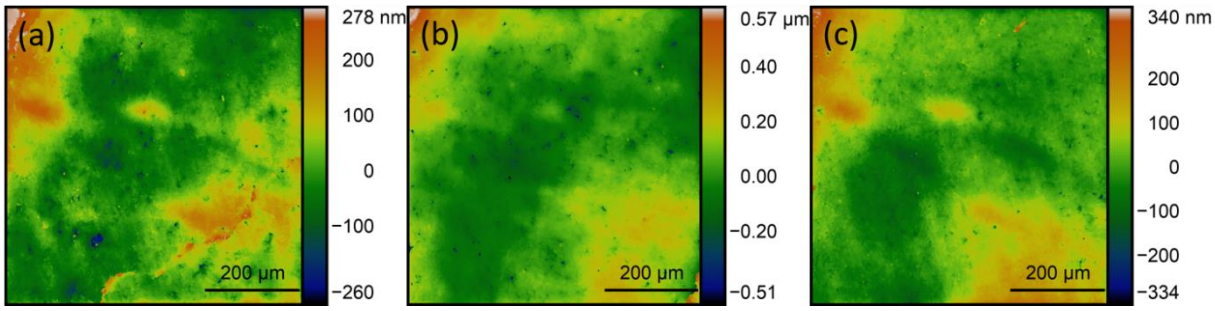

Figure 40 Height maps of (a) C16, (b) CU16 and (c) CU31 polished unmodified coatings

The SEM top-view images of the as-sprayed unmodified C16, CU16 and CU31 coatings are presented in Figure 41. All of the studied coatings showed the presence of the multi-scale roughness, i.e. a large-scale (tens of microns) wavy surface connected to the spraying process [83] with micron-sized (approximately from 2 to 10 microns) peaks and valleys that were covered by ultra-fine WC carbide particles (hundreds of nanometers in size). Apparently, the presence of ultra-fine WC particles significantly enlarged the surface area. Such a unique multi-scale roughness was connected to the agglomerated and sintered initial feedstock powder with ultra-fine WC particles that created nano-scale topographical features on the surface of micron-sized splats.

The measured roughness parameters of the C16, CU16 and CU31 coatings are summarized in Table 17, while Figure 44 represents 3D surface topography figures of the studied coatings. The surface arithmetical mean height *Sa* and the surface root mean square height *Sq* showed a direct connection to the size of the initial feedstock powder. The lowest *Sa* and *Sq* values were measured in the C16 sample produced from the coarsest powder, and the highest *Sa* and *Sq*

values were measured in the CU31 coating fabricated using the finest feedstock powder. The same behavior was reported by Al-Mutairi et al. [94], in which case the WC-Co HVOF-sprayed coatings produced from the finest powder feedstock represented the highest roughness. Such behavior was the opposite of that of plasma sprayed coatings, in which case the roughness increases with an increasing powder size Vassen et al. [106].

Table 17 Roughness parameters of surfaces of C16, CU16 and CU31 as-sprayed unmodified coatings

Coating	Sa [µm]	Sq [µm]	Ssk [-]	Sku [-]	Rs [-]
C16-AS	3.8	4.9	0.21	4.35	2.13
CU16-AS	5.4	6.7	0.18	3.03	2.23
CU31-AS	6.8	8.3	0.04	2.56	1.92

The opposite behavior can be observed in the case of the skewness *Ssk* and kurtosis *Sku*. The noticeable difference between C16/CU16 and CU31 in the skewness values showed that the surfaces of the C16/CU16 coatings were composed of more peaks than valleys/pores ($Ssk > 0$); while the surface of the CU31 coating showed a relatively equal distribution of valleys/pores and peaks ($Ssk \sim 0$). The kurtosis values indicated that the finer powder feedstock resulted in flatter peaks and valleys. Sharp-cut peaks and valleys covered the surface of the C16 coating ($Sku > 3$), the surface of the CU16 coating had a smaller distribution of narrow peaks and valleys ($Sku \sim 3$), and the surface of the CU31 coating was predominantly covered by the flattened peaks and valleys ($Sku < 3$). The difference in the skewness and the kurtosis can be clearly observed in 3D topography illustrations, Figure 42, where the variation of distribution and shape of the peaks and the valleys/pores is visualized.

Finally, the comparison of the surface roughness factor *Rs* of the C16 coating produced from coarse powder ($Rs \sim 2.13$) and the CU16 coating produced from coarse powder with ultra-fine WC particles ($Rs \sim 2.23$) proved the enlarging effect of the embedded ultra-fine WC particles on the surface area.

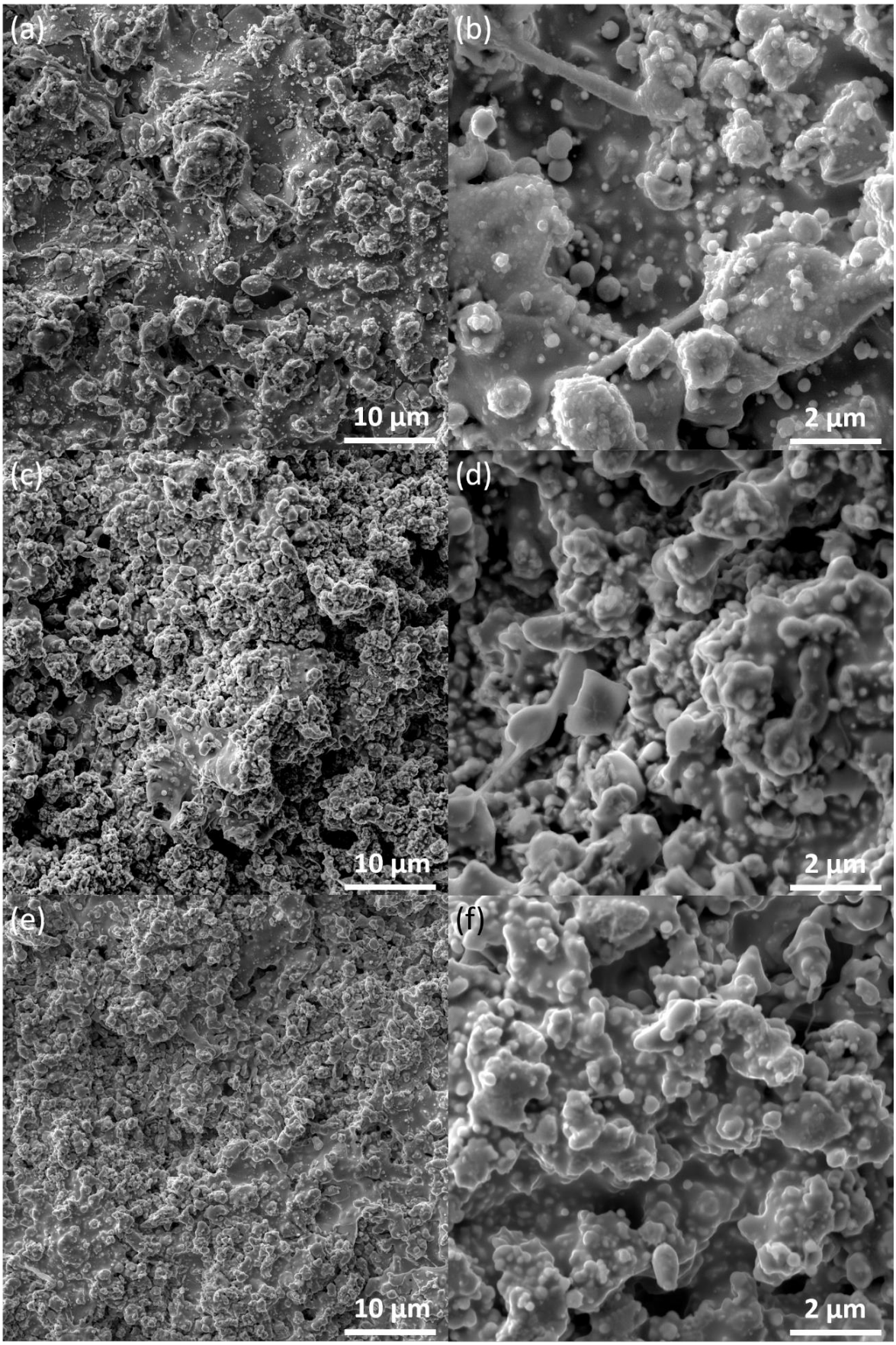

Figure 41 Top-view of (a, b) C16, (c, d) CU16 and (e, d) CU31 as-sprayed unmodified coatings

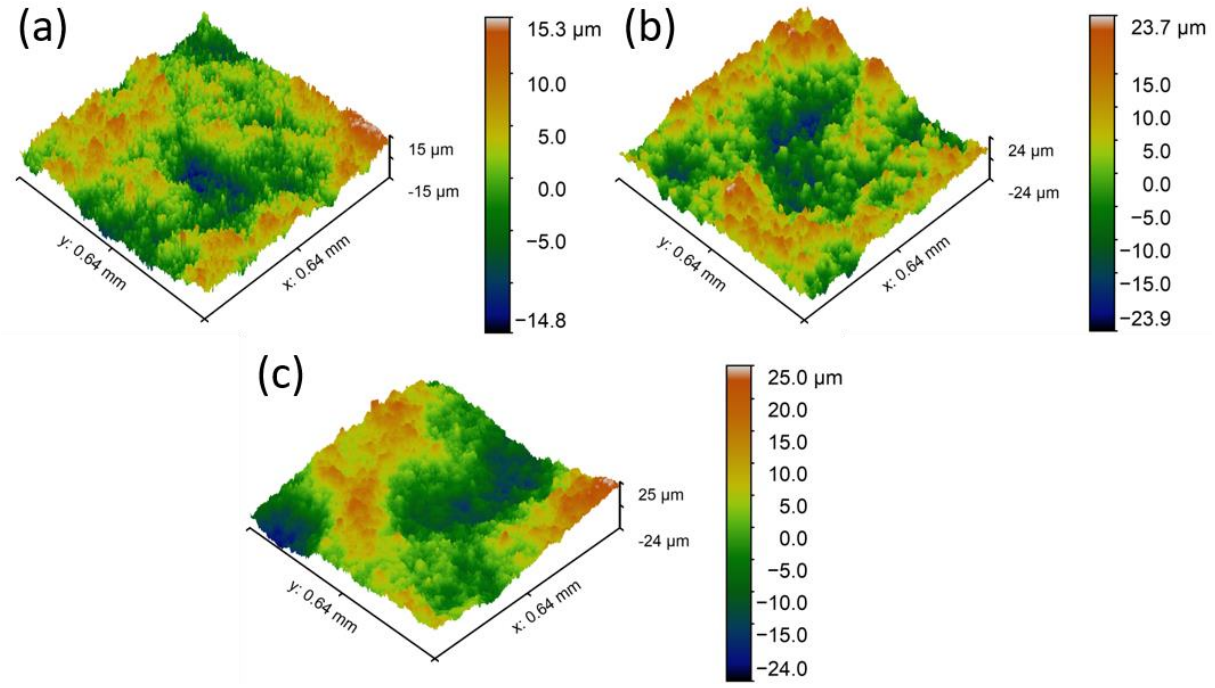

Figure 42 3D topography illustration of surfaces of (a) C16, (b) CU16 and (c) CU31 as-sprayed unmodified coatings

5.3.3 Wetting behavior

For proper estimation of effects of surface chemistry and surface topography on wetting behavior, the water contact angle and surface free energy measurements were carried out on as-sprayed, polished (with the eliminated effect of surface topography), as-sprayed modified (with the eliminated effect of the initial WC-Co-Cr surface chemistry) and the polished modified C16, CU16 and CU31 cermet coatings.

Polished and polished modified states

At first, to isolate the surface chemistry effect, polished and polished modified (Sq < 0.2 µm and Rs < 1.01) coatings were analyzed using Young's equation (Eq. 1). The results of the measurements of water contact angle (WCA), surface free energy (SFE) and distribution of its components are presented in Table 18 and Figure 43. It was found that all the samples showed hydrophilic behavior with a WCA ranging from ~50° up to ~70° in the polished unmodified state, while Si-oil modification amplified water repellency up to the hydrophobic state with a WCA of ~105° for all the modified samples. The obtained results on WCA and SFE measurements of the C16, CU16 and CU31 P - M samples were in a good agreement with the literature [71, 107]. A noticeable difference in the WCA and SFE values was found between the C16/CU16 and CU31 samples, Table 18. As the surface topography of the polished samples was nearly identical, the difference in the wetting behavior was predominantly related to the

differences in chemistry. Following the XPS quantitative analysis results, the surface chemistry of the C16, CU16 and CU31 samples was represented by polar W-O oxides and polar W-C carbides, providing hydrophilic behavior due to the polar-polar interaction with water. The only difference was found in the deconvoluted C 1s spectra of the CU31 sample, revealing the presence of an additional small peak at ~285 eV that was addressed to the C-H compound. It was calculated that this small peak of C-H compound corresponded to ~10 at. % of the whole C 1s spectra. Thus, it can be concluded that even though all samples passed through the proper cleaning procedure before the XPS, WCA and SFE measurements, some C-H hydrocarbons were still present on the surface.

Table 18 Water contact angle and surface free energy values of the polished and polished modified C16, CU16 and CU31 coatings

Sample	State	WCA [°]	SFE [mJ/m^2]	γ^d [mJ/m^2]	γ^P [mJ/m^2]	γ^p/SFE
C16	P	55 ± 1	50.26	35.71	14.55	0.29
	P-M	107 ± 2	27.05	27.00	0.05	<0.01
CU16	P	53 ± 2	51.30	36.46	14.84	0.29
	P-M	106 ± 1	27.76	28.73	0.03	<0.01
CU31	P	68 ± 1	46.58	37.36	9.23	0.20
	P-M	105 ± 2	28.21	28.16	0.05	<0.01

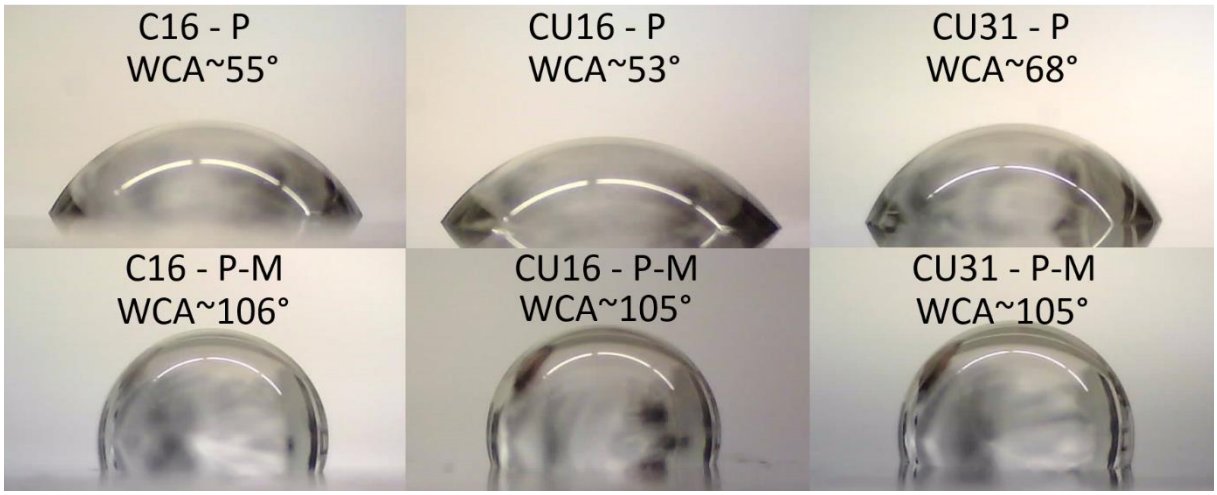

Figure 43 Water droplet behavior on (top) polished and (bottom) polished modified C16, CU16 and CU31 coatings

Recent studies have already reported [91, 108] on the effect of non-polar hydrocarbons on hydrophobic behavior. The solid surface containing a higher amount of metallic phase was supposed to provide a higher probability for hydrocarbons to be adsorbed due to the strong electron-accepting nature of metal cations. Following the Rietveld refinement, the CU31 coating showed the highest content of the pure W phase in comparison to the C16/CU16 coatings, namely 26 % wt. vs. 12 % wt., Table 14. Therefore, it could explain the presence of additional C-H peak in deconvoluted C 1s spectra of the CU31 sample.

As mentioned in the "Review" chapter, the Owens-Wendt theoretical model [13] described surface free energy as the sum of the polar γ^P and dispersive γ^d (non-polar) components. Both of them are listed in Table 18 and, for clarity, the contribution of the polar component to the SFE value is presented separately as γ^P/SFE ratio as well. The contribution of the polar component to the SFE was notably lower in the case of the CU31 sample compared to the C16/CU16 samples. Based on the XPS quantitative analysis and further spectra deconvolution, it can be concluded that the non-polar C-H hydrocarbons adsorbed on the surface of the W grains were responsible for the higher WCA value, lower SFE value and lower γ^P/SFE ratio of the CU31 coating.

The values of WCA, SFE and distribution of polar/non-polar components of the polished modified C16, CU16 and CU31 coatings were nearly equal, representing hydrophobic behavior for all three coatings. The obtained results were very close to polydimethylsiloxane (PDMS) [109], the base of Si-oil applied for modification of the surfaces.

As-sprayed and as-sprayed modified states

The analysis of the WCA of the as-sprayed unmodified C16, CU16 and CU31 coatings, Table 19 and Figure 44, revealed hydrophobic and almost superhydrophobic behavior of the C16 and CU16 coatings. To the best of the author's knowledge, this was the first report on WC-Co-Cr cermet HVOF sprayed coating with a WCA value above 140° in the as-sprayed state. The boundary "hydrophilic-hydrophobic" behavior was detected for the CU31 coating (WCA ~ 88°). The Si-oil surface modification amplified hydrophobicity up to the superhydrophobic state with a very low sliding angle (SA) and SFE values for all the studied coatings, as listed in Table 19 and presented in Figure 44. The best water repellency and mobility performance was found on the C16 and CU16 coatings with a WCA > 170° and a SA of 8° and 5°, respectively.

Table 19 Water contact angle, sliding angle and surface free energy values of the as-spayed and as-sprayed modified C16, CU16 and CU31 coatings

Sample	State	WCA [°]	Sliding angle [°]	SFE [mJ/m^2]
C16	AS	122 ± 3	-	17.37
	AS-M	>170	8	2.08
CU16	AS	143 ± 2	-	12.79
	AS-M	>170	5	2.10
CU31	AS	88 ± 2	-	28.49
	AS-M	152 ± 4	10	2.85

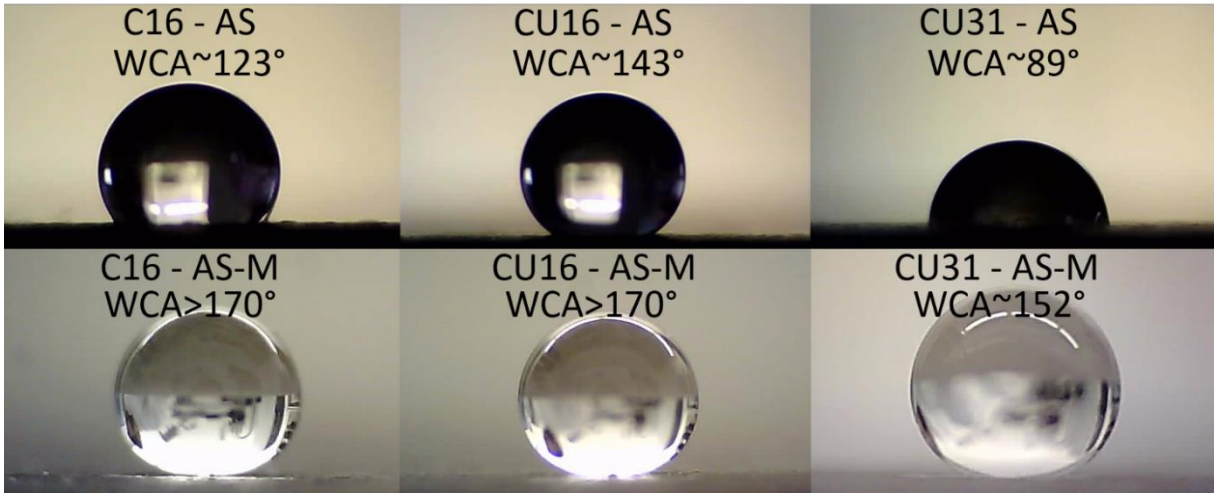

Figure 44 Water droplet behavior on (top) the as-sprayed and (bottom) as-sprayed modified C16, CU16 and CU31 coatings

Based on the hydrophilic behavior of all of the coatings in the polished unmodified state, it could be concluded that surface roughness amplified hydrophobicity, resulting in much higher values of WCA and lower values of SFE. Moreover, such a result showed that the wetting behavior of the C16, CU16 and CU31 coatings did not follow the Wenzel wetting regime, but followed the Cassie-Baxter (Eq. 7) or combined (Eq. 8) regime of wetting.

According to the combined Wenzel-Cassie-Baxter wetting regime, which was found useful for the description of surfaces with a multi-scale topography, hydrophobicity increases with an increasing surface roughness factor *Rs*. Thereby, the higher hydrophobicity of the as-sprayed and as-sprayed modified C16 (*Rs* = 2.13) and CU16 (*Rs* = 2.23) coatings was promoted by a higher surface roughness factor *Rs*, Table 17.

Using Eq. 8 for the combined regime of wetting, the calculated f_s values were 4.1% for the C16, 3.8% for the CU16 and 23.1% for the CU31 in the as-sprayed modified conditions. The f_s value shows the area of the droplet that is in contact with the solid surface. Thus, 95.9% (for the C16), 96.2% (for the CU16) and 76.9% (for the CU31) area of the water droplet was related, in fact, to the liquid-gas (air) contact, providing a high water repellency and mobility.

Furthermore, the two most hydrophobic coatings (C16 and CU16) had very close skewness *Ssk* values (*Ssk* ~ 0.2), Table 17. Since *Ssk* > 0 represented the surface with a higher number of peaks than valleys/pores, as seen in Figures 41-42, it was assumed that water droplets were kept on the top of the peaks, possessing Cassie-Baxter or a combined Wenzel and Cassie-Baxter wetting state, with entrapped air-pockets between the liquid and solid surfaces. At the same time, *Ssk* ~ 0 of the CU31 coating revealed an equal distribution of peaks and valleys/pores, thus providing more valleys/pores to be covered by water droplets, giving lower WCA values in both the as-sprayed and as-sprayed modified conditions.

Ultra-fine WC carbide particles embedded into the Co-Cr metallic matrix formed nano- and submicron-sized peaks, see Figure 45, on the surface of micron-sized splats of WC-Co-Cr feedstock powder particles that were molten or partially molten during the HVOF spraying process. These micron-scale peaks covered by nano-scale peaks and valleys/pores enlarged the total surface area, providing more space for air-pockets to be entrapped, improving hydrophobic behavior. The same amplification effect of fine carbides on the hydrophobic properties of the cermet HVAF coatings was reported by Vijay et al. [72]. Additionally, the peaks formed by WC particles, Figure 45, could act as a barrier for the three-phase contact line movement, preventing the spreading of the water droplet, thus increasing its WCA and hydrophobicity.

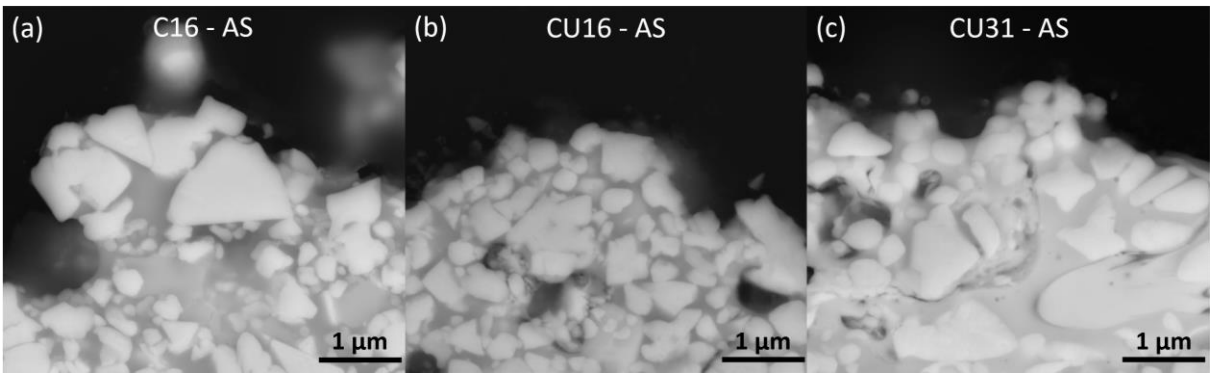

Figure 45 Cross-sections of the as-sprayed (a) C16, (b) CU16 and (c) CU31 coatings' top part with WC carbides (white color) embedded into Co-Cr metallic matrix (light gray color)

These experiments showed that using the agglomerated and sintered WC-Co-Cr powder feedstock in HVOF spraying enables the deposition of coatings with a multi-scale surface roughness, leading to the hydrophobic behavior in the as-sprayed state and the superhydrophobic behavior in the as-sprayed modified state. In both the as-sprayed and as-sprayed modified states, the highest water repellency and water mobility were observed in the CU16 coating (the WCA was close to 150° in the as-sprayed state; WCA > 170° and SA ~ 5° in the as-sprayed modified state) fabricated from bi-modal powder feedstock (coarse powder with ultra-fine WC particles). Therefore, using bi-modal powder feedstock can ensure the optimal surface topography with a high water repellency.

5.4 Mechanical properties, wear/erosion resistance and non-destructive durability tests of hydrophobic WC-Co-Cr coatings

5.4.1 Microhardness measurements

The mechanical properties of the WC-Co-Cr HVOF as-sprayed C16, CU16 and CU31 coatings (the subject of the previous chapter) were evaluated using the Vickers microhardness test at samples cross-sections. At least 12 indents of HV 0.3 load (300 g) were analyzed per sample.

The highest microhardness was measured for the CU16 coating (1155 ± 112 HV) and nearly equal values were measured for the CU31 and C16 coatings (988 ± 66 HV and 966 ± 119 HV, respectively). The microhardness of all the studied coatings was in agreement with the literature [96, 110–112]. Commonly, the microhardness of WC-Co/WC-Co-Cr coatings is amplified (i) by the amount of retained non-decarburized WC particles [96] and (ii) by the presence of ultra-fine WC particles [96, 110, 113]. The CU16 coating with the highest microhardness was produced from coarse powder with ultra-fine WC particles and with a WC content of 49 wt.%, Table 14. In contrast, nearly equal microhardness values were measured for the C16 coating (with 51 wt.% of WC, but produced from a coarse powder only) and for the CU31 coating (produced from fine powder with ultra-fine WC particles, where only of about 20 wt.% of WC phase remained).

5.4.2 Cavitation erosion resistance

For the cavitation erosion (CE) resistance test, the two most hydrophobic C16 and CU16 samples in the as-sprayed and as-sprayed modified states were selected.

The as-sprayed modified samples were tested for 20 minutes, and the test was terminated once the superhydrophobic effect was lost. The WCA value decreased down to ~140-145° and

was associated with the gradual removal of the Si-oil modification layer. The mass loss after 20 minutes of testing was ~0.01 g in both samples.

The as-sprayed unmodified C16 and CU16 samples were tested for 165 min and 120 min, respectively, and stopped once the loss of hydrophobicity was observed. In this case, the mass loss was found to be different for the two coatings. The C16 sample produced from coarse powder revealed a higher resistance to cavitation erosion with a cumulative mass loss of 0.030 (after 120 min) and 0.042 g (after 165 min). On the other hand, the CU16 sample produced from bi-modal powder (coarse powder with ultra-fine WC particles) had a cumulative mass loss of 0.040 g already after 120 min of testing. The cumulative mass loss of both the C16 and CU16 samples was much higher than reported in other studies on WC-Co/WC-Co-Cr coatings [114, 115]. For this research, the surfaces of experimental samples were not ground/polished prior to the CE test, in order to estimate the robustness of hydrophobic behavior. It was reported elsewhere [116] that the surface roughness has a negative effect on CE resistance. The surface roughness, especially multi-scale surface roughness, can be considered to be a surface defect providing inhomogeneity of stress during cavitation [116]. The same reason was most likely responsible for the higher cumulative mass loss of the CU16 sample that showed higher roughness than the C16 sample, Table 17.

The top-views of the C16 and CU16 samples after the CE test are presented in Figure 46. Even though the eroded surfaces of the C16 and CU16 samples were relatively rough after the CE test, the hydrophobic behavior was lost due to the formation of cracks within the coatings, Figure 46 a, c. After the CE test, these cracks promoted gradual penetration of the water droplets into the coating, resulting in a very low water contact angle (WCA was measured in the range from ~35° to ~50°). To prove this observation, an additional surface treatment by Si-oil was carried out to cover the cracks. The WCA after Si-oil treatment increased up to the superhydrophobic state with a WCA ~ 150°, see Figure 47, which was almost 50° higher compared to what was observed on polished modified coatings, Table 18. This result proved that the surface of the C16 and CU16 coatings after the cavitation erosion test remained rough enough to amplify hydrophobic behavior, but the cracks formed within the coatings were responsible for wetting behavior transition from the hydrophobic to hydrophilic state.

5.4.3 Slurry abrasion response test

As for the CE test, the two most hydrophobic as-sprayed and as-sprayed modified C16 and CU16 samples were selected for the Slurry Abrasion Response (SAR) test.

The superhydrophobicity of the as-sprayed modified C16 and CU16 samples was capable of withstanding erosion wear for 48 cycles (1 minute of testing), with a decrease in WCA value down to 140-145°. Additional re-covering of the experimental coatings by Si-oil restored superhydrophobic behavior, resulting in a very high WCA of about 170°. According to author's knowledge, there are no reports evaluating the robustness of the hydrophobic/superhydrophobic coatings utilizing SAR test. Nevertheless, recently published work of Xu et al. [117] can be used at least to provide rough comparison, where, the solution precursor atmospheric/vacuum plasma (SPAPS/SPVPS) sprayed Yb_2O_3 superhydrophobic coatings were subjected to the dry sand erosion test for 25 s, resulting in the decrease of the WCA value from 163° to 96° (for SPAPS Yb_2O_3 coatings) and from 155° to 140° (for SPVPS Yb_2O_3 coatings).

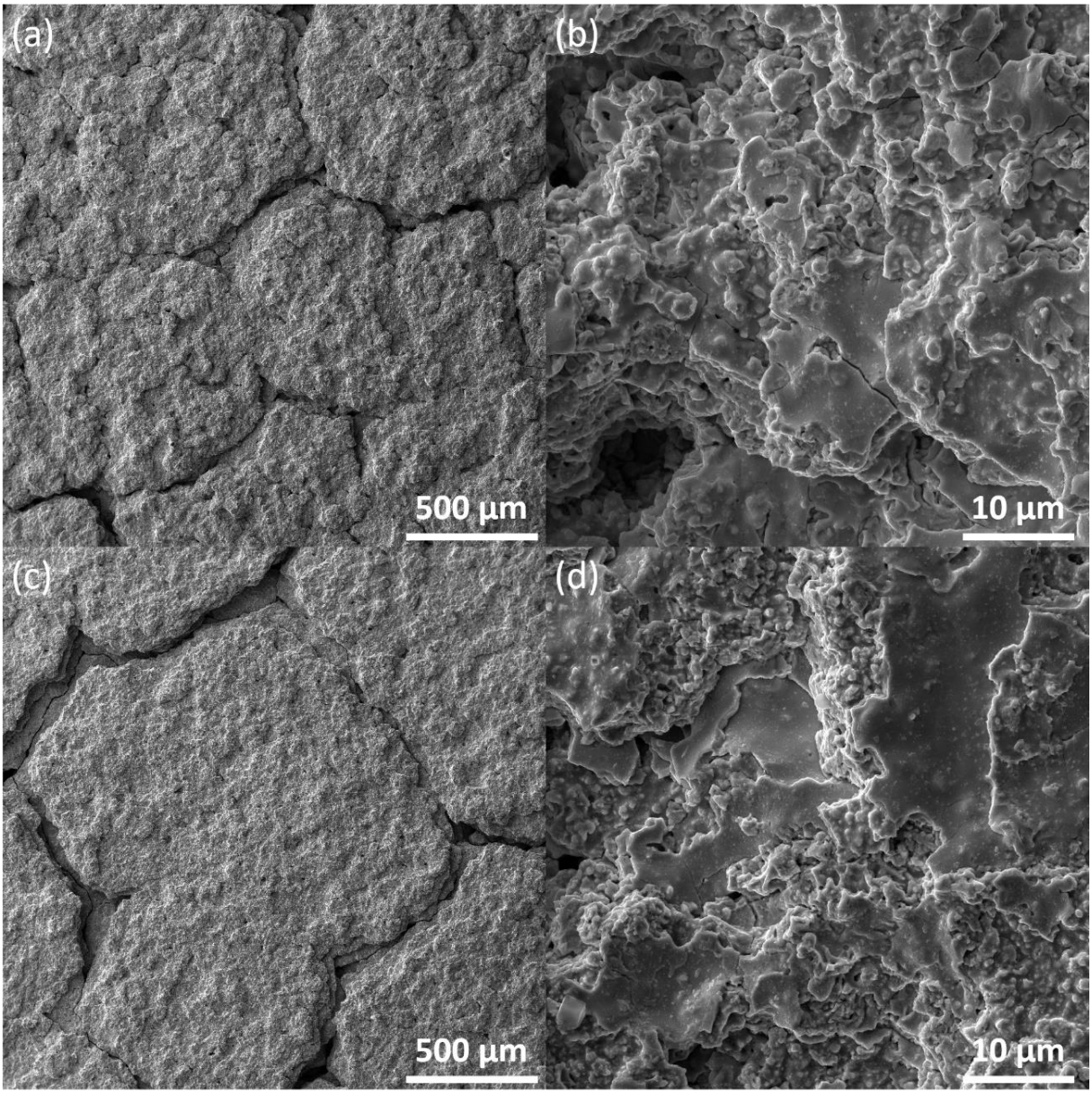

Figure 46 Top-view of (a, b) C16 and (c, d) CU16 as-sprayed coatings after cavitation erosion test

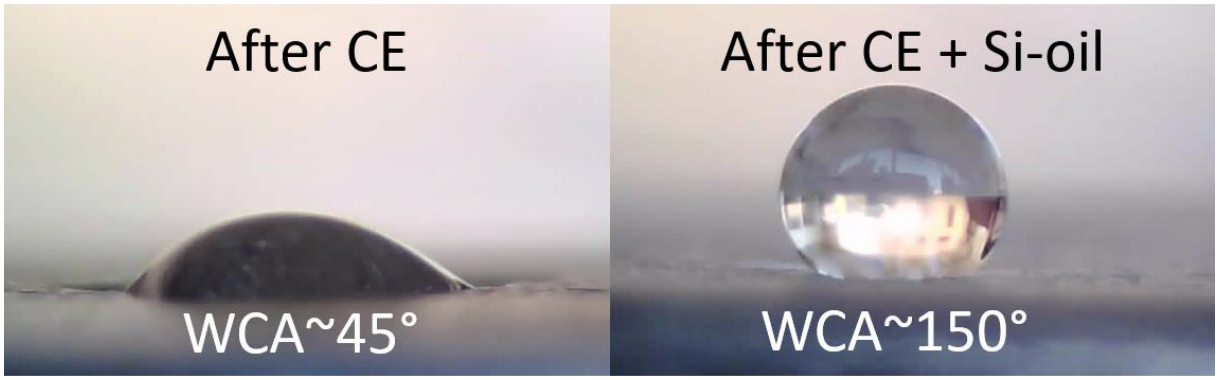

Figure 47 Water droplet behavior on CU-16 as-sprayed coating after cavitation erosion test and after re-covering by Si-oil

Hydrophobic as-sprayed C16 and CU16 samples were tested for 17 280 cycles (6 hours of testing). The changes in surface topography and WCA values were recorded after 4 and 6 hours of testing, as it was found to be the period in which the wetting behavior switched from hydrophobic to hydrophilic, Table 20 and Figure 48. Even though the hydrophilic behavior was observed in both the C16 and CU16 as-sprayed samples, there were still parts of the coatings' surfaces that showed hydrophobic behavior even after 6 hours of testing. These areas are indicated by the black color in Figure 48 right column.

Table 20 Roughness parameters of surfaces of the as-sprayed C16 and CU16 after 4 and 6 hours of the SAR testing

Coating	Time [h]	Sa [µm]	Sq [µm]	Ssk [-]	Sku [-]	Rs [-]
C16 AS	4	2.7	3.4	- 0.17	3.19	1.39
	6	2.2	3.1	- 0.20	3.02	1.11
CU16 AS	4	3.6	4.4	- 0.28	2.82	1.48
	6	2.9	3.7	- 0.31	2.51	1.18

The long-term SAR test had a significant impact on the surface roughness of the as-sprayed coatings which subsequently negatively affected wetting behavior. When comparing the surface topography data of the C16 AS and CU16 AS samples before and after the SAR test, Table 17 and Table 20, it is evident that all roughness parameters decreased in values. During the SAR test, the abrasive alumina particles in the slurry wore the peaks and led to their flattening as the peaks were the first contact points. The WCA values decreased from ~122° to ~118° (after 4 hours) and ~70° (after 6 hours) for the C16 sample, and from ~143° to ~128° (after 4 hours) and ~74° (after 6 hours) for the CU16 sample. The decrease of the surface roughness factor *Rs* was equal for both samples, namely, ~35% and ~50% after 4 and 6 hours of testing,

respectively. It can be pointed out that despite the significant decrease of the surface roughness factor *Rs*, the WCA value did not decrease that much after 4 hours of testing. Such result can be related to the formation of wear-tracks originated during the SAR testing that also influenced surface roughness, Figure 49. However, these wear-tracks were of a very small thickness, thus could not be observed by the utilized laser scanning confocal microscope used to analyze surface topography.

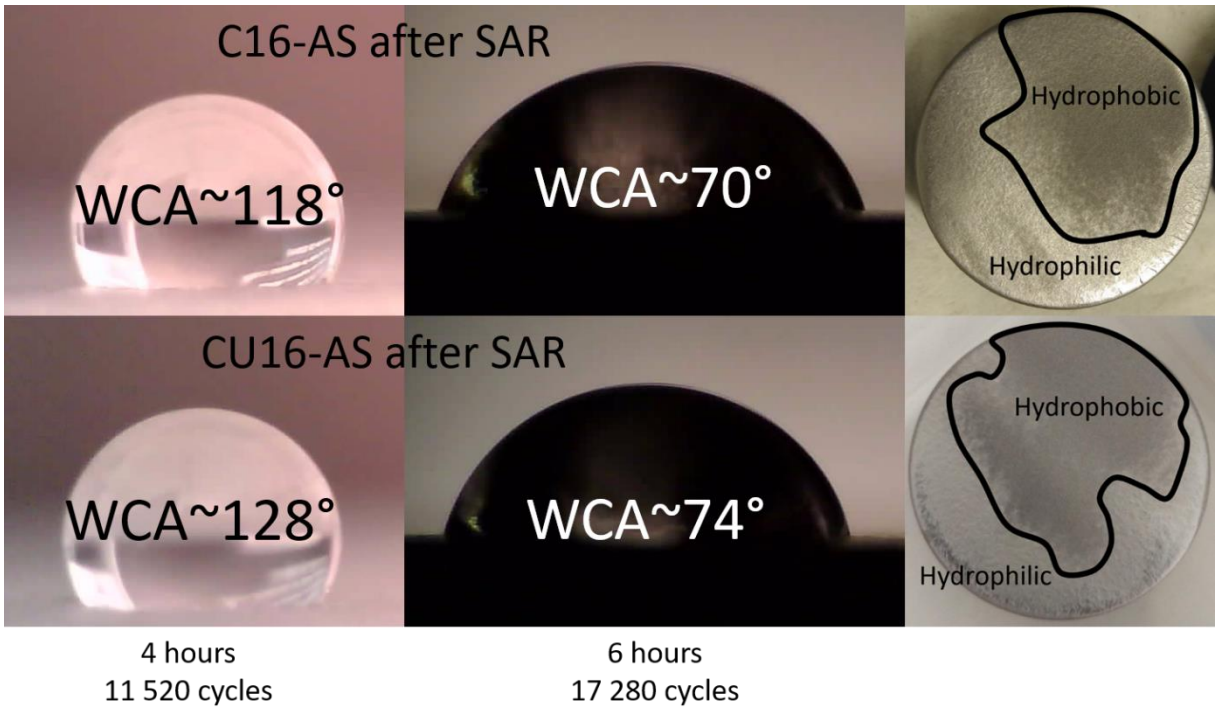

Figure 48 Water droplet behavior on the as-sprayed (top) C16 and (bottom) CU16 samples after 4 and 6 hours of SAR testing; macro-photos with marked hydrophobic and hydrophilic areas of (right-top) the C16 and (right-bottom) CU16 samples after 6 hours of SAR testing

From Figure 49, it is also clearly seen that even after such long-term harsh testing, WC particles incorporated into the Co-Cr matrix remained on the coatings' surface. These two factors, namely the formation of the wear-tracks and the retention of WC particles, were the main reason for the hydrophobic behavior after 4 hours of testing. This result proves the sufficient robustness of the hydrophobic wetting behavior of WC-Co-Cr coatings that could withstand 11 520 cycles and partially remained, even after 17 280 cycles of sacrificial testing.

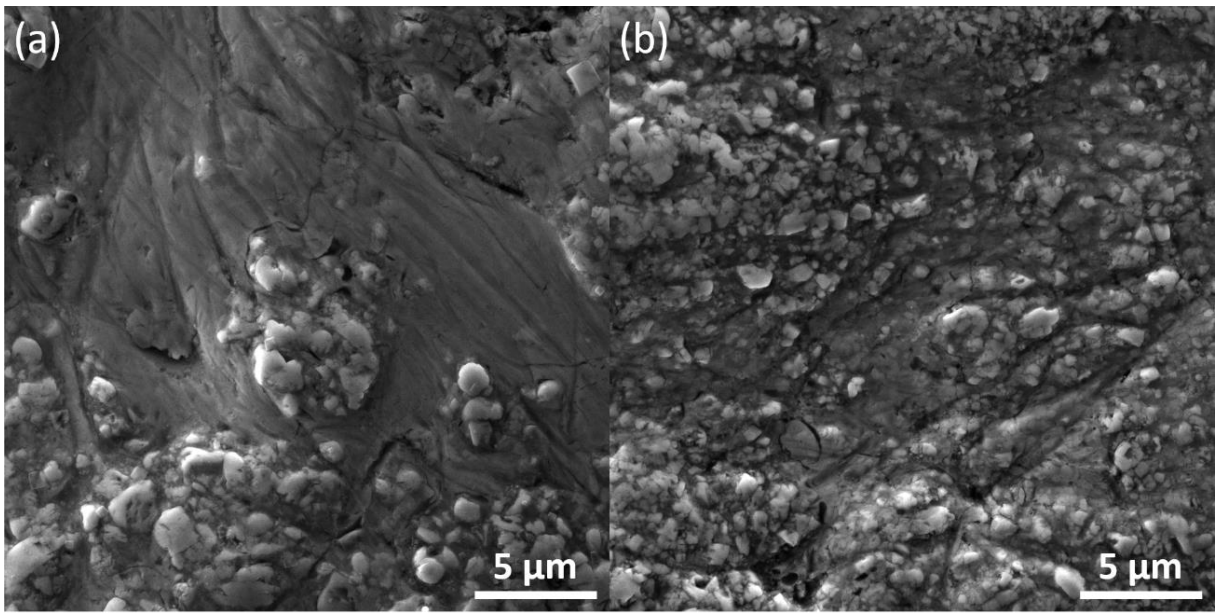

Figure 49 Top-view of the as-sprayed (a) C16 and (b) CU16 samples after the SAR test

5.4.4 Icephobic test

Evaluation of the icephobic behavior was carried out on superhydrophobic as-sprayed modified C16/CU16 samples, hydrophobic as-sprayed and polished modified C16/CU16 samples. Conventional materials, such as aluminum and stainless-steel, were analyzed as well to provide a comparison, as these materials suffered from severe ice-formation and ice-accumulation during the service lifetime [118, 119]. The aluminum and stainless-steel substrates were in the ground state with a surface arithmetic mean height *Sa* of ~1.2 µm, and the measured WCA values were of ~68° and ~71° respectively, while the contact angle of frozen droplets at the same substrates decreased to ~49° and ~53°. A similar decrease in the contact angle value was observed at C16/CU16 samples as well. The decrease in the contact angle value was of ~10° for polished modified coatings, ~4° for as-sprayed coatings and ~20° for as-sprayed modified coatings, as summarized in Table 21 and shown in Figure 50.

It is evident that the frozen droplets on the surface of C16/CU16 AS-M coatings kept the spherical shape, while the rest of the analyzed surfaces created frozen droplets with a peak on the top, see Figure 50. In case of the C16/CU16 AS-M samples, the ice formation started above the solid surface, but not at the "solid-liquid" interface. This was related to the coatings' multi-scale surface roughness and a very low "solid-liquid" contact area of C16/CU16 AS-M samples, that was 4.1 % and 3.8 % respectively [120]. The rest of the analyzed surfaces promoted nucleation of the ice at the "solid-liquid" interface due to a higher "solid-liquid" interface contact area. Considering that the ice adhesion strength decreases with an increasing WCA value [121], it can be concluded that the C16/CU16 as-sprayed modified coatings possess a

significantly improved icephobicity in comparison to unmodified coatings and conventional construction materials.

Table 21 Water and ice contact angle values of Al/SS substrates and C16/CU16 coatings

Sample	WCA [°]	Ice CA [°]
Al	68 ± 2	49 ± 1
SS	71 ± 4	53 ± 2
C16 AS	122 ± 3	120 ± 1
C16 P-M	107 ± 2	93 ± 3
C16 AS-M	>170	153 ± 1
CU16 AS	143 ± 2	139 ± 1
CU16 P-M	106 ± 1	95 ± 2
CU16 AS-M	>170	153 ± 2

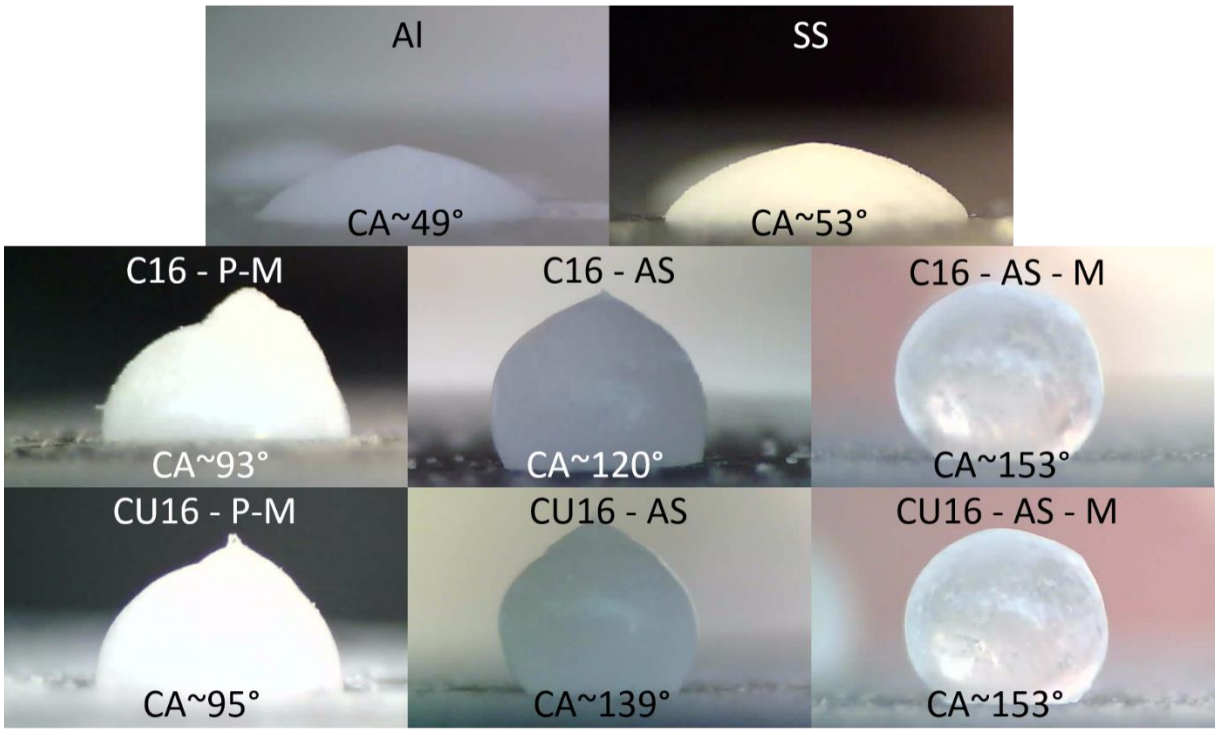

Figure 50 Icephobic behavior of Al/SS substrates and C16/CU16 coatings

5.4.5 Acid-phobic test

For the acid-phobic test, a droplet of the mixture of concentrated sulfuric acid in water (4.7 M, 9.3 M and 14 M) and pure concentrated sulfuric acid were deposited on the surface of the C16/CU16 as-sprayed modified and the C16/CU16 as-sprayed coatings. The results are summarized in Table 22. Regarding the C16/CU16 as-sprayed coatings, the measured contact

angles of the three mixtures were in the range of ~19° up to ~25°, and the droplets of concentrated sulfuric acid were spread completely on the coatings surface. In case of the as-sprayed modified C16/CU16 coatings, the contact angle values were found to be much higher, reaching ~153° (for 4.7 M and 9.3 M) and ~148° (for 14 M). The droplets of the 4.7 M and 9.3 M H_2SO_4 mixtures easily rolled off once the coatings surface was tilted at ~10°, leaving the surface without any visible damage. While the droplets of the 14 M H_2SO_4 mixture adhered to the surface promoting the degradation of the Si-oil layer. In case of concentrated sulfuric acid, the droplets spread over the coatings surface revealing a ~5° contact angle with complete deterioration of the modification layer. The concentrated sulfuric acid and its water-mixtures wetting behavior of the CU16 as-sprayed and as-sprayed modified coating is shown in Figure 51. In recent studies [122], it was reported on the importance of increasing the corrosion-resistance of WC-based cermet coatings due to the corrosive nature of their service environments. This short-term test demonstrates the potential of Si-oil surface treatment to improve corrosion resistance and increase the service lifetime of the WC-Co-Cr coatings.

Table 22 Concentrated sulfuric acid and its water-mixtures contact angle values of C16/CU16 coatings

Sample	H_2SO_4 in water mixture CA [°]			H_2SO_4 CA [°]
	4.7 M	9.3 M	14 M	
C16 AS	23 ± 2	20 ± 3	19 ± 1	2 ± 2
C16 AS-M	153 ± 1	153 ± 1	148 ± 3	4 ± 1
CU16 AS	25 ± 1	21 ± 3	20 ± 3	2 ± 2
CU16 AS-M	153 ± 2	153 ± 1	149 ± 2	5 ± 2

5.4.6 Self-cleaning and muddy-water transportation tests

Environmental or artificial contaminations can degrade the superhydrophobic behavior of a surface directly in practical applications. Therefore, the short-term self-cleaning and muddy-water transportation tests were conducted in order to provide a preliminary information on the robustness of superhydrophobic C16/CU16 as-sprayed modified coatings. The hydrophobic C16/CU16 as-sprayed coatings are not presented here due to the fact that they did not possess any water mobility, and the water droplets were adhered to the coatings even in an upside-down position.

During the self-cleaning test, the water droplets were quickly rolling off the tilted surface of the C16/CU16 AS-M coatings, collecting the alumina dust and producing clean lines on the

coatings surface, Figure 52a. As demonstrated in Figure 52b, the continuous flow of muddy water with suspended ultra-fine WC particles was sent onto the tilted surface of the C16/CU16 AS-M coating and quickly rolled off without any apparent contamination remained. These preliminary observations pointed out a promising durability of superhydrophobicity of WC-Co-Cr C16/CU16 AS-M coatings against powder/slurry contaminations and showed similar performance to the case of more expensive REO's superhydrophobic coatings [25].

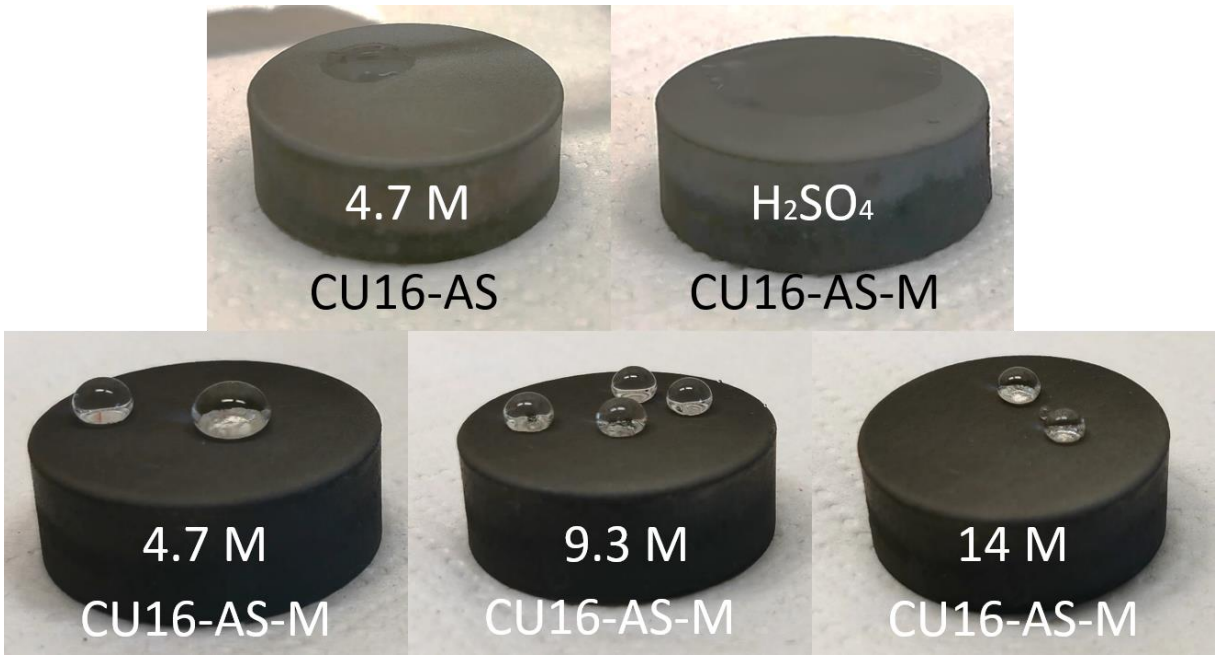

Figure 51 Acid-phobic performance of the CU16 as-sprayed and CU16 as-sprayed modified coatings

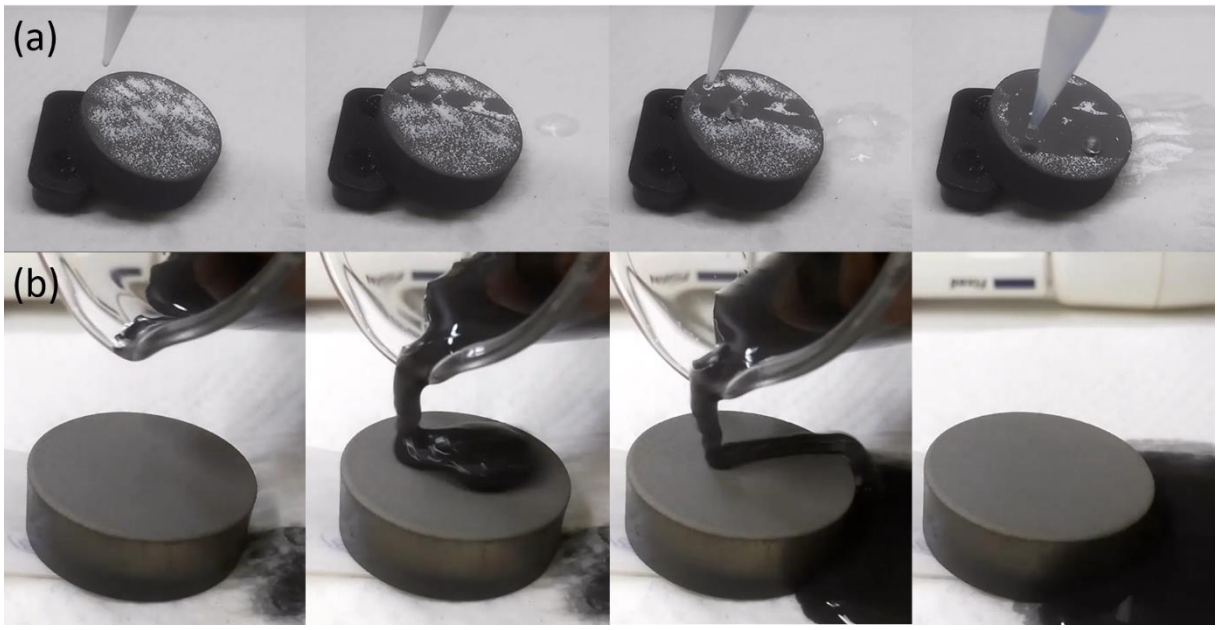

Figure 52 Representation of (a) self-cleaning and (b) muddy-water transportation tests

6 Conclusions

The main aim of the thesis was to produce the wear-resistant coatings with hydrophilic/hydrophobic behavior by means of thermal spraying; to perform a detailed analysis of produced coatings in order to assess the interconnections between microstructure, surface chemistry and surface topography with their wetting behavior; and to estimate the properties and robustness of the wetting behavior of produced coatings.

In the first part of the experimental work, several wear-resistant ceramic and cermet coatings, namely ZrO_2-Y_2O_3, Al_2O_3, Cr_2O_3-SiO_2-TiO_2 and WC-Co-Cr, were produced by means of atmospheric plasma spraying. The topography and the wetting behavior of these experimental coatings were studied in the as-sprayed, ground (#220 abrasive paper) and polished (9, 3, 1 μm diamond pastes) states. All the coatings showed hydrophilic behavior with the Wenzel wetting regime due to the presence of pores/cracks present in the coatings, which resulted in a gradual infiltration of the water droplets into the coatings. The effect of the coatings porosity and/or cracks on the wetting behavior was crucial and, therefore, the influence of surface topography on wetting behavior remained unclear. The highest values of the water contact angle were observed at the coatings in the as-sprayed state. The YSZ and WC-Co-Cr materials were selected for optimization of spraying parameters and further research as the YSZ coating showed the smallest change in WCA values in time and the WC-Co-Cr coating showed the highest WCA value in the as-sprayed state among the studied coatings.

In the second part, the YSZ coatings were produced using liquid and solid feedstocks in order to understand the effect of microstructure on wetting behavior. Four series of samples were produced, namely YSZ coatings with a lamellar microstructure (employing the F4 plasma torch) and with a columnar microstructure (employing the WSP-H and Axial III plasma torches). All the coatings were studied in the as-sprayed state. The comparative analysis of microstructure, surface chemistry and surface topography and their effect on wetting behavior revealed that (i) the YSZ coating with lamellar microstructure (the F4 YSZ coating) promoted hydrophilic behavior with the Wenzel wetting state due to the infiltration of the water into the pores and cracks in the coating; (ii) the presence of pores in the columnar microstructure located between the flat columns promoted almost superhydrophilic behavior with the Wenzel wetting state in the A3-P YSZ coating; (iii) the denser flat columnar microstructure of the A3-D YSZ coating prevented the penetration of water into the coating, resulting in hydrophobic behavior with the Cassie-Baxter wetting state; and (iv) the rough surface of the columns, as well as the high surface area, of the WSP-H YSZ sample provided superhydrophobic behavior with the Cassie-Baxter wetting state.

With the aim to overcome the dependency of wetting behavior on microstructural and topographical features of YSZ coatings, the additional RF-plasma jet surface treatment was made. After the RF-plasma jet surface modification, the organosilicon layer with dendritic structure composed of nano-sized particles was produced. Such a layer provided transition of wetting behavior from hydrophilic (A3-P YSZ sample) and hydrophobic (A3-D YSZ sample) states to superhydrophobic one with the Cassie-Baxter wetting regime. The dendritic structure of the organosilicon layer ensured entrapping of the air-pockets between the nano-sized peaks and valleys resulting in high water repellency and water mobility. Nevertheless, the superhydrophobic behavior with high water mobility of the as-sprayed WSP-H and modified A3-D/A3-P YSZ samples was not able to withstand the short-term water-flush test pointing out the need for further research on fabrication of water-repellent wear-resistant coatings.

The third part of the experimental work aimed to fabricate wear-resistant coatings from WC-Co-Cr cermet materials using three different powder feedstocks, by the means of high-velocity oxy-fuel spraying. The coarse powder, a coarse powder with ultra-fine WC particles and a fine powder with ultra-fine WC particles were used in order to deposit coatings with multi-scale topography. To understand the influence of surface topography and surface chemistry on wetting behavior, all the coatings were studied in the as-sprayed, polished (isolated effect of surface chemistry), as-sprayed modified (isolated effect of surface topography) and polished modified states. A technologically simple way to improve surface hydrophobicity based on a Si-oil treatment was provided. All cermet coatings were hydrophilic in the polished state, but hydrophobic and almost superhydrophobic in the as-sprayed state. Additional surface modification provided by a Si-oil turned wetting behavior into the superhydrophobic state of all cermet coatings. The highest water contact angle value (WCA ~ 143° in the as-sprayed; WCA > 170° in the as-sprayed modified) and the lowest sliding angle (SA ~ 5°) was found for the CU16 coating in the as-sprayed and as-sprayed modified states. The CU16 coating was produced from a coarse powder with ultra-fine WC particles, revealing that such a combination provided an optimal multi-scale surface topography for water repellency and water mobility. This is the first work reporting a WCA value as high as ~143° for as-sprayed WC-Co-Cr coatings. The wetting behavior of as-sprayed and as-sprayed modified coatings followed Cassie-Baxter or a combined Wenzel and Cassie-Baxter wetting regime with entrapped air-pockets in nano-scale topographical features. These air-pockets played the role of a barrier between a water droplet and a solid surface, preventing their contact, thus increasing hydrophobic performance. It was calculated that only 3.8% of the water droplet surface was in contact with the coating's surface, while the rest 96.2% was in contact with air.

Finally, in the last experimental part, the mechanical properties of cermet coatings and the robustness of hydrophobic/superhydrophobic behavior were evaluated by microhardness measurements, cavitation erosion, slurry abrasion response and unconventional non-destructive tests. The highest microhardness was measured for the CU16 coating produced from the coarse powder with ultra-fine WC particles. The superhydrophobic behavior of experimental samples was lost after 20 min of the cavitation erosion test and after 48 cycles of the slurry abrasion response test, pointing to the need for further research on improvement of the coatings surface modification. Even though these obtained results were better than what was reported in the literature for thermal sprayed coatings produced from expensive REO's precursors. The robustness of the hydrophobic behavior of cermet coatings was able to withstand cavitation for almost three hours (165 min); 11 520 cycles (4 hours) and partially remained after 17 280 cycles (6 hours) of slurry abrasion testing. These results showed that the hydrophobicity of the cermet coatings was robust enough even for demanding sacrificial industrial applications. Interestingly, it was observed that the produced wear tracks played an amplification role in hydrophobicity due to an enlarged surface area. Non-destructive tests on the icephobic, acid-phobic, self-cleaning and muddy-water transportation performance of the superhydrophobic C16 and CU16 coatings were carried out. The icephobic performance showed that C16 and CU16 as-sprayed modified coatings can significantly increase the icephobicity of conventional constructional materials. The acid-phobic test demonstrated the potential of the Si-oil surface treatment to improve of corrosion resistance and increase the service lifetime of the WC-Co-Cr coatings. The self-cleaning and muddy-water transportation tests also revealed good results, with no apparent contamination or negligible wear of the superhydrophobic layer.

Future work

Based on the obtained results in the thesis on the superhydrophobic behavior of (i) YSZ WSP-H coatings and (ii) on the highly-hydrophobic/superhydrophobic behavior of unmodified/modified WC-Co-Cr cermet coatings, there is still a need for further research. It is planned to produce YSZ coatings using solution precursor plasma spraying in order to analyze their icephobic/anti-icing performance for wind turbine and aerospace applications. The high porosity presented in the columnar microstructure of YSZ coatings is also an advantage for the above-mentioned industrial applications. Such research belongs to the field of applied science, while the effect of surface roughness, e.g. estimation of the fractality of the columns and its effect on wetting behavior, is a highly interesting basic research topic. Nevertheless, the columnar microstructure is not expected to be resistant to wear and/or cavitation erosion. Therefore, further optimization of the feedstock WC-Co-Cr powder, or other cermet compositions, could be a solution to the development of one-step technology to fabricate wear- and cavitation-resistant superhydrophobic coatings that could be useful in future sacrificial applications. The second possibility is to improve the coatings via the additional surface treatment, or to modify their initial feedstock directly by a hydrophobic agent. In the present work, a technologically simple way to amplify hydrophobic properties was also presented. However, further research on this topic is obviously needed, based on the results of slurry abrasion response and cavitation erosion resistance tests, revealing the need for the development of the coatings modification layer with improved hardness and adhesion.

As most of the currently published reports on the topic of hydrophobic/superhydrophobic materials/coatings are focused on expensive rare-earth element oxides and their precursors, the aforementioned materials are significantly less expensive alternatives, especially for applications where mechanical robustness is required.

Bibliography

[1] Y. YUAN, T. R. LEE. Contact angle and wetting properties. *Springer Series in Surface Sciences*. 2013, **51**(1), 3–34. doi:10.1007/978-3-642-34243-1_1

[2] A. LAFUMA, D. QUÉRÉ. Superhydrophobic states. *Nature Materials*. 2003, **2**, 457-460 doi:10.1038/nmat924

[3] J. DRELICH, E. CHIBOWSKI. Superhydrophilic and superwetting surfaces: Definition and mechanisms of control. *Langmuir*. 2010, **26**(24), 18621–18623. doi:10.1021/la1039893

[4] L. B. BOINOVICH, A. M. EMELYANENKO. Hydrophobic materials and coatings: principles of design, properties and applications. *Russian Chemical Reviews*. 2008, **77**(7), 583–600. doi:10.1070/rc2008v077n07abeh003775

[5] T. YOUNG. An essay to the cohesion of fluids. *Philoshopical Transaction of the Royal Society of London*. 1804, 65–87. doi:10.1098/rstb.1983.0080

[6] D. E. PACKHAM. Surface energy, surface topography and adhesion. *International Journal of Adhesion and Adhesives*. 2003, **23**(6), 437–448. doi:10.1016/S0143-7496(03)00068-X

[7] A. RUDAWSKA, E. JACNIACKA. Analysis for determining surface free energy uncertainty by the Owen-Wendt method. *International Journal of Adhesion and Adhesives*. 2009, **29**(4), 451–457. doi:10.1016/j.ijadhadh.2008.09.008

[8] A. THORPE, V. PETERS, J. R. SMITH, T. G. NEVELL, J. TSIBOUKLIS. Poly(methylpropenoxyfluoroalkylsiloxane)s: A class of fluoropolymers capable of inhibiting bacterial adhesion onto surfaces. *Journal of Fluorine Chemistry*. 2000, **104**(1), 37–45. doi:10.1016/S0022-1139(00)00225-6

[9] W. CHEN, A. Y. FADEEV, M. C. HSIEH, D. ÖNER, J. YOUNGBLOOD, T. J. MCCARTHY. Ultrahydrophobic and ultralyophobic surfaces: Some comments and examples. *Langmuir*. 1999, **15**(10), 3395–3399. doi:10.1021/la990074s

[10] J. GENZER, K. EFIMENKO. Recent developments in superhydrophobic surfaces and their relevance to marine fouling: A revie*w*. *Biofouling*. 2006, **22**(5) doi:10.1080/08927010600980223

[11] T. NISHINO, M. MEGURO, K. NAKAMAE, M. MATSUSHITA, Y. UEDA. The lowest surface free energy based on -CF3 alignment. *Langmuir*. 1999, **15**(13), 4321–4323 doi:10.1021/la981727s

[12] J. SCHUSTER, M. C. E. SCHVEZOV, M. R. ROSENBERGER. Analysis of the results of surface free energy measurement of Ti6Al4V by different methods. *Procedia Materials Science*. 2015, **8**, 732–741. doi:10.1016/j.mspro.2015.04.130

[13] D. K. OWENS, R. C. WENDT. Estimation of the surface free energy of polymers. *Journal of Applied Polymer Science*. 1969, **13**(8), 1741–1747 doi:10.1002/app.1969.070130815

[14] *Dispersive & polar parts of the surface energy - DataPhysics Instruments* [online]. https://www.dataphysics-instruments.com/knowledge/understanding-interfaces/dispersive-polar-parts/

[15] K. SONG, J. LEE, S. O. CHOI, J. KIM. Interaction of surface energy components between solid and liquid on wettability, and its application to textile anti-wetting finish.

Polymers. 2019, **11**(3) doi:10.3390/polym11030498

[16] R. N. WENZEL. Surface roughness and contact angle. *Journal of Physical & Colloid Chemistry*. 1949, **53**(9), 1466–1467. doi:10.1021/j150474a015

[17] R. N. WENZEL. Resistance of solid surfaces to wetting by water. *Industrial and Engineering Chemistry*. 1936, **28**(8), 988–994. doi:10.1021/ie50320a024

[18] A .B. D. CASSIE, S. BAXTER. Wettability of porous surfaces,. *Transactions of the Faraday Society*. 1944, **40**(5), 546–551. doi:10.1039/tf9444000546

[19] P. XU, T. W. COYLE, L. PERSHIN, J. MOSTAGHIMI. From lotus effect to petal effect: Tuning the water adhesion of non-wetting rare earth oxide coatings. *Journal of the European Ceramic Society*. 2020, **40**(4), 1692–1702. doi:10.1016/j.jeurceramsoc.2019.12.003

[20] J. DRELICH, A. MARMUR. Physics and applications of superhydrophobic and superhydrophilic surfaces and coatings. *Surface Innovations*. 2014, **2**(4), 211–227. doi:10.1680/si.13.00017

[21] Y. Y. YAN, N. GAO, W. BARTHLOTT. Mimicking natural superhydrophobic surfaces and grasping the wetting process: A review on recent progress in preparing superhydrophobic surfaces. *Advances in Colloid and Interface Science*. 2011, **169**(2), 80–105. doi:10.1016/j.cis.2011.08.005

[22] J. DRELICH, E. CHIBOWSKI, D. D. MENG, K. TERPILOWSKI. Hydrophilic and superhydrophilic surfaces and materials. *Soft Matter*. 2011, **7**(21), 9804. doi:10.1039/c1sm05849e

[23] D. AHMAD, I. VAN DEN BOOGAERT, J. MILLER, R. PRESSWELL, H. JOUHARA. Hydrophilic and hydrophobic materials and their applications. *Energy Sources, Part A: Recovery, Utilization, and Environmental Effects*. 2018 **40**(22) doi:10.1080/15567036.2018.1511642

[24] P. XU, T. W. COYLE, L. PERSHIN, J. MOSTAGHIMI. Fabrication of micro-/nano-structured superhydrophobic ceramic coating with reversible wettability via a novel solution precursor vacuum plasma spray process. *Materials and Design*. 2018, **160**, 974–984. doi:10.1016/j.matdes.2018.10.015

[25] P. XU, T. W. COYLE, L. PERSHIN, J. MOSTAGHIMI. Superhydrophobic ceramic coating: Fabrication by solution precursor plasma spray and investigation of wetting behavior. *Journal of Colloid and Interface Science*. 2018, **523**, 35–44. doi:10.1016/j.jcis.2018.03.018

[26] K. KOCH, B. BHUSHAN, Y. C. JUNG, W. BARTHLOTT. Fabrication of artificial Lotus leaves and significance of hierarchical structure for superhydrophobicity and low adhesion. *Soft Matter*. 2009, **5**(7), 1386. doi:10.1039/b818940d

[27] G. AZIMI, R. DHIMAN, H. M. KWON, A. T. PAXSON, K. K. VARANASI. Hydrophobicity of rare-earth oxide ceramics. *Nature Materials*. 2013, **12**(4), 315–320. doi:10.1038/nmat3545

[28] S. PRAKASH, S. GHOSH, A. PATRA, M. ANNAMALAI, M. R. MOTAPOTHULA, S. SARKAR, S. J. R. TAN, J. ZHUNAN, K. P. LOH, T. VENKATESAN. Intrinsic hydrophilic nature of epitaxial thin-film of rare-earth oxide grown by pulsed laser deposition. *Nanoscale*. 2018, **10**(7), 3356–3361. doi:10.1039/c7nr06642b

[29] S. P. FU, J. ROSSERO, C. CHEN, D. LI, C. G. TAKOUDIS, J. T. ABIADE. On the

wetting behavior of ceria thin films grown by pulsed laser deposition. *Applied Physics Letters*. 2017, **110**(8), 081601. doi:10.1063/1.4973997

[30] S. KHAN, G. AZIMI, B. YILDIZ, K. K. VARANASI. Role of surface oxygen-to-metal ratio on the wettability of rare-earth oxides. *Applied Physics Letters*. 2015, **106**(6), 061601 doi:10.1063/1.4907756

[31] S. ZENKIN, Š. KOS, J. MUSIL. Hydrophobicity of thin films of compounds of low-electronegativity metals. *Journal of the American Ceramic Society*. 2014, **97**(9), 2713–2717. doi:10.1111/jace.13165

[32] D. J. PRESTON, N. MILJKOVIC, J. SACK, R. ENRIGHT, J. QUEENEY, E. N. WANG. Effect of hydrocarbon adsorption on the wettability of rare earth oxide ceramics. *Applied Physics Letters*. 2014, **105**(1), 011601 doi:10.1063/1.4886410

[33] M. ZHANG, C. WANG, S. WANG, J. LI. Fabrication of superhydrophobic cotton textiles for water-oil separation based on drop-coating route. *Carbohydrate Polymers*. 2013, **97**(1), 59–64. doi:10.1016/j.carbpol.2012.08.118

[34] J. B. BOREYKO, C. H. CHEN. Self-propelled dropwise condensate on superhydrophobic surfaces. *Physical Review Letters*. 2009, **103**(18), 184501 doi:10.1103/PhysRevLett.103.184501

[35] K. M. WISDOM, J. A. WATSON, X. QU, F. LIU, G. S. WATSON, C. H. CHEN. Self-cleaning of superhydrophobic surfaces by self-propelled jumping condensate. *Proceedings of the National Academy of Sciences of the United States of America*. 2013, **110**(20), 7992–7997. doi:10.1073/pnas.1210770110

[36] K. LIU, L. JIANG. Bio-inspired self-cleaning surfaces. *Annual Review of Materials Research*. 2012, **42**(1), 231–263. doi:10.1146/annurev-matsci-070511-155046

[37] R. BLOSSEY. Self-cleaning surfaces - Virtual realities. *Nature Materials*. 2003, **2**(5), 301–306. doi:10.1038/nmat856

[38] H. KOIVULUOTO, E. HARTIKAINEN, H. NIEMELÄ-ANTTONEN. Thermally sprayed coatings: Novel surface engineering strategy towards icephobic solutions. *Materials*. 2020, **13**(6), 1434. doi:10.3390/ma13061434

[39] Q. XU, J. LI, J. TIAN, J. ZHU, X. GAO. Energy-effective frost-free coatings based on superhydrophobic aligned nanocones. *ACS Applied Materials and Interfaces*. 2014, **6**(12), 8976–8980. doi:10.1021/am502607e

[40] A. M. EMELYANENKO, F. M. SHAGIEVA, A. G. DOMANTOVSKY, L. B. BOINOVICH. Nanosecond laser micro- and nanotexturing for the design of a superhydrophobic coating robust against long-term contact with water, cavitation, and abrasion. *Applied Surface Science*. 2015, **332**, 513–517. doi:10.1016/j.apsusc.2015.01.202

[41] C. LEE, C. J. KIM. Underwater restoration and retention of gases on superhydrophobic surfaces for drag reduction. *Physical Review Letters*. 2011, **106**(1), 014502. doi:10.1103/PhysRevLett.106.014502

[42] X. DING, X. D. CHENG, C. Q. YUAN, J. SHI, Z. X. DING. Structure of micro-nano WC-10Co4Cr coating and cavitation erosion resistance in NaCl solution. *Chinese Journal of Mechanical Engineering (English Edition)*. 2017, **30**(5), 1239–1247. doi:10.1007/s10033-017-0162-9

[43] J. ZHANG, J. WANG, B. ZHANG, Y. ZENG, J. DUAN, B. HOU. Fabrication of

anodized superhydrophobic 5083 aluminum alloy surface for marine anti-corrosion and anti-biofouling. *Journal of Oceanology and Limnology*. 2020, **38**(4), 1246–1255 doi:10.1007/s00343-020-0036-3

[44] L. CAO, A. K. JONES, V. K. SIKKA, J. WU, D. GAO. Anti-icing superhydrophobic coatings. *Langmuir*. 2009, **25**(21), 12444–12448. doi:10.1021/la902882b

[45] T. VERHO, C. BOWER, P. ANDREW, S. FRANSSILA, O. IKKALA, R. H. A. RAS. Mechanically durable superhydrophobic surfaces. *Advanced Materials*. 2011, **23**(5), 673–678. doi:10.1002/adma.201003129

[46] L. HU, X. SONG, D. JIN, C. XING, X. SHAN, X. ZHAO, F. GUO, P. XIAO. A robust quasi-superhydrophobic ceria coating prepared using air-plasma spraying. *Journal of the American Ceramic Society*. 2019, **102**(3), 1386–1393. doi:10.1111/jace.16005

[47] P. XU, T. W. COYLE, L. PERSHIN, J. MOSTAGHIMI. Fabrication of superhydrophobic ceramic coatings via solution precursor plasma spray under atmospheric and low-pressure conditions. *Journal of Thermal Spray Technology*. 2019, **28**(1–2), 242–254. doi:10.1007/s11666-018-0814-z

[48] *Thermal Spraying | Research and Development | OSAKA FUJI Corporation | overlay welding, thermal spraying, machining technology* [online]. https://www.ofic.co.jp/en/r_and_d/thermalspraying/

[49] D. TEJERO-MARTIN, M. REZVANI RAD, A. MCDONALD, T. HUSSAIN. Beyond Traditional Coatings: A Review on Thermal-Sprayed Functional and Smart Coatings. *Journal of Thermal Spray Technology*. 2019, **28**(4), 598–644. doi:10.1007/S11666-019-00857-1

[50] L. PAWLOWSKI. *The science and engineering of thermal spray coatings*. Chichester, UK: John Wiley & Sons, Ltd, 2008. ISBN 9780470754085. doi:10.1002/9780470754085

[51] *HVOF - High Velocity Oxygen Fuel* [online]. https://www.fst.nl/thermal-spray-equipment/modular-thermal-spray-systems/hvof-spray-systems/hvof-high-velocity-oxygen-fuel.html

[52] *Plasma Spray* [online]. https://www.fst.nl/thermal-spray-equipment/modular-thermal-spray-systems/plasma-thermal-spray-systems/plasma-spraying.html

[53] M. HRABOVSKÝ. Water-stabilized plasma generators. *Pure and Applied Chemistry*. 1998, **70**(6), 1157–1162. doi:10.1351/pac199870061157

[54] R. MUSALEK, J. MEDRICKY, T. TESAR, J. KOTLAN, Z. PALA, F. LUKAC, T. CHRASKA, N. CURRY. Suspensions plasma spraying of ceramics with hybrid water-stabilized plasma technology. *Journal of Thermal Spray Technology*. 2017, **26**(1–2), 37–46. doi:10.1007/s11666-016-0493-6

[55] P. FAUCHAIS, A. JOULIA, S. GOUTIER, C. CHAZELAS, M. VARDELLE, A. VARDELLE, S. ROSSIGNOL. Suspension and solution plasma spraying. *Journal of Physics D: Applied Physics*. 2013, **46**(22), 224015. doi:10.1088/0022-3727/46/22/224015

[56] F. L. TOMA, A. POTTHOFF, L. M. BERGER, C. LEYENS. Demands, potentials, and economic aspects of thermal spraying with suspensions: A critical review. *Journal of Thermal Spray Technology*. 2015, **24**(7), 1143–1152. doi:10.1007/s11666-015-0274-7

[57] R. AHMED, O. ALI, N. H. FAISAL, N. M. AL-ANAZI, S. AL-MUTAIRI, F. L. TOMA,

L. M. BERGER, A. POTTHOFF, M. F.A. GOOSEN. Sliding wear investigation of suspension sprayed WC-Co nanocomposite coatings. *Wear*. 2015, **322**–**323**, 133–150. doi:10.1016/j.wear.2014.10.021

[58] J. KARTHIKEYAN, C. BERNDT, S. REDDY, J. WANG, A. H. KING, H. HERMAN. Nanomaterial deposits formed by DC plasma spraying of liquid feedstocks. *Journal of the American Ceramic Society*. 2005, **81**(1), 121–128. doi:10.1111/j.1151-2916.1998.tb02303.x

[59] T. TESAR, R. MUSALEK, J. MEDRICKY, J. KOTLAN, F. LUKAC, Z. PALA, P. CTIBOR, T. CHRASKA, S. HOUDKOVA, V. RIMAL, N. CURRY. Development of suspension plasma sprayed alumina coatings with high enthalpy plasma torch. *Surface and Coatings Technology*. 2017, **325**, 277–288. doi:10.1016/j.surfcoat.2017.06.039

[60] A. GANVIR, S. JOSHI, N. MARKOCSAN, R. VASSEN. Tailoring columnar microstructure of axial suspension plasma sprayed TBCs for superior thermal shock performance. *Materials and Design*. 2018, **144**, 192–208. doi:10.1016/j.matdes.2018.02.011

[61] P. SOKOŁOWSKI, S. BJÖRKLUND, R. MUSALEK, R. T. CANDIDATO, L. PAWŁOWSKI, B. NAIT-ALI, D. SMITH. Thermophysical properties of YSZ and YCeSZ suspension plasma sprayed coatings having different microstructures. *Surface and Coatings Technology*. 2017, **318**, 28–38. doi:10.1016/j.surfcoat.2017.02.054

[62] H. KASSNER, R. SIEGERT, D. HATHIRAMANI, R. VASSEN, D. STOEVER. Application of suspension plasma spraying (SPS) for manufacture of ceramic coatings. *Journal of Thermal Spray Technology*. 2008, **17**, 115-123. doi:10.1007/s11666-007-9144-2

[63] R. TOMASZEK, L. PAWLOWSKI, L. GENGEMBRE, J. LAUREYNS, Z. ZNAMIROWSKI, J. ZDANOWSKI. Microstructural characterization of plasma sprayed TiO_2 functional coating with gradient of crystal grain size. *Surface and Coatings Technology*. 2006, **201**(1–2), 45–56. doi:10.1016/j.surfcoat.2005.10.033

[64] J. YUAN, Q. ZHAN, Q. LEI, S. DING, H. LI. Fabrication and characterization of hybrid micro/nano-structured hydrophilic titania coatings deposited by suspension flame spraying. *Applied Surface Science*. 2012, **258**(17), 6672–6678. doi:10.1016/j.apsusc.2012.03.112

[65] B. J. V. YOON, F. XAVIER, B. R. WALKER, S. GRINBERG, F. P. CAMMISA, C. ABJORNSON. Optimizing surface characteristics for cell adhesion and proliferation on titanium plasma spray coatings on polyetheretherketone. *Spine Journal*. 2016, **16**(10), 1238–1243. doi:10.1016/j.spinee.2016.05.017

[66] G. GHOSH, A. SIDPARA, P. P. BANDYOPADHYAY. Fabrication of mechanically durable slippery surface on HVOF sprayed WC-Co coating. *Surface and Coatings Technology*. 2020, **394**, 125886. doi:10.1016/j.surfcoat.2020.125886

[67] X. CHEN, J. YUAN, J. HUANG, K. REN, Y. LIU, S. LU, H. LI. Large-scale fabrication of superhydrophobic polyurethane/nano-Al_2O_3 coatings by suspension flame spraying for anti-corrosion applications. *Applied Surface Science*. 2014, **311**, 864–869. doi:10.1016/j.apsusc.2014.05.186

[68] X. CHEN, Y. GONG, D. LI, H. LI. Robust and easy-repairable superhydrophobic surfaces with multiple length-scale topography constructed by thermal spray route. *Colloids and Surfaces A: Physicochemical and Engineering Aspects*. 2016, **492**, 19–25.

doi:10.1016/j.colsurfa.2015.12.017

[69] N. SHARIFI, M. PUGH, C. MOREAU, A. DOLATABADI. Developing hydrophobic and superhydrophobic TiO_2 coatings by plasma spraying. *Surface and Coatings Technology*. 2016, **289**, 29–36. doi:10.1016/j.surfcoat.2016.01.029

[70] X. CHEN, Y. GONG, X. SUO, J. HUANG, Y. LIU, H. LI. Construction of mechanically durable superhydrophobic surfaces by thermal spray deposition and further surface modification. *Applied Surface Science*. 2015, **356**, 639–644. doi:10.1016/j.apsusc.2015.08.156

[71] J. QIAO, L. ZHU, W. YUE, Z. Q. FU, J. KANG, C. WANG. The effect of attributes of micro-shapes of laser surface texture on the wettability of WC-CrCo metal ceramic coatings. *Surface and Coatings Technology*. 2018, **334**, 429–437. doi:10.1016/j.surfcoat.2017.12.001

[72] S. VIJAY, L. WANG, C. LYPHOUT, P. NYLEN, N. MARKOCSAN. Surface characteristics investigation of HVAF sprayed cermet coatings. *Applied Surface Science*. 2019, **493**, 956–962. doi:10.1016/j.apsusc.2019.07.079

[73] N. XI, Y. LIU, X. ZHANG, N. LIU, H. FU, Z. HANG, G. YANG, H. CHEN, W. GAO. Steady anti-icing coatings on weathering steel fabricated by HVOF spraying. *Applied Surface Science*. 2018, **444**, 757–762. doi:10.1016/j.apsusc.2018.03.075

[74] M. BAI, H. KAZI, X. ZHANG, J. LIU, T. HUSSAIN. Robust hydrophobic surfaces from suspension HVOF thermal sprayed rare-earth oxide ceramics coatings. *Scientific Reports*. 2018, **8**(1), 1–8. doi:10.1038/s41598-018-25375-y

[75] E. KEDROŇOVÁ, L. ZAJÍČKOVÁ, D. HEGEMANN, M. KLÍMA, M. MICHLÍČEK, A. MANAKHOV. Plasma enhanced CVD of organosilicon thin films on electrospun polymer nanofibers. *Plasma Processes and Polymers*. 2015, **12**(11), 1231–1243. doi:10.1002/ppap.201400235

[76] K. DVOŘÁK, D. GAZDIČ, M. FRIDRICHOVÁ. The influence of firing parameters on the crystallinity of ternesite. *Journal of Crystal Growth*. 2020, **542**, 125691. doi:10.1016/j.jcrysgro.2020.125691

[77] J. A. R. WESMANN, N. ESPALLARGAS. Elucidating the complex role of surface oxides formed during sliding of self-mated warm sprayed WC-CoCr in different environments. *Tribology International*. 2016, **94**, 360–372. doi:10.1016/j.triboint.2015.09.043

[78] J. A. R. WESMANN, S. KURODA, N. ESPALLARGAS. The role of oxide tribofilms on friction and wear of different thermally sprayed WC-CoCr. *Journal of Thermal Spray Technology*. 2017, **26**(3), 492–502. doi:10.1007/s11666-017-0522-0

[79] L. N. ZHANG, Y. Y. MA, Z. L. LANG, Y. H. WANG, S. U. KHAN, G. YAN, H. Q. TAN, H. Y. ZANG, Y. G. LI. Ultrafine cable-like WC/W_2C heterojunction nanowires covered by graphitic carbon towards highly efficient electrocatalytic hydrogen evolution. *Journal of Materials Chemistry A*. 2018, **6**(31), 15395–15403. doi:10.1039/c8ta05007d

[80] J. A. PICAS, M. PUNSET, E. RUPÉREZ, S. MENARGUES, E. MARTIN, M. T. BAILE. Corrosion mechanism of HVOF thermal sprayed WC-CoCr coatings in acidic chloride media. *Surface and Coatings Technology*. 2019, **371**, 378–388. doi:10.1016/j.surfcoat.2018.10.025

[81] Z. CHEN, W. GONG, S. CONG, Z. WANG, G. SONG, T. PAN, X. TANG, J. CHEN, W. LU, Z. ZHAO. Eutectoid-structured WC/W_2C heterostructures: A new platform for long-term alkaline hydrogen evolution reaction at low overpotentials. *Nano Energy*. 2020, **68**, 104335. doi:10.1016/j.nanoen.2019.104335

[82] *ISO - ISO 25178-2:2012 - Geometrical product specifications (GPS) — Surface texture: Areal — Part 2: Terms, definitions and surface texture parameters* [online]. https://www.iso.org/standard/42785.html

[83] K. SLÁMEČKA, D. JECH, L. KLAKURKOVÁ, S. TKACHENKO, M. REMEŠOVÁ, P. GEJDOŠ, L. ČELKO. Thermal cycling damage in pre-oxidized plasma-sprayed MCrAlY + YSZ thermal barrier coatings: Phenomenon of multiple parallel delamination of the TGO layer. *Surface and Coatings Technology*. 2020, **384**, 125328. doi:10.1016/j.surfcoat.2019.125328

[84] *ASTM G75 - 15 Standard Test Method for Determination of Slurry Abrasivity (Miller Number) and Slurry Abrasion Response of Materials (SAR Number)* [online]. https://www.astm.org/Standards/G75.htm

[85] *ASTM G32 - 16 Standard Test Method for Cavitation Erosion Using Vibratory Apparatus* [online]. https://www.astm.org/Standards/G32

[86] M. HARJU, E. LEVANEN, T. MANTYLA. Wetting behaviour of plasma sprayed oxide coatings. *Applied Surface Science*. 2006, **252**(24), 8514-8520. doi:10.1016/j.apsusc.2005.11.065

[87] Y. HAN, Y. LIU, W. WANG, J. LENG, P. JIN. Controlled wettability based on reversible micro-cracking on a shape memory polymer surface. *Soft Matter*. 2016, **12**(10), 2708–2714. doi:10.1039/C5SM03059E

[88] K. VANEVERY, M. J.M. KRANE, R. W. TRICE, H. WANG, W. PORTER, M. BESSER, D. SORDELET, J. ILAVSKY, J. ALMER. Column formation in suspension plasma-sprayed coatings and resultant thermal properties. *Journal of Thermal Spray Technology*. 2011, **20**, 817-828. doi:10.1007/s11666-011-9632-2

[89] P. SOKOŁOWSKI, L. PAWŁOWSKI, D. DIETRICH, T. LAMPKE, D. JECH. Advanced microscopic study of suspension plasma-sprayed zirconia coatings with different microstructures. *Journal of Thermal Spray Technology*. 2016, **25**(1–2), 94–104. doi:10.1007/s11666-015-0310-7

[90] D. ZHOU, O. GUILLON, R. VASSEN. Development of YSZ thermal barrier coatings using axial suspension plasma spraying. *Coatings*. 2017, **7**(8), 120. doi:10.3390/coatings7080120

[91] P. XU, G. MENG, L. PERSHIN, J. MOSTAGHIMI, T. W. COYLE. Control of the hydrophobicity of rare earth oxide coatings deposited by solution precursor plasma spray by hydrocarbon adsorption. *Journal of Materials Science and Technology*. 2021, **62**, 107–118. doi:10.1016/j.jmst.2020.04.044

[92] I. P. GULYAEV, V. I. KUZMIN, O. B. KOVALEV. Highly hydrophobic ceramic coatings produced by plasma spraying of powder materials. *Thermophysics and Aeromechanics*. 2020, **27**(4), 585–594. doi:10.1134/S0869864320040113

[93] P. KOMAROV, D. JECH, S. TKACHENKO, K. SLÁMEČKA, K. DVOŘÁK, L. ČELKO. Wetting behavior of wear-resistant WC-Co-Cr cermet coatings produced by HVOF: The role of chemical composition and surface roughness. *Journal of Thermal Spray Technology*. 2021, **30**(1–2), 285–303. doi: 10.1007/s11666-020-01130-6

[94] S. AL-MUTAIRI, M. S.J. HASHMI, B. S. YILBAS, J. STOKES. Microstructural characterization of HVOF/plasma thermal spray of micro/nano WC-12%Co powders. *Surface and Coatings Technology*. 2015, **264**, 175–186. doi:10.1016/j.surfcoat.2014.12.050

[95] J. PULSFORD, S. KAMNIS, J. MURRAY, M. BAI, T. HUSSAIN. Effect of particle and carbide grain sizes on a HVOAF WC-Co-Cr coating for the future application on internal surfaces: Microstructure and wear. *Journal of Thermal Spray Technology*. 2018, **27**(1–2), 207–219. doi:10.1007/s11666-017-0669-8

[96] A. LEKATOU, D. SIOULAS, A. E. KARANTZALIS, D. GRIMANELIS. A comparative study on the microstructure and surface property evaluation of coatings produced from nanostructured and conventional WC-Co powders HVOF-sprayed on Al7075. *Surface and Coatings Technology*. 2015, **276**, 539–556. doi:10.1016/j.surfcoat.2015.06.017

[97] Q. YANG, T. SENDA, A. OHMORI. Effect of carbide grain size on microstructure and sliding wear behavior of HVOF-sprayed WC-12% Co coatings. *Wear*. 2003, **254**(1–2), 23–34. doi:10.1016/S0043-1648(02)00294-6

[98] M. LI, P. D. CHRISTOFIDES. Computational study of particle in-flight behavior in the HVOF thermal spray process. *Chemical Engineering Science*. 2006, **61**(19), 6540–6552. doi:10.1016/j.ces.2006.05.050

[99] C. J. LI, A. OHMORI, Y. HARADA. Formation of an amorphous phase in thermally sprayed WC-Co. *Journal of Thermal Spray Technology*. 1996, **5**(1), 69–73. doi:10.1007/BF02647520

[100] M. FEDERICI, C. MENAPACE, A. MOSCATELLI, S. GIALANELLA, G. STRAFFELINI. Pin-on-disc study of a friction material dry sliding against HVOF coated discs at room temperature and 300 °C. *Tribology International*. 2017, **115**, 89–99. doi:10.1016/j.triboint.2017.05.030

[101] S. M. NAHVI, M. JAFARI. Microstructural and mechanical properties of advanced HVOF-sprayed WC-based cermet coatings. *Surface and Coatings Technology*. 2016, **286**, 95–102. doi:10.1016/j.surfcoat.2015.12.016

[102] X. DING, X. D. CHENG, C. LI, X. YU, Z. X. DING, C. Q. YUAN. Microstructure and performance of multi-dimensional WC-CoCr coating sprayed by HVOF. *International Journal of Advanced Manufacturing Technology*. 2018, **96**(5–8), 1625–1633. doi:10.1007/s00170-017-0837-5

[103] A. G. SHARD. Practical guides for X-ray photoelectron spectroscopy: Quantitative XPS. *Journal of Vacuum Science & Technology A*. 2020, **38**(4), 041201. doi:10.1116/1.5141395

[104] P. L. J. GUNTER, O. L.J. GIJZEMAN, J. W. NIEMANTSVERDRIET. Surface roughness effects in quantitative XPS: Magic angle for determining overlayer thickness. *Applied Surface Science*. 1997, **115**(4), 342–346. doi:10.1016/S0169-4332(97)00007-X

[105] J. ZEMEK, K. OLEJNIK, P. KLAPETEK. Photoelectron spectroscopy from randomly corrugated surfaces. *Surface Science*. 2008, **602**(7), 1440–1446. doi:10.1016/j.susc.2008.02.006

[106] R. VASSEN, G. KERKHOFF, D. STÖVER. Development of a micromechanical life prediction model for plasma sprayed thermal barrier coatings. *Materials Science and Engineering A*. 2001, **303**(1–2), 100–109. doi:10.1016/S0921-5093(00)01853-0

[107] W. TILLMANN, L. HAGEN, D. STANGIER, M. KRABIELL, P. SCHRÖDER, J. TILLER, C. KRUMM, C. STERNEMANN, M. PAULUS, M. ELBERS. Influence of etching-pretreatment on nano-grained WC-Co surfaces and properties of PVD/HVOF duplex coatings. *Surface and Coatings Technology*. 2019, **374**, 32–43. doi:10.1016/j.surfcoat.2019.05.054

[108] J. LI, C. LI, G. YANG, C. LI. Wettability transition on micro-nano hierarchical structured Ni20Cr coating surface by selective spontaneous adsorption during vacuum evacuation. *Materials Chemistry and Physics*. 2018, **219**, 292–302. doi:10.1016/j.matchemphys.2018.08.049

[109] M. MORRA, E. OCCHIELLO, R. MAROLA, F. GARBASSI, P. HUMPHREY, D. JOHNSON. On the aging of oxygen plasma-treated polydimethylsiloxane surfaces. *Journal of Colloid And Interface Science*. 1990, **137**(1), 11–24. doi:10.1016/0021-9797(90)90038-P

[110] T. GONG, P. YAO, X. ZUO, Z. ZHANG, Y. XIAO, L. ZHAO, H. ZHOU, M. DENG, Q. WANG, A. ZHONG. Influence of WC carbide particle size on the microstructure and abrasive wear behavior of WC-10Co-4Cr coatings for aircraft landing gear. *Wear*. 2016, **362**–**363**, 135–145. doi:10.1016/j.wear.2016.05.022

[111] A. KANNO, K. TAKAGI, M. ARAI. Influence of chemical composition, grain size, and spray condition on cavitation erosion resistance of high-velocity oxygen fuel thermal-sprayed WC cermet coatings. *Surface and Coatings Technology*. 2020, **394**, 125881. doi:10.1016/j.surfcoat.2020.125881

[112] B. SONG, J. W. MURRAY, R. G. WELLMAN, Z. PALA, T. HUSSAIN. Dry sliding wear behaviour of HVOF thermal sprayed WC-Co-Cr and WC-Cr_xC_y-Ni coatings. *Wear*. 2020, **442**–**443**, 203114. doi:10.1016/j.wear.2019.203114

[113] J. M. GUILEMANY, S. DOSTA, J. R. MIGUEL. The enhancement of the properties of WC-Co HVOF coatings through the use of nanostructured and microstructured feedstock powders. *Surface and Coatings Technology*. 2006, **201**(3–4), 1180–1190. doi:10.1016/j.surfcoat.2006.01.041

[114] X. DING, D. KE, C. YUAN, Z. DING, X. CHENG. Microstructure and cavitation erosion resistance of HVOF deposited WC-Co coatings with different sized WC. *Coatings*. 2018, **8**(9), 307. doi:10.3390/coatings8090307

[115] Y. WU, S. HONG, J. ZHANG, Z. HE, W. GUO, Q. WANG, G. LI. Microstructure and cavitation erosion behavior of WC-Co-Cr coating on 1Cr18Ni9Ti stainless steel by HVOF thermal spraying. *International Journal of Refractory Metals and Hard Materials*. 2012, **32**, 21–26. doi:10.1016/j.ijrmhm.2012.01.002

[116] J. FAHIM, S. M.M. HADAVI, H. GHAYOUR, S. A. HASSANZADEH TABRIZI. Cavitation erosion behavior of super-hydrophobic coatings on Al5083 marine aluminum alloy. *Wear*. 2019, **424**–**425**, 122–132. doi:10.1016/j.wear.2019.02.017

[117] P. XU, T. W. COYLE, L. PERSHIN, J. MOSTAGHIMI. Understanding the correlations between the mechanical robustness, coating structures and surface composition for highly-/super-hydrophobic ceramic coatings. *Surface and Coatings Technology*. 2019, **378**, 124929. doi:10.1016/j.surfcoat.2019.124929

[118] L. BOINOVICH, A. M. EMELYANENKO, V. K. IVANOV, A. S. PASHININ. Durable icephobic coating for stainless steel. *ACS Applied Materials and Interfaces*. 2013, **5**(7), 2549–2554. doi: 10.1021/am3031272

[119] R. JAFARI, G. MOMEN, E. ESLAMI. Fabrication of icephobic aluminium surfaces by atmospheric plasma jet polymerisation. *Surface Engineering*. 2018, **35**(5), 450–455. doi:10.1080/02670844.2018.1509813

[120] N. XI, Y. LIU, X. ZHANG, N. LIU, H. FU, Z. HANG, G. YANG, H. CHEN, W. GAO. Steady anti-icing coatings on weathering steel fabricated by HVOF spraying. *Applied Surface Science*. 2018, **444**, 757–762. doi:10.1016/j.apsusc.2018.03.075

[121] P. IRAJIZAD, S. NAZIFI, H. GHASEMI. Icephobic surfaces: Definition and figures of merit. *Advances in Colloid and Interface Science*. 2019, **269**, 203–218. doi:10.1016/j.cis.2019.04.005

[122] L. XU, J. SONG, X. ZHANG, C. DENG, M. LIU, K. ZHOU. Microstructure and corrosion resistance of WC-based cermet/Fe-rased amorphous alloy composite coatings. *Coatings.* 2018, **8**(11), 393. doi:10.3390/coatings8110393

List of abbreviations

Al_2O_3	Aluminium oxide
APS	Atmospheric plasma spray
Ar	Argon
ASW	Artificial sea-water
at. %	Atomic percent
C	Carbon
CA	Contact angle
CE	Cavitation erosion
Cr_2O_3-SiO_2-TiO_2	Chromium oxide - Silicon oxide - Titanium oxide
EDX	Energy dispersive X-ray spectroscopy
H_2	Hydrogen
HMDSO	Hexamethyldisiloxane
HV	Vickers hardness
HVOF	High-velocity oxy-fuel spray
NiCr	Nickel - Chromium
O	Oxygen
PDMS	Polydimethylsiloxane
Ra	Arithmetic mean height
REO	Rare-earth oxide
RF-plasma	Radio-frequency plasma
Rs	Surface roughness factor
SA	Sliding angle
Sa	Surface arithmetic mean height
SAR	Slurry abrasion response test
SEM	Scanning electron microscopy
SFE	Surface free energy
Si	Silicon
Si-oil	Silicone-oil
Sku	Kurtosis
SPAPS	Solution precursor atmospheric plasma spray
SPPS	Solution precursor plasma spray
SPS	Suspension plasma spray
SPVPS	Solution precursor vacuum plasma spray

Sq	Root mean square height
Ssk	Skewness
vol. %	Volume percent
W	Tungsten
W_2C	Ditungsten carbide
WCA	Water contact angle
WC-Co-Cr	Tungsten carbide - Cobalt - Chromium
WSP-H	Hybrid water-stabilized plasma spray
wt. %	Weight percent
XPS	X-ray photoelectron spectroscopy
XRD	X-ray diffraction
Y	Yttrium
YSZ	Yttria-stabilized zirconia (ZrO_2-Y_2O_3)
Zr	Zirconium
f_s	Part of the solid surface area that is in contact with liquid droplet
γ_{lv}	Liquid surface tension
γ_{sl}	Solid/liquid interfacial free energy
γ_{sv}	Solid surface free energy
γ^d	Dispersive component of surface energy
γ^p	Polar component of surface energy
θ	Contact angle

List of publications

Publications related to the thesis

[1] **P. KOMAROV**, D. JECH, S. TKACHENKO, K. SLÁMEČKA, K. DVOŘÁK, L. ČELKO. Wetting behavior of wear-resistant WC-Co-Cr cermet coatings produced by HVOF: The role of chemical composition and surface roughness. *Journal of Thermal Spray Technology*. 2021, **30**(1–2), 285–303. doi:10.1007/S11666-020-01130-6

[2] **P. KOMAROV**, D. JECH, L. ČELKO, B. PIJÁKOVÁ, D. ZHOU, R. VASSEN. Influence of RF plasma jet surface treatment on wetting behavior of yttria stabilized zirconia SPS coatings. *Defect and Diffusion Forum*. 2020, **405**, 423–429. doi:10.4028/www.scientific.net/DDF.405.423

[3] **P. KOMAROV**, L. ČELKO, M. REMEŠOVÁ, K. SKOROKHOD, D. JECH, L. KLAKURKOVÁ, K. SLÁMEČKA, R. MUŠÁLEK. The role of microstructure on wettability of plasma sprayed yttria stabilized zirconia coatings, in: *Metal 2017 - 26th Int. Conf. Metall. Mater.*, TANGER Ltd, 2017: pp. 1116–1121.

[4] **P. KOMAROV**, L. ČELKO, D. JECH, M. PAPULA, K. SLÁMEČKA, M. HORYNOVÁ, L. KLAKURKOVÁ, J. KAISER. Investigations of wettability of wear resistant coatings produced by atmospheric plasma spraying. *Solid State Phenomena*. 2017, **270**, 230–235. doi:10.4028/www.scientific.net/SSP.270.230

Other publications

[1] L. ČELKO, S. TKACHENKO, M. CASAS-LUNA, L. DYČKOVÁ, V. BEDNAŘÍKOVÁ, M. REMEŠOVÁ, **P. KOMAROV**, A. DEÁK, M. BALÁŽ, D. CRAWFORD, S. DIAZ-DE-LA-TORRE, E. BODOKI, J. CIHLÁŘ. High-energy ball milling and spark plasma sintering of molybdenum - lanthanum oxide (Mo-La_2O_3) and molybdenum – lanthanum zirconate (Mo-$La_2Zr_2O_7$) composite powders. *International Journal of Refractory Metals and Hard Materials*. 2022, **102**, 105717. doi:10.1016/j.ijrmhm.2021.105717

[2] **P. KOMAROV**, S. TKACHENKO, M. REMEŠOVÁ, A. DEÁK, D. CRAWFORD, M. CASAS-LUNA, V. BEDNAŘÍKOVÁ, E. BODOKI, J. CIHLÁŘ, L. ČELKO. Effect of high-energy attrition milling and La_2O_3 content on the microstructure of Mo-La_2O_3 composite powders. *IOP Conference Series: Materials Science and Engineering*. 2021, **1178**(1), 012030. doi:10.1088/1757-899X/1178/1/012030

[3] D. JECH, **P. KOMAROV**, M. REMEŠOVÁ, L. DYČKOVÁ, K. SLÁMEČKA, S. RAVASZOVÁ, K. DVOŘÁK, L. ČELKO. Thermal cyclic behaviour of conventional YSZ and mullite-YSZ thermal barrier coatings. *Defect and Diffusion Forum*. 2020, **405**, 417–422. doi:10.4028/ www.scientific.net /DDF.405.417

[4] Z. PAVLOUŠKOVÁ, D. JECH, **P. KOMAROV**, I. ROČŇÁKOVÁ, L. DYČKOVÁ, M. REMEŠOVÁ, L. ČELKO, D. HOLEMÝ. Characterization of high-speed alumina abrasive grinding wheel. *Defect and Diffusion Forum*. 2020, **405**, 365–369. doi:10.4028/ www.scientific.net /DDF.405.365

[5] D. JECH, M. REMEŠOVÁ, **P. KOMAROV**, S. TKACHENKO, Z. ČESÁNEK, J. SCHUBERT, Š. HOUDKOVÁ, L. ČELKO. Evaluation of microstructure, phase composition and hardness of alternative abradable ceramic coating systems produced by means of atmospheric plasma spraying. *Solid State Phenomena*. 2019, **296**, 161–166.

doi:10.4028/ www.scientific.net /SSP.296.161

[6] L. ČELKO, D. JECH, S. TKACHENKO, **P. KOMAROV**, M. REMEŠOVÁ, K. SLÁMEČKA, P. CTIBOR. Failure of gadolinium zirconate and yttria stabilized zirconia thermal barrier coatings subjected to high temperature calcia-magnesia-alumino-silicate attack. *Procedia Structural Integrity*. 2019, **23**, 360–365. doi:10.1016/j.prostr.2020.01.113

[7] L. DYČKOVÁ, **P. KOMAROV**, M. REMEŠOVÁ, M. DYČKA, K. DVOŘÁK, M. MENELAOU, L. ČELKO. Optimization of molybdenum powder milling parameters. *Metal Working and Material Science*. 2018, **20**(3), 109–122. doi:10.17212/1994-6309-2018-20.3-109-122

[8] A. GABETS, A.M. MARKOV, D.A. GABETS, **P. KOMAROV**, E.O. CHERTOVSKIKH. Investigation of chemical composition and material structure influence on mechanical properties of special cast iron, in: *Metal 2017 – 26th Int. Conf. Metall. Mater.*, TANGER Ltd, 2017: pp. 782-788.

[9] D. JECH, L. ČELKO, **P. KOMAROV**, J. ZIEGELHEIM, Z. ČESÁNEK, J. SCHUBERT. The role of different atmospheric plasma spray parameters on microstructure of abradable AlSi-polyester coatings. *Solid State Phenomena*. 2017, **270**, 224–229. doi:10.4028/ www.scientific.net /SSP.270.224

[10] L. ČELKO, D. JECH, **P. KOMAROV**, M. REMEŠOVÁ, K. DVOŘÁK, I. ŠULÁK, B. SMETANA, K. OBRTLÍK. Failure mechanism of yttria stabilized zirconia atmospheric plasma sprayed thermal barrier coatings subjected to calcia-magnesia-alumino-silicate environmental attack. *Solid State Phenomena*. 2017, **270**, 39–44. doi:10.4028/ www.scientific.net /SSP.270.39

Product

- Co-author of the functional sample “Plošný vyhřívací povlak s vysokou homogenitou teplotního pole” (Surface heating coating with high temperature field homogeneity)

Internships, conferences and trainings

- 2-month internship (September - November 2018) at the department of Materials for High-Temperature Technologies of the Forschungszentrum Jülich (Germany) under the supervision of Prof. Dr. Robert Vaßen
- 2-month internship (July – August 2018) at the department of Materials Science and Technology of Materials of the Novosibirsk State Technical University (Russia) under the supervision of Prof. Dr. Vladimir Bataev
- 2-month internship (July – August 2017) at the department of Materials Science and Technology of Materials of the Novosibirsk State Technical University (Russia) under the supervision of Prof. Dr. Vladimir Bataev

- 6th International Conference on Recent Trends in Structural Materials (COMAT 2020, Pilsen, Czech Republic)
- 9th Les Rencontres Internationales de la Projection Thermique (9 RIPT 2019, Jülich, Germany)
- 17th International Conference Metallography and Fractography (M&F 2019, Nový Smokovec, Slovakia)
- 14th Conference on Contribution of Metallography to Production Problem Solutions (14th CCMPPS 2017, Mariánské Lázně, Czech Republic)
- 26th International Conference on Metallurgy and Materials (METAL 2017, Brno, Czech Republic)

- Workshop on “The evolution of TBC with emerging thermal spray technologies” (April 2018, Pilsen, Czech Republic)
- Applied-seminar “Modern measurement techniques for surface chemistry” (May 2018, Filderstadt, Germany)

- Core facilities self-user for SEM, EDX, XRD, XPS, WCA/SFE, metallographic samples preparation

Participation in research projects

- Specific Research Project CEITEC VUT-J-19-5799 (VUT-junior project 2019) "Thermal spraying as a promising way to develop hydrophobic coatings from WC material"

List of figures

List of tables